New bioprocess technologies underpinning future manufacture of magnetosome products

By

Hong Li

A thesis submitted to the University of Birmingham

For the degree of

DOCTOR OF PHILOSOPHY

School of Chemical Engineering

College of Engineering and Physical Sciences

October 2018

UNIVERSITY OF
BIRMINGHAM

University of Birmingham Research Archive

e-theses repository

This unpublished thesis/dissertation is copyright of the author and/or third parties. The intellectual property rights of the author or third parties in respect of this work are as defined by The Copyright Designs and Patents Act 1988 or as modified by any successor legislation.

Any use made of information contained in this thesis/dissertation must be in accordance with that legislation and must be properly acknowledged. Further distribution or reproduction in any format is prohibited without the permission of the copyright holder.

Abstract

Magnetic support based separations in biotechnological applications was initiated in the late 1970's. Since then, magnetic supports have been widely applied in the laboratory and increasingly at process scales in hugely diverse applications. To date most of these have employed artificial chemically synthesized magnetic particles, but interest in naturally occurring magnetic materials made biologically is growing. Magnetosomes are one such example. These are needle-like chains of single-domain permanently magnetic membrane-wrapped crystals that act as a compass to allow magnetotactic bacteria navigate along geomagnetic field lines in search of optimal environmental oxygen levels. Their unique characteristics convey numerous advantages over chemically manufactured magnetic particles in biomedical and biotechnological settings, but future widespread application requires the development of commercial scale intensified high-yielding manufacturing platforms for magnetosome-based products.

Against the above the overall aim of this work has been to advance new bioprocess technologies underpinning future manufacture of magnetosome products.

The starting point for this work was to develop a battery of flow cytometric tools for analysing the growth, viability, physiology of magnetotactic bacteria (*Magnetospirillum gryphiswaldense* MSR-1 was selected as a model organism) and their biomineralization of magnetic iron minerals. Specifically, methods for the determination of cellular concentration, cell size distribution, single-cell physiology and time dependent changes in intracellular PHA content and the chelatable iron pool were advanced.

The next study was the development of a simple pH-stat fermentation strategy for production of *M. gryphiswaldense* MSR-1 and magnetosomes. Growth conditions were optimised with respect to biomass concentration, cellular magnetism (indicative of magnetosome production) and intracellular iron concentration using the previously developed flow cytometry analytics. High biomass and cellular iron contents of 4.2 g dry cell weight per litre and 33.1 milligrams per gram dry cell weight respectively were obtained.

The final piece of work describes the systematic advance of a fully scalable platform for extraction, recovery and purification of magnetosomes. The approach comprises single pass disruption of exponential phase *Magnetospirillum gryphiswaldense* MSR-1 cells in a commercial high pressure homogenizer, recovery and partial purification of magnetosomes by high gradient magnetic fishing in an automated 'state-of-the-art' magnetic separator, and final purification by magnetic micellar aqueous two phase separation. A magnetosome yield of nearly 45% was achieved, with 98.5% and >99% removal of polyhydroxyalkanoate and protein respectively. The process developed affords the potential for 'end-to-end' continuous manufacture.

Dedication

To my parents, other people in my family and my friends

for all the love and supports

Acknowledgements

I would like to thank my supervisor, Professor Owen Thomas, who has supported my PhD life, taught me knowledge of scientific thinking, accurate experiment manipulation, proper attitude of research and even English language from his valuable guidance. I would also like to thank Dr. Timothy Overton for the supervision and assistance during my PhD studies. I am also grateful to Dr. Alfred Fernandez-Castane for the help of my experiments, reports and scientific plan during my PhD. We worked very closely together on ProSeCa project which involved many cell cultivations, separations and analyses. Together, we published two papers which were put in this thesis as Chapter 2 & 3.

I am grateful to Elaine Mitchell, Veronica Baglin and David French for their support and advice in the laboratories. I would like to thank my friends Stephan Joseph and Ikhlaas Kasli who helped me improve my English very much. I would also like to thank all the former and current members in our research group for their kind help.

I would like to acknowledge Professor Matthias Franzreb for his guidance on the high gradient magnetic fishing and micellar aqueous two-phase system parts of this study, and also for providing the Eumulgin ES.

Table of Contents

List of Figures

List of Tables

Abbreviations

AAS	atomic absorption spectroscopy
ABI	5-aminobenzimidazol
ACA	activated charcoal agar
ATPES-PGA	3-aminopropyltriethoxysilane polyglutaraldehyde
ATPS	aqueous two-phase system
BOX	bis-(1,3-dibutylbarbituric Acid) trimethine oxonol
CFU	colony forming unit
CIP	clean-in-place
C_{mag}	cellular magnetism
CSCD	constant system cell disruptor
DCW	dry cell weight
DEAP	N,N-diethyl-1,3-propanediamine
DMSO	Dimethyl sulfoxide
DNA	deoxyribonucleic acid
DSP	downstream processing
DTT	1,4-dithiothreitol
eCG	equine chorionic gonadotropin
EDTA	ethylenediaminetetraacetic acid
EPPTMS	3-(2,3-epoxypropoxy) –propyltrimethoxysilane
ERA-IB	European research area industrial biotechnology
FCM	flow cytometry
FSC	forward light scatter
FSM	flask standard medium

GC-MS	gas chromatography-mass spectrometry
GFP-His_6	His_6-tagged green fluorescent protein
GTP	guanosine triphosphate
HEPES	4-(2-hydroxyethyl)-1-piperazineethanesulfonic acid
HGMF	high gradient magnetic fishing
HGMS	high gradient magnetic separator
IDA-Cu^{2+}	iminodiacetic acid charged with Cu^{2+} ions
IMEO	3-(2-imidazoline-1-yl) propyl-triethoxysilane
LC-MS	liquid chromatography-mass spectrometry
LSM	large scale medium
MACS	magnetic-activated cell sorter
MAH	methacryloly-L-histidinemethylester
MEP	mercaptoethylpyridine
MMIX	magnetic micro-ion exchangers
MMP	magnetosome membrane protein
MTB	magnetotactic bacteria
NIR	near-infrared
OD	optical density
OFM	optimized fermentation medium
pAAc	polyacrylic acid
PAGE	polyacrylamide gel electrophoresis
PBS	phosphate-buffered saline
PCR	polymerase chain reaction
PEDMAH	poly(ethylene glycol dimethacrylate-N-methacryloyl-L-histidinemethylester)

PEG	polyethylene glycol
PGAF	polyglutaraldehyde-coated aminosilanised ferrites
PG-SK	Phen Green™ SK
PHA	polyhydroxyalkanoates
PHEMA-EGDMA	poly(2-hydroxyethyl methacrylate ethylene glycol dimethacrylate)
PI	propidium iodide
PMA-DVB	poly(methacrylate-divinylbezene)
PMMA_NIPAAm-AAc	poly(methyl methacrylate) core N-isoproylacrylamide-co-acrylic acid shell
PMSF	phenylmethylsulfonyl fluoride
PVA	polyvinyl alcohol
PVAc-DVB	poly(vinyl acetate-divinylbenzene)
Pyr-546	pyrromethene-546
SAR	specific absorption rate
SDS	sodium dodecyl sulphate
SSC	side scatter
SSD	stable single-domain
TEM	transmission electron microscopy
VBNC	Viable but non-culturable
WCW	wet cell weight

CHAPTER 1

Introduction

1.1 Project overview

The extraction of biopharmaceuticals from blood and tissues is costly in terms of both labour and equipment, because of low purification power and low product yields in downstream processing steps. Magnetic separation techniques, especially via magnetic affinity adsorbents is a highly promising approach, which can extract proteins in serum efficiently with advantages including fast loading and washing flowrates, and easy removal of impurities.

The whole project is funded by European Research Area Industrial Biotechnology (ERA-IB) and the aim is the “recovery of high value proteins from serum by innovative direct capture techniques”, called ProSeCa in one word, which applies the production of protein based veterinary medicines from horse sera, via chemical, biological, or mixed biological/chemical magnetic supports. This research focuses on manufacturing biological magnetic particles produced by magnetotactic bacteria (MTB), with the aim of producing those particles with lipid bilayer formation wrapped on each single particle, and separating those particles from other impurities in the bacteria using scalable methods with an efficient purification factor and high yield, whilst keeping the lipid bilayer on the particles intact to maintain the proteins *in situ*.

1.2 Biomolecule Adsorption by synthetic functionalized magnetic particles

Downstream processing (DSP) describes the recovery and purification operations that follow biochemical reactions, animal and plant cell culture and agriculture synthesis. The main purpose of DSP is to purify a given product and achieve a certain concentration (Thomas, 1998). The issues of low yield efficiency and high cost of downstream processing from raw materials to the final products are a direct consequence of the traditional applications of

using separated, sequential unit operations, including cell broth separation, target molecule isolation from cells or cell free broth, and selective operations for target molecule purification (Hubbuch, 2002). Those operations perform limited functions or even just a single function. Manufacturers of biopharmaceutical products are facing inevitable pressures to reduce cost and improve purification efficiency in terms of time and yield, since the purification of a biopharmaceutical product can often account for 80% of the total production costs (Thomas, 1998). Thus, new technologies with functions of process reduction, yield improvement, plant size reduction and cost savings are significant. It is clear that the key to reduce the costs of downstream processing is to cut the number of employed unit operations.

The techniques include affinity tangential flow filtration, which combine the separation and concentration of biological molecules and affinity interactions of high value target molecules (Grzenia et al., 2008), and new porous-chromatography methods including bi-layered chromatography for size-exclusion on the shell and ion-exchange in the middle to achieve filtration and molecule capture functions together (Karnchanasri, 2013), and temperature-controlled chromatography to enhance protein adsorption affinity (Cao et al., 2015).

The techniques also include non-porous magnetic-support adsorption, which can recover products from a crude feedstock with high flowrate. The applications include magnetic adsorbents with high gradient magnetic fishing (Franzreb et al., 2006; Hausmann et al., 2000), and magnetic adsorbents with aqueous two-phase system separation (Fischer et al., 2013). Those magnetic particle based separations become attractive in large-scale applications due to their characters of fast, gentle and compatible with complex biological suspensions and low-cost with magnetic based particles.

1.2.1 Magnetic separation history

Magnetic separation techniques possess attractive properties of high speed processes and highly selective removal from feedstocks. Interest in magnetism is long-standing: the name comes from the ancient Greek town of Magnesia, and the magnetic phenomenon was first described by Thales of Miletus in about 550 BC; the Chinese are reputed to have used the directional properties of magnets in 1st century BC. However, it was not until 1845 that Faraday discovered that all substances are, to varying degrees, susceptible to the influence of a magnetic field (Svoboda, 1987). The first patents on devices for separation and handling of magnetically susceptible solids for mineral applications appeared at the very beginning of 20th century. The spectrum of materials that could be handled by such early magnetic equipment was limited to relatively coarse (i.e. large) and moderately strongly magnetic materials; it was not until the 1960s that instruments capable of handling very small and weakly magnetic species began to emerge. Since then, progress in both the development and application of magnetic separation technology has been nothing short of spectacular. Magnetic separation technology is now of huge economic importance in many large-scale process industries (e.g. clay, minerals and nuclear processing) and also finds applications in municipal and industrial waste treatment (e.g. the Sirofloc process, which uses electrostatic adsorption to remove negatively-charged impurities, such as colour, bacteria, viruses and nucleic acids; (Moffat et al., 1994)). It has been firstly used to remove dissolved and colloidal biological material in waste water treatment in the 1940s (Pieter et al., 1991). But the technology did not attract other groups until Peter Dunnill and Malcolm Lilly at University College London (UCL) employed micron-sized functionalised magnetic adsorbents for enzyme immobilisation from crude feedstock in the early 1970s (Dunnill and Lilly, 1974; P J Halling and Dunnill, 1980; Robinson et al., 1973). The first commercially available supports of Enzacryl FEO-(M) and Magnogel appeared in the late 1970s (Franzreb et al., 2006).

1.2.2 Magnetic support materials

Commercial production of functionalized magnetic supports for use in biotechnological applications was initiated in the late 1970's. Since then, a bewildering array of magnetic nanoparticle (50-600 nm, mostly 50-200 nm), microparticle (0.25-10 µm, mostly 0.8-5 µm) and macroparticle (>>10 µm) support materials have become available (Mair et al., 2009; Plačková et al., 2017; Tsao and Lee, 2016).

In small-scale medico-diagnostic applications, high-cost, low-capacity, single-use particles can be employed. For large-scale applications, however, adsorbents should : (i) be cheap and easy to manufacture in bulk quantities; (ii) possess sufficiently high specific surface areas to ensure satisfactory target-binding capacities; (iii) exhibit low nonspecific binding; (iv) be physically and chemically robust, easy to clean and reusable; and (v) be homogeneous with respect to size, shape, density and magnetic susceptibility, on a batch-to-batch basis (Bechstein et al., 2015; Franzreb et al., 2006; Gomes et al., 2018).

The simplest magnetic support materials used in bioprocessing was naked iron oxide particles, such as magnetite. Due to their very low cost, such materials have been extensively used in large-scale wastewater treatment for the nonspecific, reversible adsorption of cells and/or organic materials (Pieters et al. 1991). However, for use as a selective separation phase, the surface of the magnetic particle must be correctly covered and functionalized with an appropriated ligand.

1.2.3 Magnetic adsorbent particles for biomolecules purification

Adsorbents for protein separations generally use expensive and robust synthetic ligands, in order to achieve functions of chromatographic media, such as affinity, ionic exchange and hydrophobic interactions.

High binding capacities have been described extensively among magnetic adsorbent particles. Franzreb and co-workers reported that they attained a binding capacity of 180 mg g^{-1} magnetic beads for His_6-tagged green fluorescent protein (GFP-His_6) through iminodiacetic acid charged with Cu^{2+} ions (IDA-Cu^{2+}) on poly(methacrylate-divinylbenzene) (PMA-DVB) particles from *E. coli* homogenate (Franzreb, 2003). Another report announced that a binding capacity of 218.7 mg g^{-1} for bovine haemoglobin (BHb) through IDA-Cu^{2+} ligands on poly(glycidyl methacrylate) (PGMA) particles was possible (Ma et al., 2005). Meyer and co-workers reported that they used magnetic micro-ion exchangers (MMIX) beads with sulphite ligands to purify lactoferrin, and found the binding capacity of 334.6 mg g^{-1} from pure lactoferrin, and 12.6 mg g^{-1} from whey (Meyer et al., 2007). Thomas' group completed the research of recovery of lactoferrin and lactoperoxidase from crude whey by employing polyacrylic acid (pAAc) functionalised magnetic polyvinyl alcohol (M-PVA) particles, and achieved binding capacities of 585 and 685 mg g^{-1}, respectively (Brown et al., 2013).

In recent years, the requirement of blood-derived proteins has grown quickly, while the production could not meet the need (Gomes et al., 2018). Odabaşi and Denizli employed poly(2-hydroxyethyl methacrylate) (PHEMA) based particles with DNA functionalisation to extract human IgG from systemic lupus erythematosus patient plasma, and realised a binding capacity of 47.5 mg g^{-1} (Odabaşi and Denizli, 2001). Another magnetic adsorbents used for human IgG purification was described by Özturk and co-workers. They applied poly(2-hydroxyethyl methacrylate ethylene glycol dimethacrylate) (PHEMA-EGDMA) with 3-(2-imidazolin-1-yl) propyl-triethoxysilane (IMEO) ligands, and reached a binding capacity of 55 mg g^{-1}(Öztürk et al., 2007). The recent paper for immunoglobulin purification was reported by Gomes and co-workers (Gomes et al., 2018). They used polyglutaraldehyde

(PG) coated, 4-mercaptoethylpyridine (MEP) linked superparamagnetic adsorbents to achieve a binding capacity of 214 mg g^{-1}. Müller and co-workers reported that they employed M-PVA based particles and achieved 3.2 mg g^{-1} of binding capacity on the glycoprotein equine chorionic gonadotropin (eCG) from horse serum (Müller et al., 2015). Table 1.1 presents a summary of biopharmaceutical proteins purified by magnetic adsorbents, and all the magnetic materials employed in those examples given in the table were synthetic.

Table 1.1. Summary of protein purification with magnetic adsorbents.

Target protein	Base particle	Coating /Encapsulation	Ligand	Source	Reference
Trypsin	Cation deficient magnetite*	PGAF	Benzamidine	Porcine pancreatin	(Hubbuch and Thomas, 2002)
Lactoperoxidase	Cation deficient magnetite	PGAF	$-SO_3^-$	Whey	(Heebøll - Nielsen et al., 2004)
Lactoperoxidase	Magnetite	PVA	pAAc	Whey	(Brown et al., 2013)
Lactoferrin	Magnetite	MMIX	$-SO_3^-$	Whey	(Meyer et al., 2007)
GFP-His_6	Magnetite	PVA	IDA-Cu^{2+}	*E. coli* homogenate	(Franzreb, 2003)
GFP-His_6	Cation deficient magnetite	PGAF	IDA-Cu^{2+}	*E. coli* homogenate	(Franzreb, 2003)
GFP-His_6	Magnetite	PMA-DVB	IDA-Cu^{2+}	*E. coli* homogenate	(Franzreb, 2003)
Mouse IgG2b	Magnetite	EPPTMS	Protein A	Cell culture supernatant	(Holschuh and Schwämmle, 2005)
Mouse IgG2a	Magnetite	PMA-DVB	Protein A	Mouse ascites	(Liu et al., 2004)
Rabbit IgG	Magnetite?	Cellulose	Protein A	Aqueous solution and	(Cao et al., 2007)

				rabbit serum	
Human IgG1	Magnetite[?]	PMMA-NIPPAm-AAc	COOH	CHO cell culture supernatant	(Borlido et al., 2013)
Human IgG	Magnetite	PEDMAH	MAH	Aqueous solution and/or human plasma	(Özkara et al., 2004)
Human IgG	Magnetite	PHEMA-EGDMA	IMEO	Aqueous solution and/or human plasma	(Öztürk et al., 2007)
IgG	Magnetite	Agarose	ABI	Mimetic serum	(Gu et al., 2016)
Human IgG	Magnetite[?]	PHEMA	DNA	Systemic lupus erythematosus patient plasma	(Odabaşi and Denizli, 2001)
Human IgG	Magnetite	PVAc-DVB	2-mercapto-nicotinic acid	Human serum	(Qian et al., 2010)
Rat IgG	Cation deficient magnetite	PGAF	MEP	Rabbit antiserum	(Gomes, 2006)
Ig	Cation deficient magnetite	PGAF	MEP	Rabbit antiserum	(Gomes et al., 2018)
Con. A	Cation deficient magnetite	PGAF	Dextran	Jack bean extract	(Heebøll-Nielsen et al., 2004)
Interferon α-2b	Magnetite	PVA	Anti-IFN α-2b IgG	*Pseudomonas sp.* Strain VG-84 crude cell lysate	(Cao et al., 2006)
eCG	Magnetite	PVA	DEAP	Pre-purified horse serum	(Müller et al., 2015)

* Impurity magnetite (magnetite/maghemite combination) contains substantial amounts of impurities, especially lepidocrocite (γ-FeOOH) and possibly ferrihydrite (Hubbuch, 2002).

? Base particles not described in detail

PGAF polyglutaraldehyde-coated aminosilanised ferrites, *PVA* polyvinyl alcohol, *PMA-DVB* poly(methacrylate-divinylbezene), *EPPTMS* 3-(2,3-epoxypropoxy)-propyltrimethoxysilane, *PMMA-NIPAAm-AAc* poly(methyl methacrylate) core N-isoproylacrylamide-co-acrylic acid shell, *PEDMAH* poly(ethylene glycol dimethacrylate-N-

methacryloyl-L-histidinemethylester), *PHEMA-EGDMA* poly(2-hydroxyethyl methacrylate ethylene glycol dimethacrylate), *PVAc-DVB* poly(vinyl acetate-divinylbenzene), *APTES-PGA* 3-aminopropyltriethoxysilane polyglutaraldehyde, *MMIX* magnetic micro-ion exchangers, *GFP-His$_6$* His$_6$-tagged green fluorescent protein, *eCG* equine chorionic gonadotropin, *IDA-Cu^{2+}* iminodiacetic acid charged with Cu^{2+} ions, *MAH* methacryloly-L-histidinemethylester, *IMEO* 3-(2-imidazoline-1-yl) propyl-triethoxysilane, *MEP* mercaptoethylpyridine, *DEAP* N,N-diethyl-1,3-propanediamine, *pAAc* polyacrylic acid, *ABI* 5-aminobenzimidazol

Those magnetic adsorbents were composed of magnetic core materials which were produced by encapsulation (P. J. Halling and Dunnill, 1980; Moffat et al., 1994) or infiltration (Hirschbein et al., 1982; Mosbach and Andersson, 1977), then the magnetic cores were coated in a variety of ways to accept ligand attachment, such as the examples in Table 1.1. All the coated particles possessed a diverse range of particle size, ligand density, specific surface area, magnetic properties, etc. Thus, attention shifted to biological ways to produce magnetic particles, and many researchers have focused on MTB as a potential replacement of synthetic production of magnetic particles, since the particles can be produced in similar size, and magnetic properties, and possess high specific surface area and concentrated ligand density.

1.3 Magnetic particles in magnetotactic bacteria

1.3.1 Magnetic field and magnetism

Magnetism is a class of physical phenomena that are mediated by magnetic field. In physics, several different types of magnetism are distinguished, including diamagnetism, paramagnetism, ferromagnetism, ferrimagnetism and superparamagnetism. Materials that exhibit ferromagnetism are attracted towards the magnetic field lines when placed in a magnetic field, and the induced force (magnetic moment) experienced is dependent on the strength and direction of the magnetic field. If an alternating magnetic field is applied to a ferromagnetic material, there will be a magnetization trace loop called a hysteresis loop

(shown as a grey area in Fig. 1.1) which can be used as magnetic “memory”. Ferrimagnetic materials display some magnetic moments that point in opposite directions but the opposing moments are smaller when an external magnetic field is applied. Paramagnetic materials respond linearly to an applied magnetic field and show weaker magnetic properties than ferromagnetic substances. Materials that oppose the applied magnetic field are said to be diamagnetic. Superparamagnetism is a property that the magnetic response to a supplied magnetic field is stronger than normal paramagnetic materials, but it does not exhibit magnetic memory. Superparamagnetic properties arise when the crystal size of ferromagnetic materials is below 3-50 nm (Marghussian, 2015). Some forms of magnetism are shown in Figure 1.1.

1.3.2 Significance and features of iron in organisms

MTB were first observed in marine sediments (Blakemore, 1975), and contained solid iron in the organisms with weak magnetic fields (0.1 gauss) (Frankel et al., 1979) that has been demonstrated in geomagnetic orientation (Frankel et al., 1979). The MTB can move at a speed nearly twice as fast as *E. coli*, although they are larger with less flagellar proteins (Sharma et al., 2008). The ability to be aligned and actively swim along the geomagnetic field or other magnetic fields has been discovered in intracellularly structured magnetic nanoparticles (Bazylinski and Wiliams, 2006), called mangetosomes, which are mostly nano-sized crystals of magnetic iron (magnetite (Fe_3O_4) or greigite (Fe_3S_4)), surrounded by a lipid bi-layer (Fe_3S_4) (Flies et al., 2005; Heywood et al., 1990; Lang et al., 2009; Schüler, 1999). Magnetite magnetosomes are the most widespread mineral produced by MTB (Moisescu et al., 2008), and is the only magnetic particle found in freshwater system among all MTB (Faivre et al., 2008).

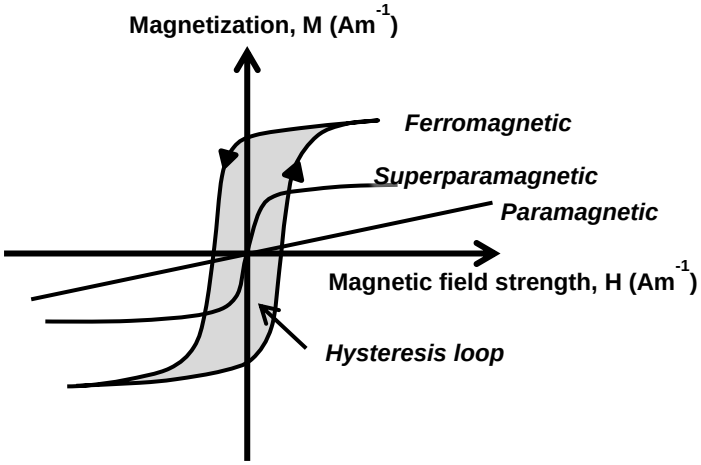

Figure 1.1. Magnetisation vs. field strength curves for ferro-, para- and superparamagnetic materials.

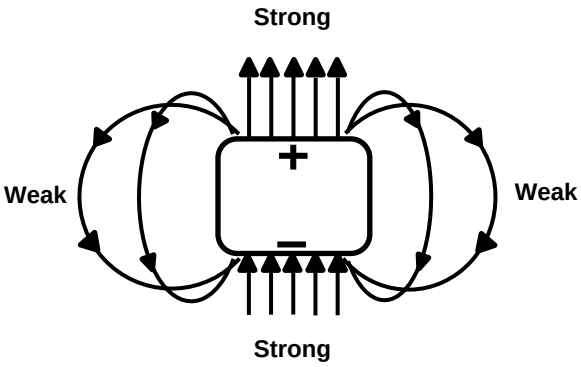

Figure 1.2. Single domain magnetic field of a single magnetic nanoparticle.

The magnetosome crystals are mostly found in a range of 35-120 nm (Bazylinski et al., 1994; Schüler, 2008; Vali and Kirschvink, 1990), except the very large ones which can reach up to 250 nm and are synthesized by uncultured coccus (Lins et al., 2006). Bacterial magnetosomes in the narrow range have been proven to be permanent, single-domain magnets at ambient temperature (Bazylinski and Frankel, 2004). In this range, particles were described to be stable single-domain (SSD) ferromagnets (Yoza et al., 2003) (Fig. 1.2) and thus, the magnetosomes possessed high magnetic coercivity (Baumgartner et al., 2013). Blakemore and Frankel (1981) first demonstrated that the magnetic particles were oriented in the {1 1 1} magnetic easy axis along the chain direction within the cell. This uniaxial geometry results in a magnetic dipole (Fischer et al., 2008), where it is believed this alignment permits the summation of individual magnetic moments of each particle, maximising the total cellular magnetic response (Uebe and Schüler, 2016). A number of reports have detailed varied morphologies of magnetosome crystals in MTB by transmission electron microscopy (TEM) (Lefèvre et al., 2011). The crystal shapes reported include rectangular (Schüler and Frankel, 1999), cubo-octahedral (Bazylinski et al., 1994; Lefèvre et al., 2011), elongated prismatic (Schüler, 2008; Schüler and Frankel, 1999) and bullet shaped (Bazylinski et al., 1994; Lefèvre et al., 2011) morphologies, and most of them are arranged

in one or multiple chains, which are parallel to each other and fixed to the shape of the cells (Lefèvre et al., 2011).

1.3.3 Formation of magnetic nanoparticles in magnetotactic bacteria

The mechanism of magnetosome formation has been researched by many groups (Faivre et al., 2008; Grünberg et al., 2004; Klumpp and Faivre, 2012; Matsunaga et al., 2007; Nguyen et al., 2016; Scheffel et al., 2008; Tanaka et al., 2011; Yang et al., 2010). Bazylinski and Schübbe (2007) reported that the mechanism of magnetosome formation could be a series

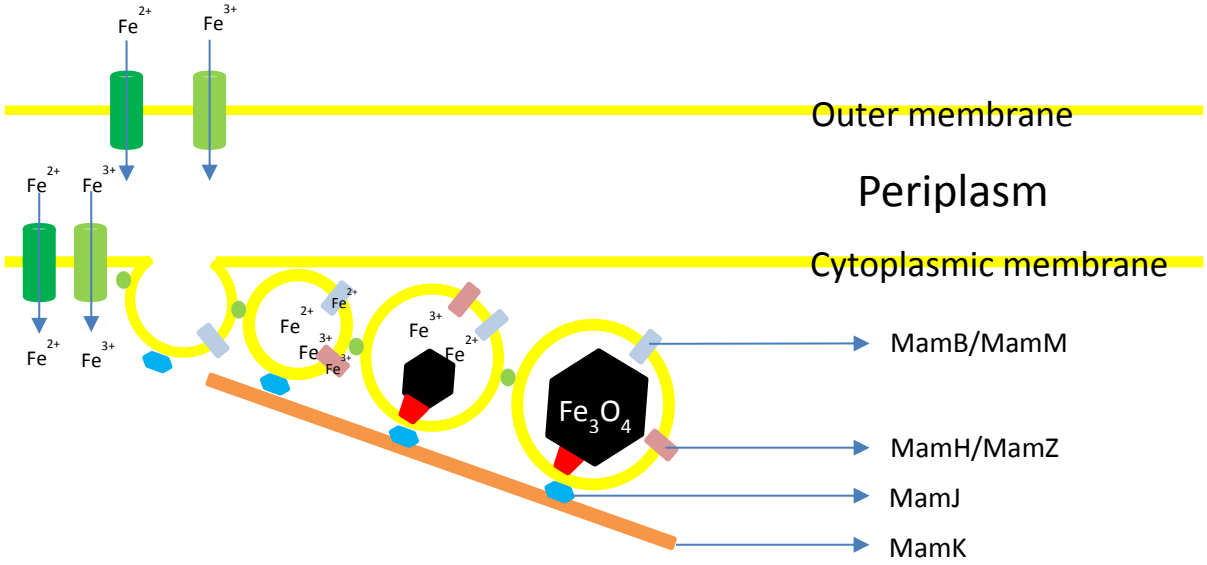

Figure 1.3. Possible magnetite crystal formation steps.

procedure including vesicle formation, iron uptake and transportation, and biologically controlled biomineralization. Yan and co-workers (2017) modelled the magnetosome formation into 4 steps: First, free iron including Fe^{2+} and Fe^{3+} are taken into the cells; Second, the magnetosome membrane forms and iron is transferred into the magnetosome membrane; Third, iron is biomineralized and localised on the inner side of magnetosome membrane; Fourth, every single magnetosome is aligned by a filament protein to control magnetosome chain assembly (Fig. 1.3).

Those steps include: (i), magnetosome membrane that compromises a proteinaceous phospholipid bilayer from cytoplasmic membrane (Gorby et al., 1988; Katzmann et al., 2010) by invagination is formed and MamB is a critical component of this process (Uebe and Schüler, 2016), a specifically denoted magnetosome protein by letter. (ii), at the same time, extracellular iron in both ferric and ferrous types is imported into the cytoplasm by transporters, and then transported into magnetosome membrane vesicles (probably by Mam B and MamM for Fe^{2+}, and MamH and MamZ for Fe^{3+} (Frankel et al., 1983; Raschdorf et al., 2013; Uebe et al., 2011)). (iii), nucleation of magnetite crystals occurs when soluble iron start to form crystalline iron phases. This happens in a narrow redox range (Fe^{3+} and Fe^{2+} are present at a ratio of 2/1), and high oxygen levels and oxidized carbon source are avoided (Heyen and Schüler, 2003; Katzmann et al., 2013; Li et al., 2014a, 2012; Y. Li et al., 2013). (iv), magnetosomes are arranged into linear chains that maximise the total magnetic response of the cell aligned cytoskeletal filaments which are formed by MamK (Grünberg et al., 2001; Schübbe et al., 2003). MamJ, an interacting partner of MamK has been confirmed as a connector that attaches magnetosomes to MamK, since magnetosomes magnetosomes aggregate by magnetic attraction and detach from MamK in the strains that is lack in MamJ (Scheffel et al., 2006; Scheffel and Schüler, 2007). However, there are still unclear factors in the steps of magnetosome formation. Although a significant accumulation of soluble iron has been observed in the magnetosomal vesicles recently

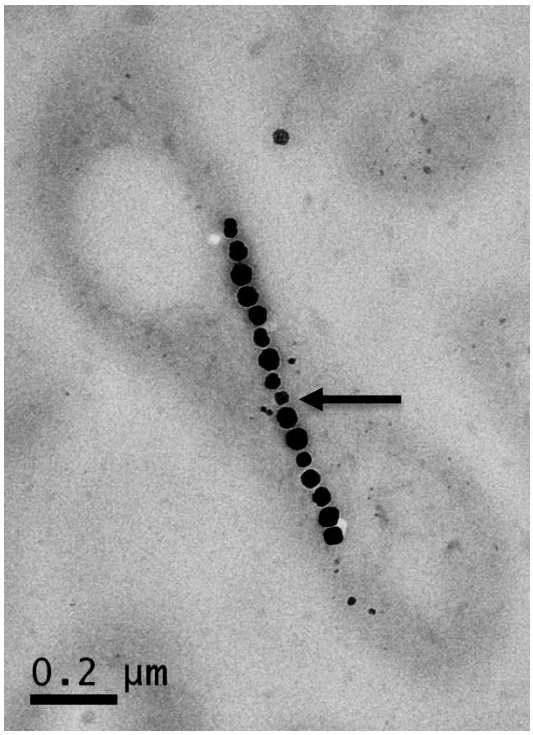

Figure 1.4. TEM image of *M. gryphiswaldense* strain MSR-1 with a magnetosome chain (black arrow).

(Werckmann et al., 2017), and then the nucleation occurs at the interface with the magnetosome membrane, as small nascent crystals in the lumen of magnetosome membrane vesicles have been found (Katzmann et al., 2010; Komeili et al., 2006), it is still not clear that how magnetite has been formed. MamE, Mam M and MamO are the candidate regulators, since magnetite biomineralization was abolished when those proteins were deleted in *M. magneticum* AMB-1 and *M. gryphiswaldense* MSR-1 mutant strains (Lohße et al., 2014; Murat et al., 2010; Uebe et al., 2011; Yang et al., 2010). Only one single crystal is formed in each magnetosome membrane vesicle and the crystal size distribution is also well controlled. Several single-deletion mutants of MTB have been described that smaller magnetite crystals were produced, including MamN, MamF or MamD-lack strains (Uebe and Schüler, 2016), but the factors that regulate crystal size are not well understood, as well as the optimal number of magnetite crystals. One of the reasons could be that only a limited number of MTB have been isolated (about 20) (Yan et al., 2017), such as *M. magneticum* AMB-1 (Matsunaga et al., 1991), *M. gryphiswaldense* MSR-1 (Schüler et al., 1999), *M. magnetotacticum* MS-1 (Maratea and Blakemore, 1981) and *Magnetospira thiophila* MMS-1 (Williams et al., 2012). Figure 1.4 shows a transmission electron microscopic (TEM) image of MTB with a magnetosome chain.

1.3.4 Potential applications of magnetosomes

After the discovery of MTB, it was not long that researchers turned to exploit their physical, magnetic and biomolecular applications. There are reports regarding the applications of magnetotactic bacteria, or magnetosomes, such as wastewater treatment, pathogen detection, cancer treatment and protein purification (Ali et al., 2018; Alphandéry et al., 2009; Chen et al., 2014; Lang and Schüler, 2006).

1.3.4.1 Wastewater treatment

MTB have been considered as bio-adsorbents for heavy metal removal and recovery from wastewater since early 1990's (Ali et al., 2018). The adsorption process of heavy metals has been studied to understand the removal mechanism. Different types of adsorption isotherms and kinetic models were investigated, and almost all of the studies supported Langmuir isotherm and pseudo-second-order kinetic mode (Ali et al., 2018; Cai et al., 2011; Song et al., 2008; Wang et al., 2011). Normally this type of adsorption is fast and reversible, and the equilibrium to adsorb Cu(II), Ag(I), Cr (VI) and Au(III) is achieved in 10 minutes (Cai et al., 2011; J. Li et al., 2013; Qu et al., 2014; Song et al., 2007; Wang et al., 2011). This may be due to the high specific surface area of the magnetosome membrane.

1.3.4.2 Pathogen detection and drug delivery

Due to the magnetosome membrane containing a large amount of amine and hydroxyl groups, it is promising to modify the surface of membrane in the application of pathogen detection (Peng et al., 2014). It has been reported that magnetosome-antibody complex combined with immunofluorescence have been effectively applied to detect the pathogenic bacteria (Nakamura et al., 1993). Rabbit anti-MO-1 cell polyclonal antibody decorated magnetosomes have also been employed for *staphylococcus aureus* isolation successfully as well (Chen et al., 2014). Since magnetosomes contain large amount of membrane proteins, it is also possible to conjugate drugs such as doxorubicin to the surface of magnetosomes (Sun et al., 2008; Sun et al., 2007) and deliver the drugs to its destination by magnetic field.

1.3.4.3 Cancer treatment

Magnetosomes, apart from the application of doxorubicin delivery discussed above, are also good candidates for cancer treatment by using their magnetic hyperthermia (Alphandéry, 2014). In the magnetic hyperthermia procedure, tumour cells are destroyed completely, or reduced in size within the temperature range of 37-45°C (Alphandéry et al., 2012; Hamdous et al., 2017; Lee et al., 2015; Mathuriya, 2016). The research group has focused on heat production by extracted magnetosome chains (Alphandéry et al., 2011), and the specific absorption rate (SAR) generated hysteresis loss is much larger than that has been reported from superparamagnetic nanoparticles (Brusentsov et al., 2001; Ma et al., 2004). Alpandéry and co-workers have used about 1 mg extracted magnetosome chains from *M. magneticum* AMB-1 bacteria to produce heat and eliminate breast cancer cells successfully under the skin of a mouse (Alphandéry et al., 2011), and found out that the efficiency of heat production by chains of magnetosomes was higher than the heat produced by aggregated magnetosomes without a magnetosome membrane (Alphandéry et al., 2012).

A new method of therapeutic hyperthermia for cancer treatment by magnetosomes has been studied recently, called photothermal therapy. This therapy requires a near-infrared (NIR) light to generate heat, instead of providing an alternating magnetic field. Chen and co-workers noticed that magnetosomes can convert the energy of 808 nm near-infrared (NIR) light into heat rapidly (Chen et al., 2016). A further research illustrated that the NIR light at 808 nm with magnetic targeting can induce a complete tumour elimination *in vivo* (Wang et al., 2018). Plan Sangnier and co-workers (2018) compared the heat production results *in vitro* and *in vivo* by adding a magnetic field and NIR light at 808 nm on magnetosomes, and demonstrated that by achieving the same temperature elevation, photothermia required lower concentration of magnetosomes, indicating that photothermia revealed more efficient performance against cancer treatment.

1.3.4.4 Gene research

Bacterial magnetite nanoparticles have been applied as gene carriers and detectors of nucleic acids (Maruyama et al., 2004; Ota et al., 2003; Tanaka et al., 2003). Matsunaga and co-workers reported that these nanoparticles can be employed as genus specific oligonucleotide probes in order to detect cyanobacterial DNA as DNA microarray (Matsunaga et al., 2001). mRNA isolation and DNA extraction by oligo-modified magnetosomes have also been reported (Sode et al., 1993). Additionally, the purification of DNA with dendrimer-modified magnetosomes magnetic nanoparticles were 7-11 times higher compared with man-made magnetic particles (Yoza et al., 2003). Magnetosomes have also been compared with artificial magnetic particles for enzyme immobilisation, and Matsunaga and co-workers reported that the amount of immobilized enzyme on magnetosomes was 40-100 times higher than that on man-made magnetic particles (Matsunaga et al., 1996).

1.3.4.5 Protein immobilisation and purification

Because of the membrane covered on magnetic nanoparticles, another biotechnological applications of magnetosome are based on immobilisation of proteins, peptides and enzymes (Lang and Schüler, 2006). They also reported the localisation of fusion proteins on magnetosomes is MamC by tagging green fluorescent protein (Lang and Schüler, 2008), and demonstrated the promising functionalisation of magnetosomes for protein purification in the future.

It has been reported that extracted magnetosomes can immobilise 40-100 times more than man-made Zn-Fe magnetic particles for glucose oxidase and uricase immobilisation

(Matsunaga et al., 1996). Immunoassays have also been researched using magnetosomes. One method of immunoglobulin immobilisation was that magnetosomes was first conjugated with antibodies, and then the antibody-magnetosome conjugates were employed to bind immunoglobulin, and the sensitivity of immunoglobulin determination was 4-10 times higher than previous reported methods (Nakamura et al., 1993). Another report for human insulin determination was reported by Tanaka and Matsunaga (2000). The authors used antibody-protein A-magnetosome complexes to detect human insulin, and found that the immunoreaction was as sensitive as gas chromatography-mass spectrometry (GC-MS) or liquid chromatography-mass spectrometry (LC-MS) method including the ability to examine multiple samples in a single assay. 17β-estradiol (E2) can be tested in half an hour in a detectable concentration of 20 ppt by employing anti-E2 monoclonal antibody immobilised magnetosomes (Tanaka et al., 2004b). As it is feasible to functionalised protein A and antibodies on the biologically magnetic nanoparticles, the applications for protein purifications using magnetosomes is particularly promising.

Thus, unique properties of magnetosomes, not normally associated with chemically synthesized magnetic nanoparticles, of narrow size distribution, permanent ferromagnetic character uniform morphology, fast absorption rate on metal ions, high heating capacity by magnetic field and NIR light and high specific surface area make them hugely attractive prospects for biotechnology and healthcare applications.

1.4 Production and purification of biological magnetic nanoparticles

It is recognised that the widespread application of magnetosomes will, to a large extent, depend on the development of intensified high yielding manufacturing platforms for magnetotactic bacteria (Jacob and Suthindhiran, 2016; Yan et al., 2012). After biomass

collection from fermentation, the extraction of magnetosomes has also been researched in many groups, but most of the reports showed limited scale of extraction, and the yields of magnetosomes were not very clear (Alphandéry et al., 2011; Gorby et al., 1988; Grünberg et al., 2001; Xiang et al., 2007).

1.4.1 MTB biomass manufacture and magnetosome production

As the purely separated MTB strains are limited (Yan et al., 2017), there are very limited choices for magnetosome production. Blakemore and co-workers firstly reported that *M. magnetotacticum* did not grow in medium with free exchange to air (Blakemore et al., 1979). *M. magneticum* AMB-1 has studied to produces magnetosomes only under microaerobic condition (O_2 ≤ 1%) (Yang et al., 2001), although early investigation reported that the magnetic bacteria can grow under aerobic condition (Matsunaga et al., 1991). Schüler and Baeuerlein (1997) have grown *Magnetospirillum gryphiswaldense* MSR-1 in pure culture and received a cell yield of 0.40 g L^{-1} in dry weight. They also cultured MSR-1 cells in batch fermentation in 5-L bioreactor starting from oxygen saturated condition, and found out that magnetic particles can only form when oxygen concentration decreased to 2-7 μM (less than 3 % saturation), although free iron can be taken from medium at the beginning of the experiment (Schuler and Baeuerlein, 1998). Heyen and Schüler (2003) optimised media called flask standard medium (FSM) using L-lactate and ferric citrate as carbon source and iron source, respectively, and enhanced growth conditions under oxystat condition for *M. gryphiswaldense* MSR-1 in flask and bioreactor. They reported that MSR-1 had high oxygen tolerance (0.25-150 mbar), but magnetosomes only can be produced when oxygen concentration was less than 20 mbar (2 % saturation), and got a maximum yield of 6.3 mg magnetite L^{-1} day^{-1}.

Sun and co-workers successfully employed a 42-L fermentor to produce *M. gryphiswaldense* in 60-h cultivation(Sun et al., 2008). They employed lactate and ferric citrate as carbon and iron sources, respectively, and kept pH stable at 7.0 by using 10% HCl during fermentation. They measured concentration of lactate every 2 h in the fermentation and kept its concentration constant by adding a substrate containing lactate, ammonium sulphate and ferric citrate, and achieved optical density at 565 nm (OD_{565}) 7.24, which was 2.17 gram of dry cell weight (DCW) per litre, and attained a yield of magnetosomes 41.7 mg L^{-1} in dry weight, or 16.7 mg L^{-1} day^{-1}. Another publication of culture of *M. gryphiswaldense* MSR-1 worked on feeding strategy in 42-L fed-batch fermentation (Zhang et al., 2011). They optimised the feed which contained lactate and ferric chloride as carbon and iron sources, respectively, and achieved magnetosome yield of 356.52 mg L^{-1} (178.26 mg L^{-1} day^{-1}) after 44-h cultivation, while the OD_{565} was 42. Schüler's group recently reported a magnetosome overproduction method by genomic amplification of biosynthesis-related gene clusters and increased magnetosome production 2.2 times more than their previous achievement (Lohße et al., 2016). This research makes a promising outlook of biological magnetic nanoparticles in the future.

Apart from cultivation of *M. gryphiswaldense* MSR-1, other strains of MTB have not been widely reported in pilot scale production, because Heyen and Schüler (2003) have reported that *M. gryphiswaldense* strain MSR-1 had the highest oxygen tolerance, and highest magnetosome yield under the same cultural condition, compared with *M. magnetotacticum*, *M. magneticum*, although Silva and co-workers have investigated *Magnetovibrio blakemorei* strain MV-1 in 5-L bioreactor and achieved magnetite concentration of 64.35 mg L^{-1}, or a yield of 16.09 mg L^{-1} day^{-1} (Silva et al., 2013). Table 1.2 shows a summary of magnetosome production.

Table 1.2 Yields of cells and magnetosomes summary

Strain	Culture time (h)	Cell yield (g L^{-1})	Magnetosome yield (mg L^{-1})	Reference
MS-1	96-144	0.4*	/	(Noguchi et al., 1999)
MSR-1	40	4.76	/	(Yang et al., 2013)
MS-1	48	0.32	3.4	(Yang et al., 2001)
AMB-1	48	0.48	4.7	(Heyen and Schüler, 2003)
MSR-1	30	0.40	7.9	(Heyen and Schüler, 2003)
AMB-1	96	0.58	14.8	(Yang et al., 2001)
MSR-1	60	2.17	41.7	(Sun et al., 2008)
MV-1	96	/	64.35	(Silva et al., 2013)
MSR-1	44	9.16	356.52	(Zhang et al., 2011)

* Wet weight, whilst the others are dry weights.

1.4.2 Magnetosome release and recovery

1.4.2.1 Cell disruption and magnetosome release

Cell disruption is the first important step for collecting biomolecular nanoparticles from magnetotactic bacteria, after cell harvest and collection. The purpose of cell disruption is to break the cell wall and/or membrane, or open gates to allow the target extracts to be released. There are many different methods for disruption. Mechanically, cells can be disrupted by liquid shear force which is generated by pressure or mechanical wave acting on liquid. This includes ultrasonication, French press, and bead mill. Another mechanical cell disruption techniques employs solid shear on frozen cells by high pressure compression of a mixture of ice crystals, especially in dry ice to ~243 K (Hughes et al., 1971). non-mechanically, there are chemical, enzymatic and physical ways for cell lysis (Theodossiou et al., 1997). Chemical lysis includes the employments of acids, alkalis, organic solvents and

surfactants. Enzymatic lysis employs the characters that enzymes, such as glycosidases, proteases and cellulases, are able to hydrolyse the wall of microbial cells. Physical lysis, such as cold osmotic shock and freeze-thawing, can be a potential method for animal cells, but not for microorganisms which have tough cell walls.

Sonication is a general and mature technique for cell disruption. Kobayashi and co-workers (2006) used a probe sonicator and compared several different pulse frequency to approach the *Magnetospirillum magnetotacticum* strain MS-1 by separating the same batch of cells in several aliquots and using different procedures, such as different frequencies for different operation times with and without treatment of sodium dodecyl sulphate (SDS). In order to check the efficacy of cell disruption in different methods, they examined the homogenate after disruption by TEM. Finally they believed that 200 pulses of 8 s each time without SDS was a good choice, because stronger or longer sonication, or SDS detergent lead to breakage of the magnetosome membrane and agglomeration of magnetosomes.

Alphandéry and co-workers employed an ultrasonic bath to disrupt *Magnetospirillum magneticum* AMB-1 (Alphandéry et al., 2009). They looked at a range of sonication time from 60 to 180 min at 30 W for breaking AMB-1 bacteria and they found 120 min to be the optimisation operation in another paper (Alphandéry et al., 2012). For sonication less than 60 min, the bacteria were not lysed efficiently, and for more than 180 min, agglomeration was observed which meant the membrane of magnetosomes was broken. Compare with probe sonication, cell disruption with ultrasonic bath takes much longer time to reach the similar disruption efficiency. This may be the frequency provided by ultrasonic bath is much lower than that supplied by probe sonicator, thus a much lower shear force was offered to the cell suspension.

Another series of methods which used French press at about 20,000 psi to disrupt cells is more generally accepted and used by researchers. The method can be first found in a paper written by Gorby and co-workers (1988). They harvested *Aquaspirillum magnetotacticum* MS-1 by centrifugation at 5000g and washed the pellets three times with 10 mM HEPES buffer containing 10 μg ml^{-1} phenylmethylsulfonyl fluoride (PMSF) which is a protease inhibitor, then they passed the cells through a French press three times at 18000 psi at a concentration of 10^{12} cells in 30 ml buffer. Similar disruption methods using a French press have been reported by other groups. For example, Schüler's group has employed French press at 20000 psi for three cycles to disrupt *Magnetospirillum gryphiswaldense* MSR-1 at a cell concentration of 10 g cells in wet weight in 50 ml HEPES buffer containing 0.1 mM PMSF (Grünberg et al., 2004). Ginet and co-workers employed French press for 3 times under a pressure of 1000 psi, but the concentration of cell suspension used for disruption was not very clear (Ginet et al., 2011). Another case which applied French press at 1000 psi for AMB-1 cell disruption has been reported, and the concentration of cell suspension was 1 g wet cell weight (WCW) in 10 ml HEPES buffer (Xiang et al., 2007).

The Chemical strategies for cell disruption have been reported a great deal, but it was difficult to find out the papers of chemical cell disruption of MTB. In early period, Neu and Heppel, (1965) reported a chemical disruption method by using 1 mM EDTA and 20% sucrose to give osmotic shock to *E. coli* for 10 min incubation. The result showed that the osmotic shock was efficient to release proteins in periplasm compared with ultrasonication, but not efficient to release proteins and DNA in cytoplasm.

Later, some researchers reported that they used a mixture of 1 mM EDTA, 20% sucrose and 500 μg ml^{-1} lysozyme to do the cell fractionation in large scale of cells from 5 l of culture (French et al., 1996). The release of some enzymes in periplasm by the compounds was higher compared with release by sonication, which meant that the compounds can release

periplasm proteins which were entrapped by peptidoglycan matrix. The efficacy of protein release in periplasm when incubating *E. coli* with water and sucrose separately had a higher protein release in a further research than the release while incubating the cells with sucrose only (Pierce et al., 1997). They also found a relation between the amount of lysozyme and DCW to optimise the protein release.

Other studies tested different combined chemicals to disrupt gram negative cells by using guanidine-HCl and/or Triton X-100 (Hettwer and Wang, 1989).They found that in a high concentration of guanidine (4 M), proteins in cytoplasm could be released about 50%.Triton X-100 cannot release proteins in cytoplasm by itself. But a combination of 0.1 M guanidine and 1-2 % of Triton X-100 could release similar amount of proteins from cytoplasm. The experiment showed that the 0.1 M guanidine open “gates” for Triton to go into the cells to inner membrane and disrupt it, although no changes could be seen in the outer membrane by TEM. This combination provided a very good strategy which contained a low concentration of guanidine to keep proteins active.

Research into MTB disruption by chemical means is very limited. This is largely because only chemicals most widely employed for disrupting other cell types (namely Triton, guanidine hydrochloride, EDTA and SDS) have been trialled thus far, and these have proved most damaging to magnetosome structures, i.e. solubilising the membranes and embedded magnetosome proteins coating individual magnetic crystals, leading to gross disruption of chain configuration and loss of magnetic memory (Grünberg et al., 2004; Kobayashi et al., 2006).

1.4.2.2 Magnetosome recovery after cell disruption

Magnetosome extraction is another important step for obtaining pure magnetosomes. The methods generally exploit the magnetic properties of the particle magnetization. According to the theoretically magnetic force, some researchers claimed that the effective magnetic field should be 1-10 T, and the problem was it was very difficult to collect magnetic materials from large volumes of solution (George et al., 1983). Some reports employed very low power centrifugation after cell disruption (Borg et al., 2015; Grünberg et al., 2004; Uebe et al., 2011) to separate cell debris from magnetic nanoparticles. Then the supernatant went

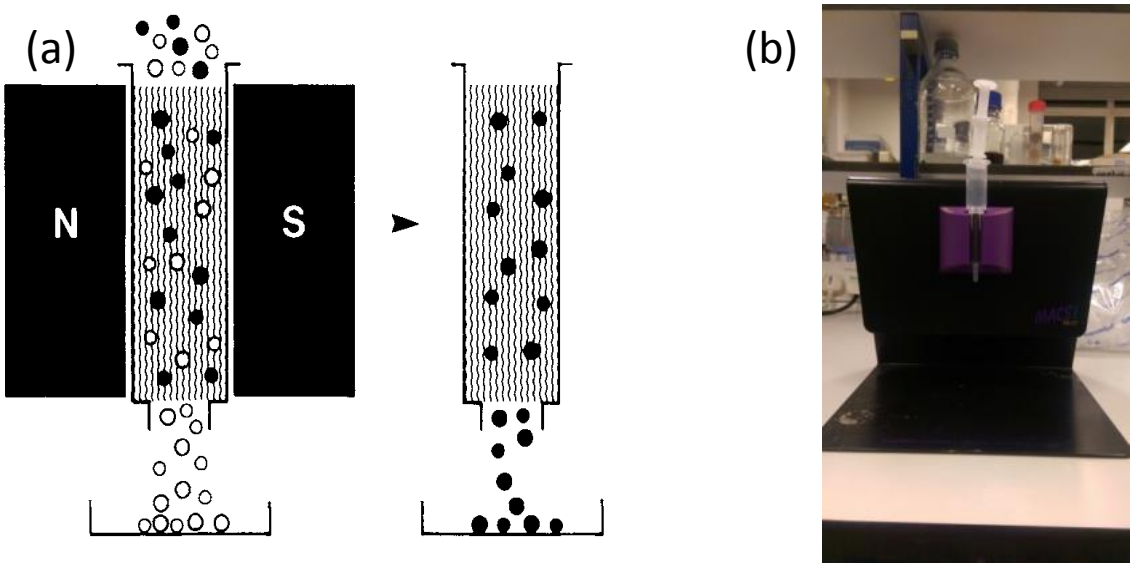

Figure 1.5. Magnetic cartridge for magnetic separation. (a), principle of magnetic separation (Miltenyi et al., 1990), (b), MACS cartridge and working stand (this work).

through a magnetic cartridge called a magnetic cell sorter (MACS) made by Miltenyi (Bergisch Gladbach, Germany) which has been firstly designed in the application of magnetic cell separation (Miltenyi et al., 1990) (Fig. 1.5a). Magnetosomes were kept on the columns when an Nd-Fe-B permanent magnet was around the column, while the soluble proteins cannot be retained. Then the magnetic nanoparticles were flushed off after the magnet was removed (Fig 1.5b). The eluted magnetosomes were centrifuged by high speed ultracentrifugation at more than 200,000 g through a sucrose cushion (60% [w/w]) to spin magnetosomes down and leave the residue of proteins on the surface (Grünberg et al.,

2004; Lang and Schüler, 2008; Uebe et al., 2011) in the final separation step. Other researchers employed serial washing steps for magnetosome recovery after magnetosomes were released from disrupted cells. Xiang and co-workers used 0.5 T Nd-Fe-B magnet after cell disruption, and took out the supernatant from the sample after magnetic particles were collected on one side of a tube, and then replaced same buffer into the sample with 10 times repeat (Xiang et al., 2007). Similar recovery methods have been reported by Alphandéry and co-workers (Alphandéry et al., 2012). They used a neodymium magnet (0.1-1 T) and separated the magnetosomes in homogenates after 10-20 times of washing steps. Gorby has reported the use of a 2 kG radar magnet to separate magnetosomes by 10 times washing steps, and then another 10 times washing steps after diluting the suspension in 100 times with a buffer containing 1 M NaCl for protein removal (Gorby et al., 1988).

One approach utilised a high-gradient magnetic filter (HGMF) that consisted of a ferromagnetic matrix and increases the volume of the chamber between the two poles of the magnet (George et al., 1983). Another publication mentioned two methods for magnetosome extraction (Setchell, 1985). The author mentioned a rotating drum magnetic separator which was similar to a continuous drum filter system to purify the magnetosomes. This method could approach very large quantity of magnetic particles and resulted in very concentrated solid contained solutions. But, if high yield of magnetosomes, or high purity was required, then high gradient magnetic separators (HGMS) provides a suitable option. Guo and co-workers published a route of magnetosome release and extraction in pilot scale (Guo et al., 2011). They have shortened the whole purification process and successfully managed to extract magnetosomes produced in a batch of 6-L *M. gryphiswaldense* culture in 2-5 days. All those methods mentioned in this paragraph have shown scalable magnetosome recovery potential, but no yield or purification factor has been reported.

As outlined above, it is clear that the data of magnetosome extraction and recovery is very limited. The efficiency of magnetosome release from MTB and the yield of magnetosome recovery requires further work. The situation of magnetosome chain configuration should also be considered during the whole production route. Thus, in this research, a completely scalable route of magnetosome production and purification was investigated, with consideration of the production of impurities such as PHA, the magnetosome chain configuration, magnetosome yield and purification factor.

1.5 Outline of the work

In this research, we employed *M. gryphiswaldense* strain MSR-1 to produce biomolecular magnetic nanoparticles, magnetosomes, and tried to understand the physiology and metabolism of the cells. Specifically, methods for the determination of cellular concentration, cell size distribution, single-cell physiology and time dependent changes in intracellular PHA content and the chelatable iron pool were advanced.

The next study was the development of a simple pH-stat fermentation strategy for production of *M. gryphiswaldense* MSR-1 and magnetosomes. Growth conditions were optimised with respect to biomass concentration, cellular magnetism (indicative of magnetosome production) and intracellular iron concentration using the previously developed flow cytometry analyses, and high biomass with high intracellular iron were obtained.

The final piece of work describes systematic advance of a fully scalable platform for extraction, recovery and purification of magnetosomes. The approach comprises single pass disruption of exponential phase *Magnetospirillum gryphiswaldense* MSR-1 cells in a commercial high pressure homogenizer, recovery and partial purification of magnetosomes

by high gradient magnetic fishing in an automated ‘state-of-the-art’ magnetic separator, and final purification by magnetic micellar aqueous two-phase separation.

By doing this, the work can contribute towards the development of industrially relevant processes for biomolecular magnetic particle manufacturing, hence developing the next generation of bio-based magnetic nanoparticles.

CHAPTER 2

Flow cytometry as a rapid analytical tool to determine cell physiology of *Magnetospirillum gryphiswaldense* MSR-1

Alfred Fernández-Castané, Hong Li, Owen R. T. Thomas and Tim W. Overton

A version of this manuscript has been published in

Scientific Reports in 2017

2.1 Introduction

Magnetic nanomaterials are increasingly important products with myriad applications in diverse settings including but not limited to environmental pollution control, information and energy storage (Frey et al., 2009), catalysis (Schatz et al., 2010), biotechnological (Fischer et al., 2013; Franzreb et al., 2006; Frey et al., 2009) and especially biomedical research (Frey et al., 2009; Pankhurst et al., 2009; Rui et al., 2010; Wilhelm et al., 2016). While most are produced by chemical means there is growing interest in harnessing the cellular machinery of certain naturally occurring bacteria (Alphandéry, 2014; Arakaki et al., 2008; Jacob and Suthindhiran, 2016; Yan et al., 2012) to generate useful magnetic, and other metallic nanoparticle materials, biologically. In this context, 'magnetosomes', magnetic nanoparticle based organelles naturally contained within magnetotactic bacteria (MTB), are particularly important (Barber-Zucker and Zarivach, 2017; Bazylinski and Frankel, 2004; Lang and Schüler, 2006; Pollithy et al., 2011; Pósfai et al., 2013; Uebe and Schüler, 2016). In most MTB, magnetosomes are arranged in one or more highly ordered 'compass needle-like' chains of single-domain permanently ferrimagnetic magnetite (Fe_3O_4) or greigite (Fe_3S_4) crystals (35–120 nm diameter) each wrapped in a phospholipid bilayer membrane containing a unique set of magnetosome specific proteins, i.e. distinct from those of cytoplasmic and outer membranes (Bazylinski and Frankel, 2004; Lang and Schüler, 2006; Raschdorf et al., 2013). These internal structures within MTB function as navigational devices essential for magnetotaxis (Frankel, 1984). Unique properties of magnetosomes, not normally associated with chemically synthesized magnetic nanoparticles, of narrow size distribution, uniform morphology, high crystal purity, permanent magnetic character, high heating capacity, low aggregation tendency, ready dispersion in aqueous solution, facile functionalization, high biocompatibility, low toxicity and high specific absorption rates (Jacob and Suthindhiran, 2016; Yan et al., 2012) make them especially attractive prospects for biotech and healthcare applications, i.e. in immunoassays (Wacker et al., 2007), magnetic affinity cell sorting (Yoshino et al., 2008), magnetic resonance imaging (Boucher et al., 2017), drug and gene

delivery (Tang et al., 2012) and cancer therapy (Felfoul et al., 2016; Jacob and Suthindhiran, 2016).

It is recognised that future widespread application of magnetosomes will, to a large extent, depend on the development of intensified high yielding manufacturing platforms for magnetosomes (Jacob and Suthindhiran, 2016; Uebe and Schüler, 2016; Yan et al., 2012). Fundamental to this are appropriate means for analysing MTB growth, viability, physiology and biomineralization of magnetic iron minerals, in order to understand and optimise magnetosome formation at any scale, from initial small (millilitre) studies on strain isolation and cultivability in the laboratory, and pilot scale manufacture (10–100 L), to fully fledged commercial production in cubic metre scale bioreactors. Qualitative evidence of magnetosome production within MTB can be obtained by observing a shimmering effect in cell suspensions mounted on magnetic stirrer plates, and black coloration of cell suspensions and/or colonies on agar plates, while magneto-spectrophotometric assay of cellular magnetism (C_{mag}) of suspended cells provides a rapid indirect measure of cellular magnetosome content (Lefèvre et al., 2009; Zhao et al., 2007). Quantitative determination of magnetosome content in cells and during subsequent recovery and purification operations usually involves measurement of iron content by means of atomic absorption spectrometry (dependent on species and cultivation conditions magnetosomes account for 80 to 99.5% of the total cell-bound iron in magnetic cells (Frankel, 1984; Grünberg et al., 2004; Heyen and Schüler, 2003), combined with imaging of magnetosomes by transmission electron microscopy. Recent work indicates the importance of monitoring physiological stress indicators to identify optimal conditions for magnetosome formation (Yang et al., 2013), and the utility of transcriptome analysis for comparing magnetosome forming and non-forming conditions in MTB (Wang et al., 2016). Other analytical methods especially pertinent to pilot- and large-scale magnetosome production and downstream processing from high biomass MTB fermentations include the tracking of polyhydroxyalkanoates (PHA) granules. Here,

PHA formation diverts cellular resources from growth, lowering yields, and high levels of PHA would be likely to be a troublesome contaminant of magnetosome preparations. Current procedures for the determination of PHA content employ lengthy procedures involving solvent extraction, derivatization and gas chromatography (Wang et al., 2016).

With the exception of at line optical density and C_{mag} measurements all of the aforementioned techniques are labour intensive and/or time consuming. The development of analytical methods is essential for the development of robust production processes, itself a requirement for industrialisation implementation. It is desirable that such methods will be rapid, requiring small volumes of samples and provide data of cellular parameters without the need of further growth, thus giving a 'snapshot' of the current physiological state of the cells. The flow cytometry (FCM) methods applied in this study fulfil these requirements. FCM has previously been applied previously for rapid analysis of microbial physiology (Geng et al., 2014) and expression of auto-fluorescent proteins (Lagendijk et al., 2010), monitoring recombinant protein production (Sevastsyanovich et al., 2009) and for investigating population heterogeneities in cultures. In FCM, multiple physical characteristics of single particles suspended in a fluid can be measured concurrently as they flow through a beam of light. FCM is a fast single-cell analysis technique well suited to collection of large datasets (tens of thousands of cells can be analysed) and allows determination of light scatter (relative size and granularity/internal complexity) and fluorescence properties of individual cells and thus determination of population heterogeneity. An important advantage of FCM is that it does not rely upon microbial growth for analysis of cell viability. 'Viable but non-culturable' (VBNC) cells exist within most microbial cell populations (Taimur Khan et al., 2010), but growth-based methods for determining viable cell numbers (total viable counts generating colony forming unit, CFU data) will not detect the VBNC phenotype, thus total viable cell concentrations are underestimated. FCM does not share this limitation. MTB grow very slowly on agar plates, for example, *M. gryphiswaldense* MSR-1 forms colonies after 7–

10 days (Heyen and Schüler, 2003). Regardless of cell type FCM analysis can be performed in a matter of seconds. Moreover, when combined with carefully selected mixtures of fluorescent probes FCM can be employed to determine the physiological state of single cells.

Reports on the application of FCM to MTB are few in number (Lang et al., 2009; Lang and Schüler, 2008) and the full power of the technique has not exploited in any case. FCM has been used for analysing gene expression in *M. gryphiswaldense* MSR-1 (Lang and Schüler, 2008), and in the development of new expression systems for the same species (Lang et al., 2009). Green fluorescent protein (GFP) was used as a reporter in both studies, i.e. for magnetosomal localization and expression of GFP tagged magnetosome proteins under magnetite forming conditions (Lang and Schüler, 2008); and for identification of promoters (fused to GFP) for efficient gene expression (Lang et al., 2009).

In this work, we present a battery of FCM methods tailored *a priori* to the study of *M. gryphiswaldense* MSR-1 and other MTB, and applicable to cells grown in liquid cultures and on agar plates. Specifically, we describe methods for determination of cellular concentration, cell size distribution, single-cell physiology and relative changes over time of intracellular contents of PHA and the chelatable iron pool.

2.2 Materials and methods

2.2.1 Strains, growth media and culture conditions

Magnetospirillum gryphiswaldense MSR-1 was obtained from Leibniz-DSMZ (Deutsche Sammlung van Mikroorganismen und Zellkulturen GmbH) and used in all experiments.

Unless otherwise indicated all chemicals were from Sigma-Aldrich Chemical Company Ltd (Gillingham, Dorset, UK). *M. gryphiswaldense* MSR-1 cells were grown on solid activated charcoal agar (ACA) plates and in liquid media. ACA plates contained 3 g L^{-1} activated charcoal. 15 g L^{-1} agar (Formedium, Hunstanton, Norfolk, UK), 0.1 g L^{-1} yeast extract, 3 g L^{-1} soybean peptone, 3 g L^{-1} sodium pyruvate, 0.34 g L^{-1} $NaNO_3$, 0.1 g L^{-1} KH_2PO_4, 0.15 g L^{-1} $MgSO_4 \cdot 7H_2O$ and 2.38 g L^{-1} 4-(2-Hydroxyethyl)piperazine-1-ethanesulfonic acid (HEPES) buffer in MiliQ water. The pH was adjusted to 7.0 with sodium hydroxide (Heyen and Schüler, 2003) before autoclaving. After autoclaving iron(III) citrate (final concentration of 500 µM) and 1.4-dithiothreitol (DTT; final concentration of 1 mM) were aseptically added to the plate mix before pouring (Schultheiss and Schüler, 2003). Set ACA plates were incubated at 30 °C in 12-plates anaerobic jars with one Anaerocult®C sachet (Merck Chemicals Ltd, Beeston Notts, UK) to achieve microaerobic conditions. Liquid cultures of *M. gryphiswaldense* MSR-1 were routinely grown in a shaking incubator (30 °C, 150 rpm) using a flask standard medium (FSM) composed of 0.1 g L^{-1} yeast extract, 3 g L^{-1} soybean peptone, 3.5 g L^{-1} potassium l-lactate, 100 µM iron(III) citrate, 0.34 g L^{-1} $NaNO_3$, 0.1 g L^{-1} KH_2PO_4, 0.15 g L^{-1} $MgSO_4 \cdot 7H_2O$, 5 mL L^{-1} of EDTA-chelated trace element mixture (Widdel and Bak, 1992) and 2.38 g L^{-1} HEPES buffer in deionized water; the whole adjusted to pH 7.0 prior to sterilization in an autoclave. Cells were grown at 30 °C in a shaking incubator at 150 rpm. O_2-limiting cultures were grown in tightly sealed screw cap 50 mL Falcon tubes with variable headspace volumes (10–40 mL), whereas aerobic cultivations were performed with 50 mL of media in 250 mL shake flasks allowing free air exchange. Non-magnetic cells were cultured in FSM without iron (FSM-Fe^-) for a minimum of three sequential sub-cultures in an attempt to eliminate all trace of the metal. Magnetic cells were obtained from cultures grown in bioreactor experiments under controlled conditions using a growth strategy adapted from previous works (Heyen and Schüler, 2003; Sun et al., 2008; Yang et al., 2013).

2.2.2 Flow cytometry (FCM)

Table 2.1. Fluorescent dyes used in this study. With the exception of Pyr-546 (Photonic Solutions, Ohio, USA) the listed dyes were acquired from Fisher Scientific (Loughborough, Leics, UK). The cited working concentrations were adapted from previous studies and/or optimised in this work.

Fluorescent dye	Excitation λmax, abs (nm)	Emission λmax, fl (nm)	Stock concentration	Solvent	Working concentration	Fluorescence channel
Bis-(1,3-dibutylbarbituric Acid) Trimethine Oxonol (BOX)	490	516	10 mg mL^{-1}	DMSO	100 ng mL^{-1}	FL1 (green)
Phen Green™ SK (PG-SK)	525	580	1 mM	DMSO	5 µM	FL1 (green)
Propidium iodide (PI)	533	617	200 µg mL^{-1}	H2O	100 ng mL^{-1}	FL3 (red)
Pyrromethene-546 (Pyr-546)	493	519	0.1 mg mL^{-1}	DMSO	0.5 µg mL^{-1}	FL1 (green)
Syto®9*	483	503	5 mM	DMSO	1 µM	N/A
Syto®62	652	676	5 mM	DMSO	0.4 µM	FL4 (far red)

*Syto® 9 was only used for fluorescence microscopy assays. N/A = not applicable.

Bacterial samples taken directly from agar plates or liquid cultures were resuspended in phosphate-buffered saline (PBS) and then analysed directly in a BD Accuri C6 flow cytometer (Becton, Dickinson and Company, Oxford, UK) for cell size and granularity, or after staining with various fluorescent dyes (see Table 2.1) using protocols developed and detailed in the Results and Discussion. During FCM on fluorescently labelled cells, samples were excited using a 488 nm solid-state laser and fluorescence was detected using two different filters, i.e.: a 533/30 BP filter (FL1-A) for bis (1.3-dibutybarbituric acid) trimethine

oxonol (referred to here as bis-oxonol or BOX), pyrromethene-546 (Pyr-546) and phen green™ SK (PG-SK); and a 670 LP filter (FL3-A) for propidium iodide (PI). Syto®62 was excited with a 640 nm solid-state laser and detected through a 675/25 BP filter (FL4-A).

2.2.3 Analytical methods

Culture optical densities were recorded at a wavelength of 565 nm (OD_{565}) in an Evolution 300 UV-Vis spectrophotometer (Thermo Fisher Scientific, Hemel Hempstead, Herts, UK) controlled by Thermo Scientific™ VISION*pro*™ software.

Cellular magnetic response (C_{mag}) values of cultures were determined immediately after OD_{565} measurements using a purpose-built magnetic measurement system mounted within the spectrophotometer. In common with previous magneto-spectrophotometry apparatus (Lefèvre et al., 2009; Zhao et al., 2007) our system features two pairs of Helmholtz coils arranged around the cuvette holder, one pair perpendicular to the light beam and the other in line with it. Each pair of coils is energized in turn, and the OD_{565} is measured in each condition. Magnetic cells will align with the magnetic field and thus orient in line with or perpendicular to the light beam; the optical density will therefore change between the two conditions. Non-magnetic cells do not align with the magnetic field, thus the optical density does not change on switching the field orientation. C_{mag} values for culture samples are calculated by dividing the OD_{565} values of suspensions of cells aligned parallel to the light beam by those obtained when the same cells are perpendicularly aligned. C_{mag} values greater than unity reflect the presence of magnetic cells.

Cellular morphology was routinely examined by light microscopy using an Olympus BX50 optical microscope (Olympus Corporation, Tokyo, Japan). Images were captured using a MotiCam 1 (800 × 600 pixel) camera (Microscope Systems Limited, Glasgow, UK) and processed with Motic Images Plus 2.0 software (Motic Europe S.L.U., Barcelona, Spain).

Cells stained with fluorescent probes were observed and imaged using a Zeiss Axiolab microscope (Carl Zeiss Ltd., Cambridge, UK) fitted with a Zeiss AxioCam ICm1 camera, and the images were processed in auto-exposure mode with the aid of Zeiss ZEN Lite 2012 software. Samples were excited with a Zeiss VHW 50f-2b ultraviolet light source and a 520 LP filter was employed for detection of fluorescence from Syto® 9 and pyrromethene-546 (Pyr-546).

2.3 Results and discussions

2.3.1 Morphological difference between cell growth on plates and in suspension

FCM analysis was employed to monitor cell size and optical complexity of *M. gryphiswaldense* MSR-1 by means of light scattering. In FCM, light scatter is collected at two different angles: in the direction of the laser path (forward light scatter, FSC); and orthogonal to it (side scatter, SSC). For spherical particles (e.g. of latex), FSC correlates with the logarithm of particle diameter (Day et al., 2002). For cells and other non-spherical particles, changes in FSC are roughly indicative of changes in cell size. When applied to cells, SSC measures 'granularity' (Lee et al., 2004), a parameter that includes optical complexity caused by particulate material contained within the cell. Figure 2.1 shows the results of comparative FCM scatter and light microscopic analyses of MSR-1 cells cultured on ACA plates (resuspended in PBS) and in the liquid medium FSM. Clear differences in the heterogeneity of cell populations cultured in FSM (Fig. 2.1a) *cf*. those grown on ACA (Fig.

2.1b) can be discerned from the scatter patterns of FSC vs. SSC dot plots (Fig. 2.1a and b). Larger cells are represented by high FSC-A values (y-axis) whereas more granular cells are characterized by higher SSC-A (x-axis) values. Cells grown in liquid FSM appear less heterogeneous, smaller and less granular than those grown on ACA plates. Moreover, differences in particle size distribution and cell shape of suspension and plate grown MSR-1 cells are respectively inferred from 'Count vs FSC-A' histograms and light microscopy, with plategrown cells appearing more polydisperse in size (Fig. 2.1c) and filamentous (Fig. 2.1e) compared to liquid-grown cells (Fig. 2.1d).

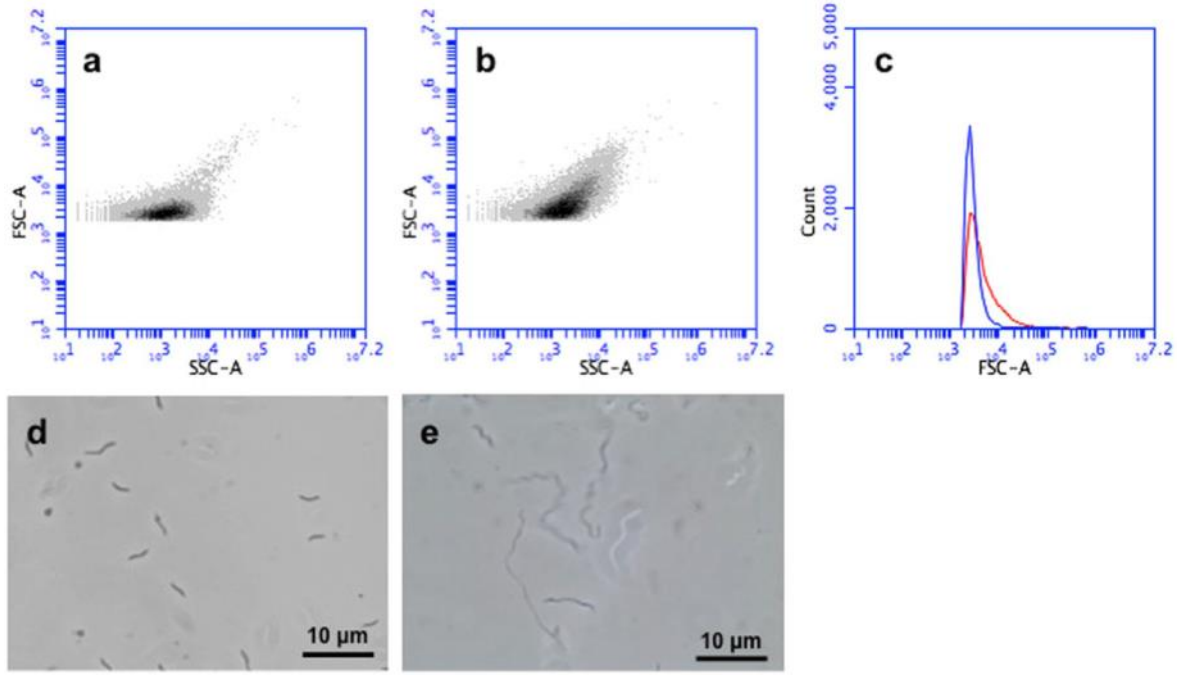

Figure 2.1. Analysis of M. gryphiswaldense MSR-1 using FSM and light microscopy. Scatter plots (Forward scatter, FSC-A vs. Side scatter, SSC-A) of cells cultured (a) in liquid FSM and (b) on ACA plates; (c) comparison of individual particle count vs FSC-A plots for plate (red trace) and liquid (blue trace) grown cells; light microscope images of (d) liquid and (e) plate grown cells.

2.3.2 Determination of cell concentration by FCM

FCM analysis was also used as a rapid method for determining cell concentrations in shake flask experiments. In auto-calibration mode and operating at a medium flow rate of 35

$\mu L \cdot min^{-1}$ a strong correlation ($R^2 > 0.94$) between OD_{565} and FCM event counts was observed for MSR-1 cells (Fig. 6.1a) with 1 OD_{565} equivalent to 1.16×10^9 cells mL^{-1}. This relationship is strikingly different to Schultheiss and Schüler's (Schultheiss and Schüler, 2003) correlation of OD_{565} with CFU, i.e. 1 OD_{565} equivalent to 3.3×10^8 CFU mL^{-1} and likely reflects an important advantage of FCM over CFU counting, namely its ability to detect viable but non-culturable cells (VBNC). We also used Syto®62, a permeant DNA dye, to stain MSR-1 cells and so distinguish them from noise particles of similar size; with Syto®62-stained cells a similar correlation was found between OD_{565} and cell count ($OD_{565} = 1.03 \times 10^9$ cells mL^{-1}; Fig. 6.1b).

2.3.3 Use of FCM to determine MSR-1 membrane polarization and cellular death

Two fluorescent probes were used to monitor the respiratory potential and death of *M. gryphiswaldense* MSR-1 cells using FCM. BOX (DiBac4 (Franzreb et al., 2006); bis-(1,3-dibutylbarbituric acid) trimethine oxonol) is a green lipophilic fluorescent probe that can only enter cells if their membranes are depolarized (Nebe-Von-Caron et al., 2000). Healthy cells possess intact polarized cytoplasmic membranes, which are impermeant to BOX (BOX^-). In contrast, cells with depolarised cytoplasmic membranes (whether injured, stressed or dead) permit BOX access and fluoresce green (BOX^+). PI (propidium iodide), a nucleic acid intercalator, is excluded by the intact membrane of viable cells (PI^-), but is taken up by dead cells with red fluorescence (PI^+) (Nebe-von-Caron et al., 2000). Staining procedures were optimised using actively growing *M. gryphiswaldense* cells, starving cells and dead cells killed with ethanol. Fig. 2.2 shows the two-colour fluorescence dot plots of MSR-1 cells co-stained with BOX and PI (fluorescence being detected on FL1-A and FL3-A channels, respectively). The fluorescence patterns from actively growing magnetic cells (Fig. 2.2a) and

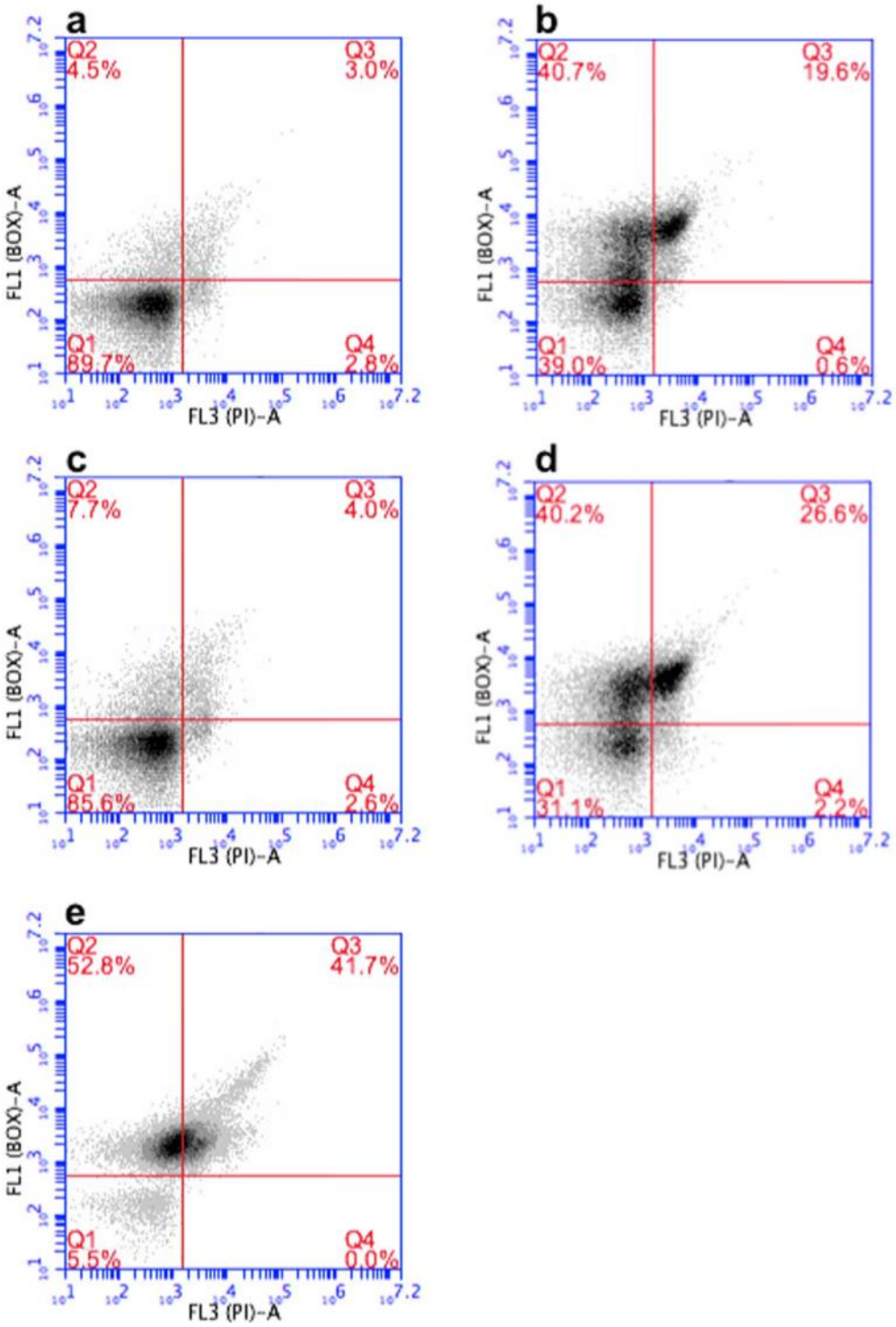

Figure 2.2. Viability analysis of MSR-1 cells using FCM. MSR-1 cells were co-stained with BOX (fluorescence measured on FL1-A channel, y axis) and PI (fluorescence measured on FL3-A channel, x axis). Key: (a) actively growing magnetic cells; (b) starving magnetic cells; (c) actively growing non-magnetic cells; (d) starving nonmagnetic cells; and (e) cells incubated with absolute ethanol for 10 minutes, centrifuged and then resuspended in phosphate buffered saline. The numbers of cells in each of the four quadrants of all plots are indicated in red font and are expressed as percentages of the total population.

non-magnetic cells (Fig. 2.2c) were strikingly alike; i.e.: 86–90% of the cell populations were 'healthy', staining negatively with both fluorescent markers (BOX^- PI^-, Quadrant 1); 5–8% were 'injured', staining positively with BOX, but negatively with PI (BOX^+ PI^-, Quadrant 2); and 3–4% were dead (BOX^+ PI^+, Quadrant 3). The fluorescence patterns from starving magnetic (Fig. 2.2b) and non-magnetic (Fig. 2.2d) MSR-1 cells were comparable with one another, but indicated noticeably fewer healthy populations (31–39% healthy, ~40% injured, 19–26% dead) than those of actively growing cells (~90% healthy, 5–8% injured, <3% dead). The low healthy population in starving cultures suggests the presence of large numbers of VBNC cells. This confirms the observation that the correlation between OD565 and cells mL^{-1} as measured by FCM is different to the correlation between OD565 and CFU mL^{-1} (Schultheiss and Schüler, 2003) due to the presence of VBNC cells. Only 5% of the positive control population, i.e. cells killed with ethanol, were healthy MSR-1 cells (Fig. 2.2e).

2.3.4 Accumulation of PHA aggregates in MSR-1

It has been widely reported that limiting nitrogen and O_2 availability under carbon excess results in high-level accumulation of polyhydroxyalkanoates (PHA) in several species of bacteria (Ban et al., 2010; García-Torreiro et al., 2016; Kessler and Witholt, 2001; Schultheiss et al., 2005; Ward et al., 1977). Ban et al., (2010) specifically examined the effect of hydrogen metabolism on cell growth and magnetosome synthesis in *M. gryphiswaldense* MSR-1 concluding that in MTBs PHA formation occurs under conditions of excess reducing power. Liu and co-workers (Liu et al., 2008) succeeded in isolating an MSR-1 mutant capable of higher level magnetosome production and lower PHA accumulation than the wild type, indicating a possible link between the formation of PHA and magnetosomes in this bacterium. In more recent work, genomic excision of the *phbCAB* operon in MSR-1 was shown to abolish PHA granule formation albeit at the expense of much reduced growth (Raschdorf et al., 2014). Collectively, the above findings hint at the

existence of an energy competition between the processes of PHA and magnetosome formation. Here we have used FCM to investigate PHA accumulation within individual bacteria of starved non-magnetic and magnetic MTB cultures. Cells were stained with the lipophilic dye 1,3,5,7,8-pentamethylpyrromethene-difluoroborate complex (pyrromethene-546 or Pyr-546) which on entering bacteria stains PHA green (Vizcaino-Caston et al., 2016). Previous studies have shown that Pyr-546 fluorescence correlates to intracellular PHA content (Kacmar et al., 2006) and is superior to Nile red as a dye for PHA. After incubating for various times (10–300 s) samples were immediately analysed by FCM. Figure 2.3 shows that when used at a concentration of 0.5 μg·mL^{-1} the timeframe for Pyr-546 penetration and

full staining of intracellular PHA was less than 1 min after adding the dye and analysing the sample. No further enhancement in fluorescence occurred between 70 and 300 s exposure

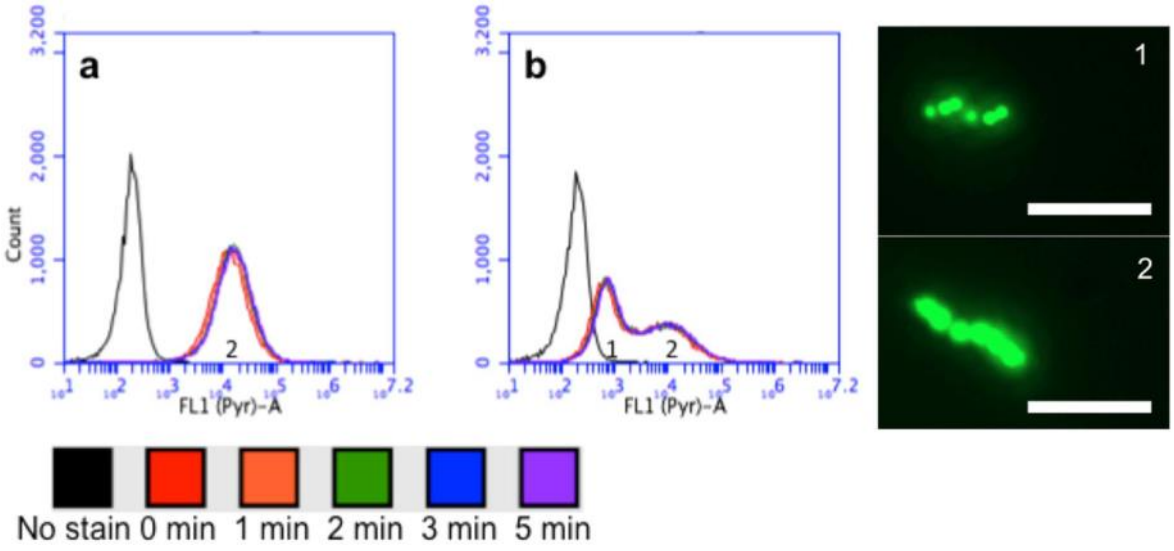

Figure 2.3. Analysis of PHA content using FCM. Fluorescence intensity histograms of starved (a) non-magnetic and (b) magnetic cells after staining with Pyr-546 (0.5 μg·mL^{-1}) for various times. The numbers '1' & '2' marked on the inserts and the fluorescence micrographs correspond to magnetic and non-magnetic cells, respectively to identify those with low and high PHA content. The scale bars indicate a length of 5 μm (*N.B.* All colourful traces superimpose on one another).

to Pyr-546 for both non-magnetic (Fig. 2.3a) and magnetic (Fig. 2.3b) cells. This said, FCM analysis reveals salient differences in the PHA content of magnetic and non-magnetic MSR-

1, for example, revealing the presence of two discrete populations with low (Fig. 2.3b, labelled '1') and high (Fig. 2.3b, labelled '2') PHA content in magnetic cells *cf*. just a single 'high PHA' population in non-magnetic cells (Fig. 2.3a marked '2'). Fluorescence microscopy images of cells containing different quantities of Pyr-546 stained PHA are shown in Fig. 2.3. Similarly to our findings, recent studies performed with *Cupriavidus necator* observed sub-populations with more and less PHA (Vizcaino-Caston et al., 2016). Other works with *Pseudomonas putida* have recently observed an asymmetric PHA distribution during cell division under carbon limiting conditions suggesting that this could be explained by different cellular growth rates, distinct ability to degrade PHA or uneven distribution of PHA granules to daughter cells (Karmann et al., 2017).

2.3.5 Measurement of intracellular chelatable iron

The intracellular pool of chelatable iron is considered a critical component in the biomineralization of magnetosomes. Recent studies in *M. gryphiswaldense* MSR-1 suggest that at least some of the iron transport for magnetite synthesis occurs through two copies of the ferrous iron transporter FeoB which is common to most bacteria. Strains lacking *feoB1* (Rong et al., 2008) and *feoB2* (Rong et al., 2012) were found to have lower magnetite contents than the wild type. Deletion of the iron response regulator, Fur, which activates *feoB1* and *feoB2* also resulted in reduced magnetosome formation (Uebe et al., 2010). All the above studies compare magnetosome production of wild type and 'deficient' strains, but do not provide dynamic measurements of iron transport in MSR-1. Moreover, it is well known that biomineralization depends not only on iron, but also on O_2 availability (Heyen and Schüler, 2003; Schüler and Baeuerlein, 1998).

Typically, magnetosome production is quantified off-line (by measuring the iron content in cells using atomic absorption spectroscopy), and is backed up by visualization of magnetosomes under the transmission electron microscope. In both cases sample preparation and analysis are laborious and time consuming. Therefore there is clearly need of rapid new methods to interrogate and quantify magnetosome production and biomineralization in MTBs, as well as inform the development and optimization of large-scale magnetosome production strategies in bioreactors. It is this context that we developed a FCM based method for detecting chelatable iron in *M. gryphiswaldense* MSR-1 cells using phen green™ SK (PG-SK), whose fluorescence is quenched by metal ions including Fe^{2+} and Fe^{3+}. PG-SK has been previously used to study iron transporters (Große et al., 2006) and efflux systems in *E. coli* as well as applied to studies in human cell lines for iron, copper and silver uptake (Xu et al., 2012; Zhao et al., 2014).

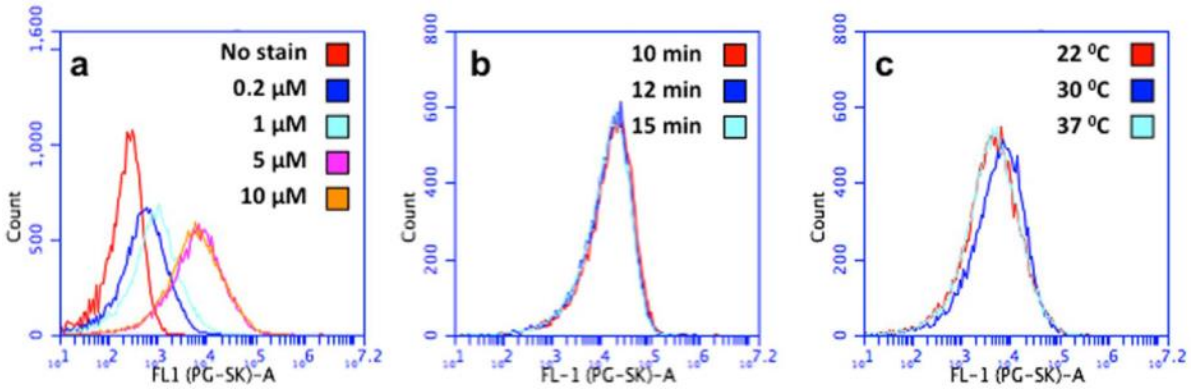

Figure 2.4. Analysis of intracellular iron by FCM. Fluorescence intensity histograms of non-magnetic MSR-1 cells growth in FSM-Fe^{-} after staining: (a) with various concentrations of PG-SK for 600 s at 30 °C (*N.B.* the 5 and 10 µM traces superimpose on each other); (b) for various times with 10 µM PG-SK at 30 °C (*N.B.* all traces superimpose on one another); and (c) at various temperatures using 10 µM PG-SK for 600 s.

Non-magnetic MSR-1 cells grown aerobically in FSM-Fe^{-} (without iron) were stained with PG-SK. The staining procedure was partially optimized with respect to staining time (600–900 s) and PG-SK concentration (0.2–10 µM) at three different temperatures (22, 27 and 30 °C). The highest fluorescence was observed at a PG-SK concentration of 5 µM after 10

minutes of incubation (Fig. 2.4a). Doubling the PG-SK concentration did not enhance the fluorescence intensity of stained MSR-1 cells further (Fig. 2.4a). Extending the time of staining incubation did not response a higher fluorescence, so longer staining times were not needed (Fig. 2.4b). Peak fluorescence intensity was similar at all staining temperatures employed (Fig. 2.4c).

2.3.6 Physiological changes of cells cultured with limited O_2 availability

The effect of O_2 limitation on growth and cellular magnetism of MSR-1 cells was investigated indirectly by varying the volume of headspace provided (i.e. 20%, 40%, 60%, and 80%) in tightly sealed 50 mL Falcon tubes. In all experiments the initial OD_{565} was 0.086 ± 0.004. After 48 h in culture, OD_{565} and C_{mag} values were recorded (Fig. 2.5a). Two clear and opposite trends were observed: biomass production paralleled the increase in headspace volume, and therefore O_2 availability, conversely, the magnetism of *M. gryphiswaldense* MSR-1 cells dropped dramatically from strongly magnetic (C_{mag} = 2) at 20% (v/v) headspace to very weakly magnetic (C_{mag} = 1.1 at 60% (v/v) headspace). These results are in agreement with findings from previous studies (Heyen and Schüler, 2003). Fig. 2.5b shows corresponding FCM analyses for relative quantification of intracellular iron and PHA content as a function of headspace volume. The highest intracellular PHA accumulation was observed in cells cultured in tubes with the lowest O_2 availability (i.e. lowest headspace volume of 20%). Increased PHA formation during O_2 limitation has previously been reported (Kessler and Witholt, 2001). Conversely, cells cultured at high O_2 concentrations (80% headspace volume) had the lowest PG-SK fluorescence among the tested conditions and thus the highest free iron concentration. Microarray data showed that iron transporter *feoB1* is upregulated aerobically (Wang et al., 2016), suggesting that iron transport into cells is highest aerobically.

Staining cells grown with different headspace volumes with PI and BOX (Fig. 2.6c) revealed that overall cell health was highest with 20% headspace and lowest with 80% headspace volume. PI was also used for analysis of physiology of MSR-1 cells from

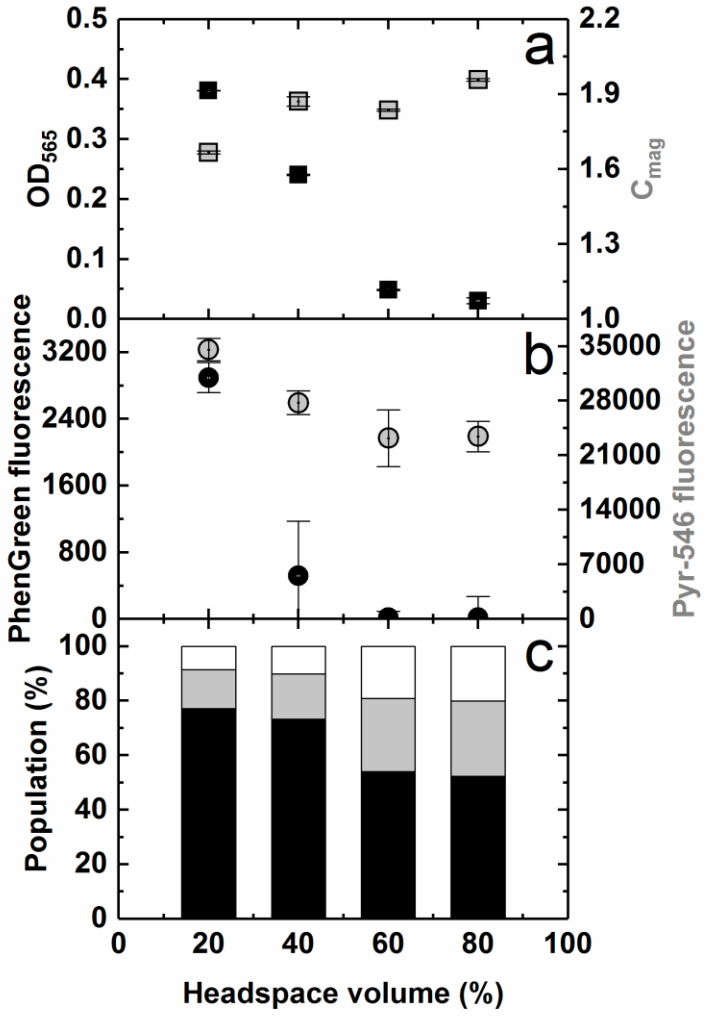

Figure 2.5. Effect of O_2 limitation on physiology. MSR-1 cultures were grown in tubes with different headspace volumes for 48 h. (a) OD_{565} (grey square) and cellular magnetism (C_{mag}; black square). Error bars are standard deviation. (b) Fluorescence of cells stained with PG-SK (black circle) and Pyr-546 (grey circle) as measured using FCM. Error bars are coefficient of variation. (c) Viability as determined using FCM and staining with PI and BOX; percentage of healthy (black bars), injured (pale grey bars) and dead (white bars) cells are shown. Experiments were performed in triplicate.

ACA agar plates; this indicated that 15–20% of cells on plates were dead (PI^+), whilst in a previous research by Wyre (2015), the dead *E. coli* remained below 10% (PI^+) throughout

the 16-week experiment. This highlights the difficulty in transferring MSR-1 cultures from single colonies to liquid cultures and emphasises the need to use a large amount of cells for setting up liquid cultures.

2.3.7 Physiological characterization of MSR-1 in shake flask experiments with free air exchange

To gain new insight into *M. gryphiswaldense* MSR-1 physiology during the shift from O_2-limited to aerobic conditions, we transferred cells grown under O_2-limited conditions to O_2-rich conditions with or without the supplementation of iron. Magnetic cells grown in FSM batch medium and using a pH-stat feeding strategy in an O_2-limited bioreactor were aseptically transferred to non-baffled shake flasks containing fresh media, either FSM or FSM without Fe (FSM-Fe^-), and grown in O_2 rich conditions (free air exchange) at 30°C on an orbital shaker (150 rpm). OD_{565} and C_{mag} were monitored immediately before (t = 0 h) and 24 or 48 h after transfer and intracellular free iron and cellular PHA content were measured and compared to the pre-transfer culture using FCM (Fig. 2.6). After O_2-limited growth in the bioreactor, and at the point of transfer to shake flasks (t = 0 h), MSR-1 cells were moderately magnetic (Cmag = 1.71). Strong Pyr-546 fluorescence (Fig. 2.6b, 0 h) and electron and fluorescence microscopy (Fig. 6.2) confirmed that cells contained large quantities of PHA. After transfer to aerobic conditions, cells grew better in the presence of iron (FSM) compared to the absence (FSM-Fe^-). After 24 h, C_{mag} rose slightly from 1.71 to 1.84 (although variation was high at 24 h), but then dropped to 1.46 at 48 h. Cultures grown in FSM had >3 fold decreased Pyr-546 fluorescence at 24 h and 48 h, indicating a decrease in PHA content, suggesting that growth utilised PHA as a substrate; FSC and SSC values also dropped (Fig. 2.6c), indicative of decreasing cell size and potentially corroborating loss of PHA granules. The impact of PHA utilisation on cell morphology has previously been reported in *C. necator* (Tian et al., 2005) and *Pseudomonas oleovorans* (Ruiz et al., 2001). In addition, in a parallel

experiment, TEM analysis and fluorescence microscopy with Pyr-546 stained cells allow comparison of PHA detection methods (Fig. 6.3).

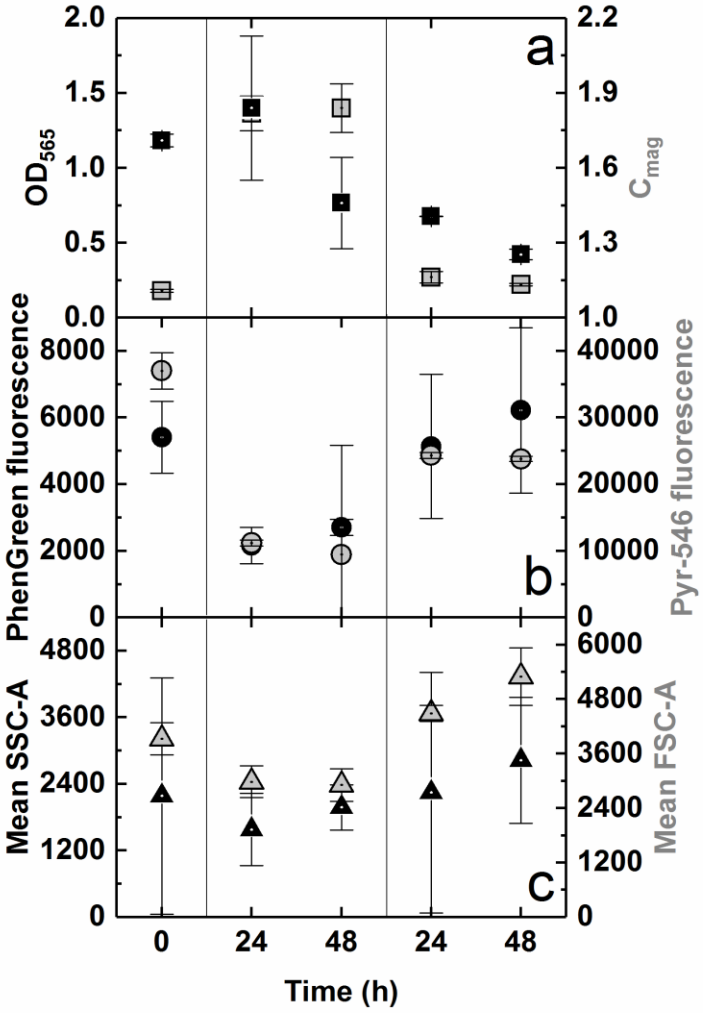

Figure 2.6. Physiology of magnetic cells during shift to aerobic conditions. MSR-1 cells grown under O2-limited conditions in a bioreactor were transferred to O2-sufficient conditions with either iron-containing (FSM) or iron-lacking (FSM-Fe−) media. (a) OD565 (grey squares) and Cmag value (black squares). Error bars are standard deviation; cells were taken from a single bioreactor into three replicate flasks for each condition. (b) Mean fluorescence intensity of cells stained with 0.5 µg·mL−1 pyrromethene-546 (Pyr546) (grey circles) or 5 µM phen green™ SK (PG-SK) (black circles). Error bars are covariance. (c) Forward scatter (FSC, grey triangles) and side scatter (SSC, black triangles) of cells as determined by FCM. Error bars are covariance. 25 000 events were analysed per sample by FCM.

After transfer of magnetic cells to culture medium lacking iron citrate (FSM-Fe^{-}), very little growth ensued (OD_{565} ~ 0.3; Fig. 2.6a), likely due to dilution of magnetosome content per cell during cell division (Uebe and Schüler, 2016). C_{mag} fell steadily (reaching 1.2 after 48 h; Fig. 2.6a). Pyr-546 fluorescence dropped to 65% of its pre-transfer value (Fig. 2.6b), reflecting low PHA utilisation, whereas FSC and SSC increased, indicating an increase in cell size and granularity (Fig. 2.6c).

PG-SK fluorescence dropped over time for cultures grown in FSM but not in the absence of iron; as expected, this reflects an increase in chelatable iron concentration in cells grown in the presence of iron, but not in the absence. Headspace volume experiments revealed an increase in intracellular iron concentration under more aerobic conditions in the presence of iron (Fig. 2.5). As with the regulation of intracellular iron concentrations in response to O_2, high extracellular iron concentrations were shown to increase the expression of the *feo* iron transporters (Wang et al., 2013).

FCM analysis of viability, intracellular chelatable iron and PHA, employing PI/BOX, PG-SK and Pyr-546 dyes respectively provides valuable insight on the effects of O_2 and iron levels on the growth, magnetosome and PHA production of MTBs. The data are rapidly obtained, does not require growth of MTBs on agar plates, and when used together with similarly fast measurements of optical density and C_{mag} can be useful in the design of growth strategies for production of magnetosome rich cells.

2.4 Conclusions

In this study, we have used the FCM tool to understand how *M. gryphiswaldense* cells grew slower under limited O_2 conditions, but the iron taken into the cells under this condition has been mineralised to form magnetosomes, whilst the iron taken under sufficient O_2 conditions

has not been solidified in the cells. PHA granules can only be consumed under sufficient O_2 conditions and PHA accumulation was very obvious under limited O_2 conditions. Thus, magnetosome production is only available in oxygen-limiting conditions.

In conclusion, we have demonstrated a series of fast analytical methods with FCM in the cultivation of *M. gryphiswaldense* both in liquid culture and on agar plates. We can employ FCM analyses to monitor cell size distribution, physiology, relative change to the intracellular contents of PHA and chelatable iron over the time of the cultivation with optimised, qualitative staining procedures. This study substantially simplifies monitoring strategies for the fermentation of *M. gryphiswaldense*.

CHAPTER 3

Development of a simple intensified fermentation strategy for growth of *Magnetospirillum gryphiswaldense* MSR-1: physiological responses to changing environmental conditions

Alfred Fernández-Castané, Hong Li, Owen R.T. Thomas, Tim W. Overton

A version of this manuscript has been published in

New Biotechnology in 2018

3.1 Introduction

Magnetotactic bacteria (MTB) are a phylogenetically diverse group of bacteria that are able to synthesize magnetosomes; sub-cellular nanoscale organelles that comprise chains of crystals of magnetite or greigite (depending upon the species of MTB), with each crystal coated in a biological phospholipid membrane containing membrane proteins (Arakaki et al., 2008; Heyen and Schüler, 2003). Magnetosomes represent an attractive alternative to existing commercially available chemically-synthesized magnetic nanoparticles, the synthesis of which usually requires: extreme temperature conditions (~320 °C in the "heat up" method); organic solvents; and subsequent complex in vitro surface modification steps for grafting biomolecules to the particle surface (Laurent et al., 2008). Chemical synthesis of magnetic nanoparticles with a narrow size range and at large scale is also difficult (Bakhshi et al., 2016; Galloway et al., 2013; Ling et al., 2015). Magnetosomes therefore have several advantageous properties: they are ferrimagnetic; have a narrow size distribution; are coated in organic material, preventing aggregation (Arakaki et al., 2008; Heyen and Schüler, 2003); and can be functionalized *in vivo* using genetic engineering tools, allowing one-step manufacture of functionalized particles (Borg et al., 2015).

Magnetosomes have been utilized in a wide range of biotechnological and healthcare applications, such as: contrast agents for magnetic resonance imaging; development of immunoassays; cell sorting and cancer therapy (Dasdag, 2014; Mathuriya, 2015; Wacker et al., 2007; Yoshino et al., 2008). However, availability of magnetosomes in sufficient quantities for these applications is problematic due to the low magnetosome yield of naturally occurring MTB species. *Magnetospirillum gryphiswaldense* is an MTB that has been subject of considerable research and can be cultured at higher cell densities than other MTB species; strain MSR-1 also generates up to 4% of its dry cell weight as magnetosomes

(Grünberg et al., 2004). Recent studies have optimized fermentations and employed genetic engineering approaches to improve magnetosome yields. Nevertheless, further improvement of MTB biomass and magnetosome yields remains a key objective in the field.

The optimised pH range for the cultivation of *M. gryphiswaldense* is 7.0-7.5 (Gorby et al., 1988; Heyen and Schüler, 2003; Lang and Schüler, 2008; Zhang et al., 2011), and the production of magnetosomes in *M. gryphiswaldense* occurs under oxygen-limited conditions; magnetite biomineralization is induced only below a threshold value of 20 mbar O_2 and optimum conditions for magnetosome formation were found at pO_2=0.25mbar (Heyen and Schüler, 2003). In order to achieve such conditions, pH-stat was employed because both the hydrogen consumption and carbon dioxide release occur in the fermentation to increase pH in the medium, and sophisticated control regimes employed gas blenders to supply mixtures of nitrogen and air containing 1% O_2 to maintain microaerobic conditions (Heyen and Schüler, 2003). This strategy requires supplying relatively high gas flow rates (0.1–3 L min^{-1}), leading to potential foaming in bioreactors and consequent use of antifoams, which may impair growth (Routledge, 2012). The complexity of gas blending and expense of very sensitive pO_2 probes renders scaleup difficult and unattractive. In other studies, the fermenter was supplied with air and the pO_2 was maintained between 0 and 1% by regulating airflow and agitation through cascade control (Zhang et al., 2011); alternatively, highly sensitive pO_2 probes were employed for accurate monitoring of absolute values of O_2 in the parts per billion range (Yang et al., 2013). However, using cascade control to maintain pO_2 set-point is likely to cause oscillations in dissolved oxygen concentration resulting in unstable pO_2 in the fermenter (Montague et al., 1989). Therefore, design of methods for growth of MTB in bioreactors must pay particular attention to the stable control of dissolved oxygen concentration. Efforts should also be made to employ control that can be scaled up for eventual industrial production of MTB.

In addition to oxygen concentration, denitrification pathways have been shown to be important for magnetosome formation (Li et al., 2014b, 2012; Y. Li et al., 2013). Magnetite biomineralization has been linked to dissimilatory nitrate reduction to dinitrogen gas, employing a periplasmic Nap nitrate reductase, cytochrome cd_1-dependent NirS nitrite reductase, a NorBC nitric oxide reductase and NosZ N_2O reductase (Li et al., 2012; Y. Li et al., 2013). The highest expression of denitrification- related genes coincided with conditions permitting maximum magnetite synthesis (Li et al., 2012). Both oxygen and nitrate are used as electron acceptors under microaerobic conditions, the former being reduced by a high affinity cbb_3-type terminal oxidase (Li et al., 2014b). A homologue of the oxygen-sensing transcription regulator FNR, MgFnr, regulates these processes and thus is important for magnetosome synthesis (Li et al., 2014b).

The physiology of *M. gryphiswaldense* has not been sufficiently studied in high-cell density cultures and so little is known about the parameters that limit biomass and magnetosome yields. For other organisms, yields are determined by factors such as media formulation, feeding strategy, bioreactor mixing and/or oxygen availability. Typically, for *M. gryphiswaldense*, shake flask cultures with limited control of process parameters yield biomass equivalent to an OD_{565} of 1–2 (Heyen and Schüler, 2003; Schüler and Baeuerlein, 1998) and therefore, findings from such shake flask cultures are not transferrable to bioreactor cultures, where biomass concentrations are around 10-fold higher. So far, *M. gryphiswaldense* MSR-1 has been the most studied strain in bioreactor experiments (Ali et al., 2017; Uebe and Schüler, 2016). Zhang and co-workers (Zhang et al., 2011) examined the increase of osmotic potential as a function of media composition. Yang et al., (2013) investigated physiological and metabolic stress parameters, such as reducing power and ATP content, to reveal conditions for magnetosome formation. More recently, transcriptome

analysis was used to compare magnetosome forming and non-forming conditions in *M. gryphiswaldense* in fermentation experiments (Wang et al., 2016). Under aerobic condition, genes expressed for nutrient metabolism, iron uptake, energy generation, such as *liv*, *feo*, and *cta* are up-regulated. Whilst under microaerobic condition, expression of *nap*, *nir*, *nor* and *nos* is up-regulated for dissimilarity denitrification pathway to provide additional energy required for magnetosome synthesis for enhancing motility and colonization abilities. Thus, a study of nitrate concentration in *M. gryphiswaldense* cultivation is very attractive.

In the previous chapter, new processes for analysis of MTB growth, physiology, magnetic iron biomineralisation and PHA content, were developed. In this chapter, the development of a simple pH-stat based fermentation, that affords growth of *M. gryphiswaldense* MSR-1 to high cell densities, is described. Flow cytometry methods developed in Chapter 2 combined with stress parameters (cell morphology, aspects of metabolism, and the accumulation of intracellular polyhydroxyalkanoate (PHA)) were employed to investigate the impact of different concentrations of lactate and nitrate on cell growth and magnetosome formation, with a view to developing better understanding of the physiology and metabolism of MTB. Such knowledge is essential for industrial production of magnetosome-based products in MTB, given that it underpins the commercial development of future magnetosome-related applications (Heyen and Schüler, 2003; Lohße et al., 2016; Zhang et al., 2011).

3.2 Materials and methods

3.2.1 Strains, growth media and culture conditions

Magnetospirillum gryphiswaldense MSR-1 was obtained from Deutsche Sammlung von Mikroorganismen und Zellkulturen GmbH (DSMZ, Germany) and used for all experiments. Unless indicated otherwise, all chemicals were purchased from Sigma-Aldrich (Poole, UK).

Cryostocks of *M. gryphiswaldense* in 5% DMSO were routinely grown in flask standard medium (FSM) comprising: 3.5 g L^{-1} potassium L-lactate; 100 µM iron citrate ($C_6H_5FeO_7$); 0.1 g L^{-1} KH_2PO_4; 0.15 g L^{-1} $MgSO_4 \cdot 7H_2O$; 2.38 g L^{-1} HEPES; 0.34 g L^{-1} $NaNO_3$; 0.1 g L^{-1} yeast extract; 3 g L^{-1} soy bean peptone; and 5 mL L^{-1} EDTA-chelated trace element solution (EDTA-TES (Widdel and Bak, 1992)) replacing $MnCl_2$ to $MnSO_4 \cdot H_2O$. EDTA-TES contained: 5.2 g L^{-1} EDTA disodium salt; 2.1 g L^{-1} $FeSO_4 \cdot 7H_2O$; 30 mg L^{-1} H_3BO_3; 85.4 mg L^{-1} $MnSO_4 \cdot H_2O$; 190 mg L^{-1} $CoCl_2$ g L^{-1}; 4 mg L^{-1} $NiCl_2 \cdot 6H_2O$; 2 mg L^{-1} $CuCl_2 \cdot 2H_2O$; 44 mg L^{-1} $ZnSO_4 \cdot 7H_2O$ and 36 mg L^{-1} $Na_2MoO_4 \cdot 2H_2O$. Pre-cultures used for bioreactor inoculation were grown in FSM without iron source. The pH of FSM was adjusted to 7.0 with NaOH (Heyen and Schüler, 2003). Cells were grown at 30°C in flat-bottomed flasks in an orbital shaker incubator operated at 150 rpm.

The batch medium for bioreactor experiments consisted of FSM without iron citrate and the feed solution contained: 50–200 g L^{-1} lactic acid; 3–25 g L^{-1} $NaNO_3$; 18 mL L^{-1} 25–28% $NH_3 \cdot H_2O$; 6 g L^{-1} yeast extract; 2.4 g L^{-1} $MgSO_4 \cdot 7H_2O$; 6 g L^{-1} $K_2HPO_4 \cdot 3H_2O$; 70 mL L^{-1} Mineral Elixir and 2 g L^{-1} $FeCl_3 \cdot 6H_2O$. The mineral elixir (pH 7) contained: 1.5 g L^{-1} nitrilotriacetic acid; 3 g L^{-1} $MgSO_4 \cdot 7H_2O$; 0.5 g L^{-1} $MnSO_4 \cdot 2H_2O$; 1 g L^{-1} NaCl; 0.1 g L^{-1} $FeSO_4 \cdot 7H_2O$; 0.18 g L^{-1} $CoSO_4 \cdot 7H_2O$; 0.1 g L^{-1} $CaCl_2 \cdot 2H_2O$; 0.18 g L^{-1} $ZnSO_4 \cdot 7H_2O$; 0.01 g L^{-1} $CuSO_4 \cdot 5H_2O$; 0.02 g L^{-1} $KAl(SO_4)_2 \cdot 12H_2O$; 0.01 g L^{-1} H_3BO_3; 0.01 g L^{-1} $Na_2MoO_4 \cdot 2H_2O$; 0.03 g L^{-1} $NiCl_2 \cdot 6H_2O$ and 0.3 mg L^{-1} $Na_2SeO_3 \cdot 5H_2O$.

3.2.2 Bioreactor set up

An Electrolab (Tewkesbury, UK) Fermac 310/60 5-L jar bioreactor equipped with 4 baffles and an agitator with 2 six-bladed Rushton turbines was used. Aeration was achieved by sparging air from below the lower impeller at a rate of 0 – 100 mL min^{-1}, through a reusable,

autoclavable 0.22-µm filter (Sartorius). Dissolved oxygen in the medium (pO_2) was measured online using a D150 Oxyprobe (Broadley James). Agitation was maintained at 100–500 rpm. pH was measured using an F-695 FermProbe (Broadley James) and was controlled at a set-point of 7 ± 0.05 with the automated addition of an acidic feeding solution. Off-gas passed through a condenser, autoclavable 0.22-µm filter (Sartorius, Goettingen, Germany) and HEPA filter (Millipore, Darmstadt, Germany). The temperature was maintained at 30 °C by a heating jacket and cold U-tube. Routine operational conditions were developed in this study and are detailed in the Results and Discussion section.

3.2.3 Flow cytometry

Table 3.1. Fluorescent dyes used in this study. With the exception of Pyr-546 (Photonic Solutions, Ohio, USA) the listed dyes were acquired from Fisher Scientific (Loughborough, Leics, UK). The cited working concentrations were adapted from previous work (Fernández-Castané et al., 2017) and/or optimised in this study.

Fluorescent dye	Excitation λmax, abs (nm)	Emission λmax, fl (nm)	Stock concentration	Solvent	Working concentration	Fluorescence channel
Bis-(1,3-dibutylbarbituric Acid) Trimethine Oxonol (BOX)	490	516	10 mg mL^{-1}	DMSO	100 ng mL^{-1}	FL1 (green)
Phen Green™ SK (PG-SK)	525	580	1 mM	DMSO	5 µM	FL1 (green)
Propidium iodide (PI)	533	617	200 µg mL^{-1}	H_2O	100 ng mL^{-1}	FL3 (red)
Pyrromethene-546 (Pyr-546)	493	519	0.1 mg mL^{-1}	DMSO	0.5 µg mL^{-1}	FL1 (green)

Bacteria were analyzed using a BD Accuri C6 flow cytometer (BD Biosciences, UK). Samples were taken from the bioreactor, resuspended in phosphate-buffered saline (PBS) and stained with dyes listed in Table 3.1. Samples were excited with a 488 nm and forward scatter (FSC) and side scatter (SSC) and fluorescence data collected (Table 3.1). Dyes were

used for fluorescence assays and with the exception of Pyr546 (Photonic solutions, Ohio, USA) were purchased from Thermo Fisher Scientific (UK).

3.2.4 Analytical methods

Culture optical densities at 565 nm (OD_{565}) were measured using a spectrophotometer (Evolution 300 UV–vis, Thermo Scientific, UK). Data were collected using VISIONpro software. Magnetic response (C_{mag}) of cells was measured immediately after OD_{565} using a magnetic measurement system built into the spectrophotometer, based on devices described in the literature (Lefèvre et al., 2009; Zhao et al., 2007). Briefly, 2 pairs of Helmholtz coils were arranged around the cuvette holder, one pair perpendicular to the light beam and the other pair in line with the light beam. Each pair of coils was energized in turn (producing a magnetic flux density of 1.9mT at the centre of the cuvette) and the optical density (OD_{565}) measured in each state. Magnetic cells align with the magnetic field and thus are either oriented in line with the light beam, or perpendicular to it, thereby changing the optical density measurement. Non-magnetic cells do not move when the magnetic field is changed, so their optical density is identical in both states. The C_{mag} is calculated by dividing the OD_{565} value measured when cells are aligned parallel to the light beam by that obtained when cells are aligned perpendicular to the light beam. For dry cell weight (DCW) determination, 1 mL samples, prepared in triplicate, were centrifuged and washed three times with MilliQ water, followed by overnight incubation at 105 °C.

Fluorescence microscopy (Zeiss Axiolab) was used to observe stained cells with fluorescent probes. Images were acquired using an AxioCam ICm1 camera and processed using ZEN Lite 2012 software in auto exposure mode. Samples were excited using an ultraviolet light source (Zeiss VHW 50f-2b) and fluorescence was detected using a 520 L P filter.

3.2.4.1 Nitrate and nitrite assays

Nitrate concentration was determined using the Szechrome NAS reagent system (Polysciences inc., USA) according to manufacturer's instructions. Briefly, a working reagent was prepared comprising 5 g L^{-1} Szechrome NAS reagent dissolved in a 1:1 mixture of 85–86% (v/v) H_3PO_4 and 95–97% H_2SO_4. Samples were diluted 40-fold before analysis, prepared in duplicate, and 50 µL portions were pipetted into 1 cm light path cuvettes, before adding 950 µL of working reagent and incubating for 1 h. Absorbance was read at 570 nm in a spectrophotometer (Evolution 300, Thermo Scientific, USA).

Nitrite concentration was determined using the Greiss reagent kit system (Promega, USA) according to manufacturer's instructions. Samples were diluted 20-fold for analysis, prepared in duplicate, and absorbance was read at 560 nm in a plate reader.

3.2.4.2 Lactic acid assay

Extracellular L-lactic acid concentration was measured using an Llactic acid kit (Megazyme, Ireland) according to manufacturer's instructions. Samples were diluted 40-fold for analysis in duplicate, and reactions were prepared at total volumes of 1 mL in 1 cm light path cuvettes. Absorbance was measured at 340 nm before and after an incubation time of 10 min.

3.2.4.3 Iron concentration

Flame atomic absorption spectroscopy was performed as an offline analysis to study the intracellular and extracellular iron concentrations within the bioreactor. Iron was determined

at 248.3 nm using a single element iron hollow cathode lamp (SMI-LabHut Ltd.) operated at a current of 30 mA with an acetylene/air flame (0.7 L min^{-1} acetylene and 4.0 L min^{-1} air) in a Perkin Elmer AAnalyst 300 Atomic Absorption Spectrometer (USA). Sample preparation was done in triplicates as described elsewhere (Heyen and Schüler, 2003). Briefly, 500 µL nitric acid (70% v/v) was used to solubilize the iron in the form of magnetite pellets and incubated at 98 °C for 2 h with shaking at 300 rpm, whereas 10 µL were employed for supernatant samples.

3.2.4.4 Transmission electron microscopy

Cell pellets were centrifuged at 14,000 rpm for 3 min, resuspended in 1 mL of 2.5% (v/v) glutaraldehyde in 0.1 M potassium phosphate solution (pH 7.2) and incubated for 1 h. A series of washing steps with increasing alcohol concentration (50–100% v/v) followed. Sedimented cells from the last dehydration step were embedded in resin by infiltration of the pellet with a solution containing 50% (v/v) Mollenhauer (Mollenhauer, 1964) resin in propylene oxide (Agar Scientific) on a rotator (Type N, TAAB) operated at 4 rpm for 12 h in a fume cupboard, followed by curing in undiluted Mollenhauer resin at 60 °C for another 48 h. Thin sections (120 nm) were cut from the resin block using diamond knives on a Reichert-Jung UltraCut Ultramicrotome. The cut sections were examined using a JEOL 1200EX TEM electron microscope operated at 80 kV, in the transmission mode, with the beam current at 60 µA, and TEM images were collected.

3.3 Results and discussions

This study investigated the production of magnetosomes in *M. gryphiswaldense* MSR-1 in bioreactors upon variation of environmental conditions and feed composition (lactic acid and sodium nitrate concentration). Magnetosome biomineralization has been shown to occur

under microaerobic conditions (Heyen and Schüler, 2003) and previous studies performed in bioreactors demonstrated that optimal process conditions to obtain high biomass and magnetosome yields were achieved by balancing O_2 and nutrient supply (Heyen and Schüler, 2003; Zhang et al., 2011). Here, a relatively simple intensified fermentation strategy was developed using flow cytometry (FCM) to study changes in cell physiology and morphology, PHA accumulation, and intracellular chelatable iron concentration. First, scoping fermentations were carried out to define a routine fed-batch pH-stat growth strategy. The pH-stat strategy was first used by Zhang et al. (Zhang et al., 2011) for *M. gryphiswaldense* growth; an acidic feeding solution containing nutrients including lactic acid as a carbon and energy source was supplied into the medium to maintain the pH set-point of 7. Next, the effect of the lactic acid concentration in the feed solution on bacterial growth and physiology was evaluated. Finally, the effect of the concentration of sodium nitrate in the feed solution was evaluated. Taken together, a development pathway to intensified bioreactor cultures of *M. gryphiswaldense* MSR-1 is provided that could be scaled up in future work.

3.3.1 A simple fermentation strategy to grow magnetosome-producing *M. gryphiswaldense* MSR-1

Preliminary experiments were used to determine the routine operational conditions of the pH-stat strategy. In these experiments, cellular magnetosome content was determined by measuring intracellular iron content using atomic absorption spectroscopy (AAS). In previous works, magnetosome production has been measured employing methods to determine dry weight of magnetosomes (Zhang et al., 2011) using the protocol described by Xiang et al., (2007), or AAS of purified magnetosomes. Alternatively, magnetosome yields have been calculated by measuring iron in media and subsequent mass balances (Sun et al., 2008), or by means of inductively coupled plasma optical emission spectroscopy (Yang et al., 2013).

Therefore, such variation in analytical methodologies to determine magnetosome production must be considered when comparing studies.

First, the effect of air supply to the culture (0 – 100 mL min^{-1}) and different stirring rates in the bioreactor (100–500 rpm) were evaluated. Setting air flow rates above 10 mL min^{-1} and stirring above 300 rpm at the beginning of the fermentation prevented the pO_2 from dropping to 0%, and thus the low oxygen tension required for magnetosome formation could not be achieved. The position of the two impellers in the bioreactor was optimized to minimize foaming; the upper impeller was placed 2 cm below the liquid/air interface with the lower impeller placed 3 cm below the upper impeller. Together with the low aeration rates, this suppressed foaming and therefore prevented the requirement for antifoam, which can inhibit growth (Routledge, 2012).

Supply of oxygen and iron was investigated in two sets of two-stage fermentations, with the aim of temporally separating biomass and magnetosome formation, as is common practice in fermentations generating recombinant proteins, where growth and protein production are temporally separated (Overton, 2014). First, *M. gryphiswaldense* MSR-1 was grown aerobically (150–400 rpm stirring, 10 mL min^{-1} airflow, control of pO_2 to>10% by varying stirrer speed, pH-stat feeding mode) in FSM medium containing a total iron concentration of 7.7 mg L^{-1} (5.6 mg L^{-1} supplied as ferric citrate ($C_6H_5FeO_7$) and 2.1 mg L^{-1} supplied as $FeSO_4$ in the EDTA trace element solution) to an OD_{565} of around 6, which took 60 h. The bioreactor was then purged continuously with nitrogen gas (0.4 – 0.6 L min^{-1}) in order to rapidly decrease the pO_2 to ‘zero’, aiming to reach conditions suitable for magnetosome production. This switch from aerobic to anaerobic conditions increased the iron content of the cells (determined using AAS) from 2 to 8.7 mg of iron per gram DCW, but cell growth

ceased under anaerobic conditions. Previous studies carried out by Heyen and Schüler, (2003) growing MSR-1 under aerobic conditions in medium containing 100 μM ferric citrate determined basal levels of intracellular iron up to 10.8 mg g^{-1} of DCW; these cells were classed as only weakly magnetic, probably due to oxygen limitation caused by high biomass concentrations. Therefore, our basal cellular iron contents are comparable to previous reports (Heyen and Schüler, 2003), indicating either formation of small quantities of magnetosomes, or more likely, non-magnetosome intracellular iron that could be stored by bacterioferritin under aerobic conditions (Wang et al., 2016).

Next, MSR-1 was grown under oxygen-limited conditions ($pO_2 \leq 0.4\%$) using pH-stat mode for 54 h to an OD_{565} of around 4.3 in FSM without the addition of ferric citrate (this medium contained 2.1 mg of Fe^{2+} L^{-1}, supplied as EDTA-TES). Then, a pulse of ferric chloride was added to the feed solution to bring the final concentration of Fe^{3+} to 414 mg L^{-1}; the feed also contained 1.4 mg of Fe^{2+} L^{-1}, supplied as Mineral Elixir). This caused a dramatic cessation of cell growth after 3 h; the final biomass concentration achieved was OD_{565} ~6.4, and cellular iron concentration increased from 3.1 to 6.1 mg g^{-1} DCW after a total fermentation time of 71 h. These two scoping studies demonstrated that rapid changes in oxygen concentration or iron concentration were detrimental to overall process performance, thereby directing design of culture methods without such changes.

Following these initial scoping experiments, routine fermentation conditions were established as follows. Stirring rate was maintained at 250 rpm throughout. Bioreactor experiments were started without any air supply so that the drop in pO_2 occurred within ca. 24 h of fermentation and reached 'zero' at an OD_{565} of 1 – 1.5. Air supply was started ~2 h after reaching a pO_2 of 0% at a flow rate of 3 mL min^{-1}; airflow rate was subsequently increased by 1 mL min^{-1} for

every 1 unit increase in OD_{565}. This aeration strategy allowed cultures to start growing aerobically, then gradually adapt to the decreasing pO_2, finally resulting in oxygen-limited conditions suitable for magnetosome formation. All the other fermentation conditions are described in the Materials and Methods section. Fig. 6.4 shows an example of changes in OD_{565}, stirrer speed, pH, pO_2 and airflow over a representative pH-stat fermentation.

Our growth strategy employs a simple set up approach, minimizes the use of complex control parameters, and eliminates the need for gas blending. This method permitted biomass concentrations comparable to previously reported work to be attained (Yang et al., 2013), and to the best of our knowledge only one academic research group (Yang et al., 2013; Zhang et al., 2011) has recorded significantly higher MTB biomass yields, i.e. OD_{565} values of 30.4 and 43 in 7.5 L and 42 L bioreactors, respectively.

3.3.2 Optimisation of lactic acid supply in the feed solution

The use of lactate or lactic acid as a carbon source has been widely studied in *M. gryphiswaldense* bioreactor experiments. Heyen and Schüler, (2003) used flask standard medium (FSM) and large scale medium (LSM) containing 27mM potassium lactate as a carbon source in batch experiments. 15mM sodium lactate was used in optimized fermentation medium (OFM) by Sun and co-workers (Sun et al., 2008) and Li et al., (2012) in batch and fed-batch experiments, respectively. Zhang and co-workers (Zhang et al., 2011) sought to reduce accumulation of Na^+ and Cl^- ions in the media, which were thought to inhibit growth. They used sodium lactate in the batch medium and three formulations of feed solution for pH-stat experiments with different concentrations of lactic acid or sodium lactate as carbon source, and NH_4Cl or ammonium hydroxide as nitrogen source. They showed that the osmotic potential was maintained throughout the fermentation (100 mmol kg^{-1}) using

Feed C, which contained 100 g L^{-1} lactic acid and 18 mL L^{-1} ammonium hydroxide, allowing achievement of the highest biomass concentration of *M. gryphiswaldense* MSR-1 to date (equivalent to OD_{565} = 30.4 in a 7.5 L bioreactor).

The Feed C of Zhang et al., (2011) was used as a starting point to assess the effect of lactic acid concentration in the feed. Three oxygen-limited fermentations were performed with 50, 100 or 200 g L^{-1} lactic acid in the feed. The pHs of the feeds were 3.65, 3.05 and 2.65, respectively. As a consequence, the most acidic feed required less volume to maintain the pH set point (7.0 ± 0.05) during pH-stat growth. An aerobic fermentation was also carried out with 100 g L^{-1} lactic acid feed. Fig. 6.5 shows the relationship between the quantity of feed solution added to bioreactors in pH-stat mode and the biomass concentration in g DCW·L^{-1}; a linear regression was fitted to data where cells were actively growing, with R^2 values of 0.94–0.99. The calculated feeding rates were respectively 131.4, 17.8 and 1.63 mL[1] of feed per g DCW L^{-1} for the 50, 100 and 200 g L^{-1} lactic acid oxygen-limited experiments. The aerobic experiment resulted in a feeding rate of 2.92 mL of feed for every g DCW per litre. The lactic acid concentration decreased over the oxygen-limited fermentations employing 100 and 200 g L^{-1} lactic acid, whereas it rose during the 50 g L^{-1} lactic acid feed fermentation. This observation is relevant when considering the required volume of feeding solution, that in turn affects the production costs in an industrial setting. Significantly more 100 g L^{-1} lactic acid feed was required for oxygen-limited growth than needed for aerobic growth. It should be noted that feed requirements are a function of pH increases in the fermenter and do not correlate directly to lactic acid demand as a carbon source; this

[1] The mass of lactic acid added into the bioreactors were 6.57, 1.78, and 0.33 g for the feed of 50, 100, and 200 g L^{-1}, respectively.

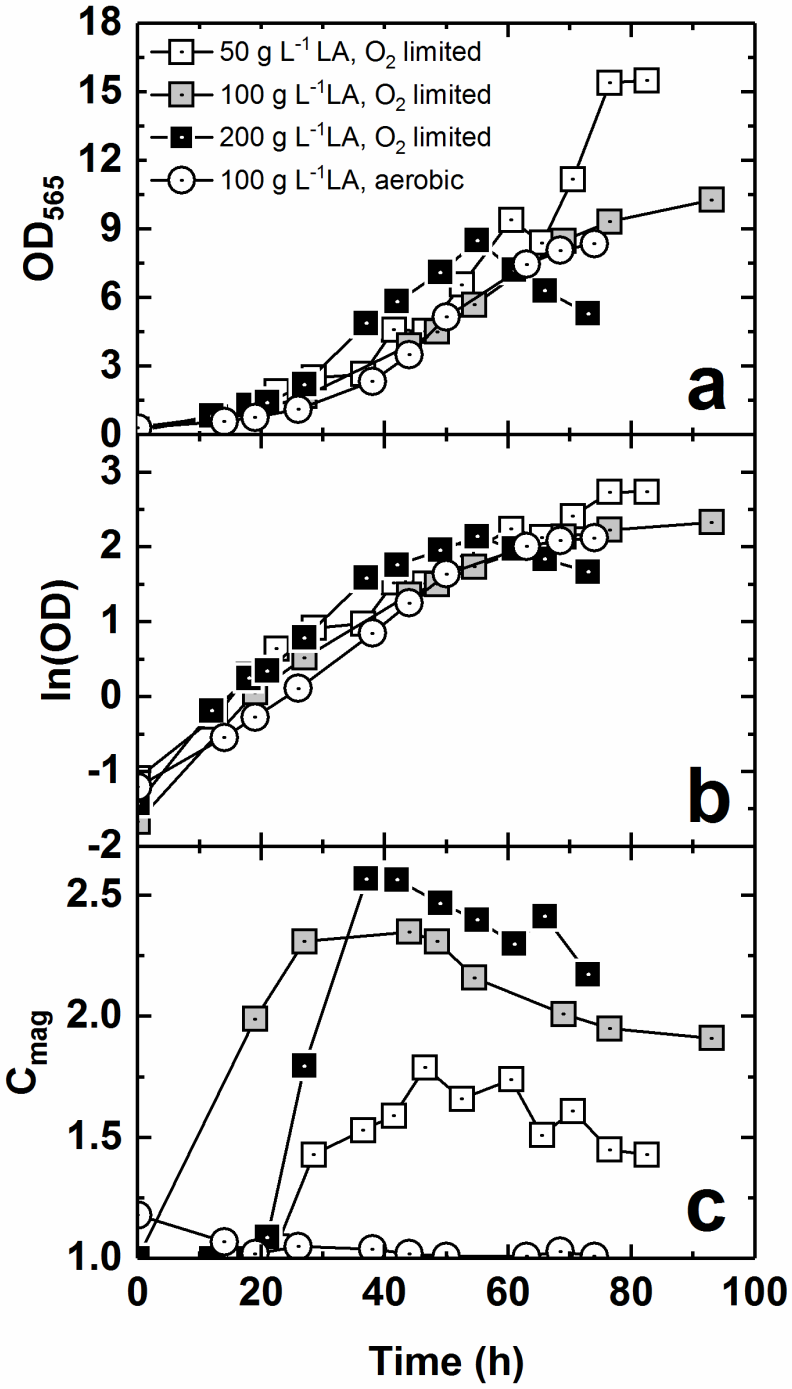

Fig. 3.1. Comparison of oxygen-limited and aerobic fermentations conducted with different feed lactic acid concentrations. Plots show (a) OD_{565}, (b) growth rates ln (OD), and (c) cellular magnetic response, C_{mag} versus time.

reinforces the need to optimize lactic acid concentration in the feed, to balance pH maintenance, minimize cost and prevent accumulation of excess carbon source or other nutrients. Growth curves (Fig. 3.1a) show that OD_{565} was highest in the culture grown with

50 g L^{-1} lactic acid feed. Specific growth rates were calculated (Table 3.2) and it was observed that maximum specific growth rate (μ_{max}) occurred at the early stage of the fermentation and within the first 24 h of culture in all microaerobic experiments, whereas growth rate remained roughly constant over the exponential phase in the aerobic experiment (Fig. 3.1b).

Cellular magnetism (C_{mag}) was also measured to determine the response to cells to magnetic fields. Specific growth rates (Table 3.2) were generally higher for the period before (μ_b) than the period after (μ_a) the point at which the highest C_{mag} value was reached in oxygen-limited cultures (Fig. 3.1c). When comparing the aerobic and oxygen-limited fermentations carried out with the same feed composition, the latter showed a higher growth rate at the beginning and a quick decrease after 40 h, whilst the aerobic fermentation showed a roughly constant growth rate until 50 h of cultivation (Fig. 3.1b). Our results showed lower μ values than reported previously for use of pH-stat mode; this may reflect differences in growth and operational strategies to maintain oxygen-limited conditions and/or media composition.

Table 3.2 Comparison of bioprocess parameters for culture with varying feed lactic acid concentration.

Lactic acid concentration in feed (g L^{-1})	μ_{max} (h^{-1})	μ^b (h^{-1})	μ^a (h^{-1})	$Y_{X/S}{}^b$	$Y_{X/S}{}^a$
50	0.12	0.056	0.051	0.15	0.26
100	0.09	0.069	0.02	0.23	0.23
200	0.1	0.07	-0.003	0.23	0.02
100 (Aerobic)	0.07	0.058*		0.14*	

Key: μ^b and μ^a correspond to the growth rate before and after reaching maximum C_{mag}, and $Y_{X/S}{}^b$ and $Y_{X/S}{}^b$ are the corresponding yield coefficients; *values correspond to the exponential phase.

Our total fermentation time varied between 70–94 h as opposed to 44 h reported by Zhang and co-workers (Zhang et al., 2011) to reach an OD_{565} of 30.4; our maximum OD_{565} value was 15.5. However, maximum specific growth rates from our work (0.09 – 0.12 h^{-1}) are only slightly lower than μ values obtained from oxystat experiments performed in previous studies with *M. gryphiswaldense*, which were ≈0.13 h^{-1} under microaerobic conditions, where OD_{565} values of<1.5 were reached (Heyen and Schüler, 2003).

Table 3.3. Maximum biomass (OD_{565}), iron concentration and C_{mag} measurements for fermentations presented in Fig. 3.1.

Maximum value	Lactic acid concentration (g L^{-1})		
	50	100	200
OD_{565}	15.5	10.3	8.5
Iron concentration (mg L^{-1})	53.5±1.2	19.4±0.2	56.8±0.3
Iron/DCW (mg g^{-1})	14.8±0.7	12.2±0.3	33.1±1.0
C_{mag}	1.79	2.35	2.56

For iron concentration values, mean values from 3 measurements are stated ± standard deviation.

Biomass to substrate yields for cultures were calculated both before ($Y_{x/s}{}^{b}$) and after ($Y_{x/s}{}^{a}$) reaching their maximum C_{mag} values (Table 3.2). Comparison of $Y_{x/s}{}^{b}$ within the oxygen-limited cultures revealed that the 50 g L^{-1} lactic acid feed yielded less biomass per mass of supplied lactic acid than the 100 or 200 g L^{-1} feeds. $Y_{x/s}{}^{a}$ values reflect the fact that the biomass increased after the oxygen-limited 50 and 100 g L^{-1} fermentations reached maximum C_{mag}. The 200 g L^{-1} experiment did not increase in biomass after reaching maximum C_{mag}.

Maximum biomass and magnetosome productivity for those fermentations are compared in the oxygen-limited experiments in Table 3.3. The amount of lactic acid in the feed solution inversely correlated to final biomass. The highest volumetric and specific magnetosome

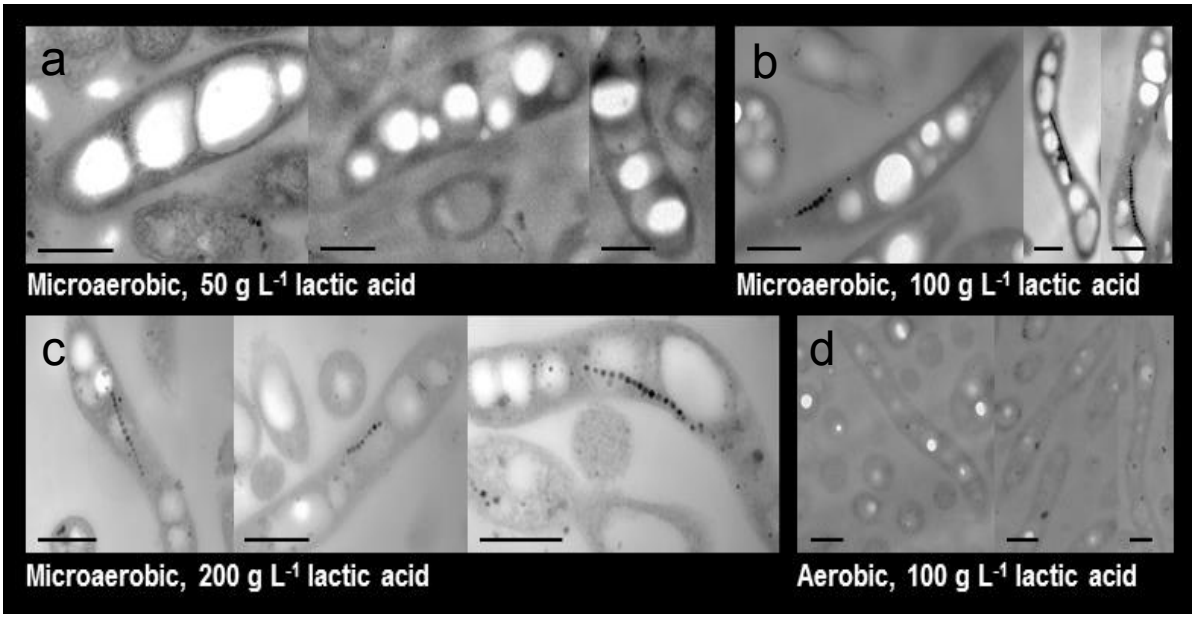

Figure 3.2. Transmission electron micrographs of bacteria from oxygen-limited and aerobic fermentations conducted with different feed lactic acid concentrations. The length of each scale bar is 0.5 µm.

production, as determined by AAS, was achieved in the 200 g L^{-1} feed experiment, yielding 56.8 mg iron L^{-1} and 33.1 mg iron g^{-1} DCW, respectively. The highest C_{mag} (2.56) was observed in the 200 g L^{-1} feed experiment and the lowest with 50 g L^{-1} feed, whilst the lowest iron amount *in vivo* was observed in the 100 g L^{-1} feed experiment. This illustrated that cellular iron content and C_{mag} did not correlate perfectly well with one another. TEM images (Fig. 3.2a–d) showed that cells harvested from the 50 g L^{-1} feed culture did not contain magnetosomes, or had short magnetosome chains, whereas longer chains were found in bacteria from the 100 g L^{-1} and 200 g L^{-1} feed fermentations. Additionally, as C_{mag} depends on changes in light scattering (as detailed in the Materials and Methods section), other parameters aside from the content of magnetosome chains, e.g. cell shape/morphology, likely influence the C_{mag} value. Thus, the measurement of iron concentration should be solid iron, but not the total intracellular iron. This can be achieved by measuring the pellet samples after cell disruption operations, which we did in Chapter 4.

Maximum C_{mag} values were achieved at an OD_{565} of 5–8 depending on the experiment (Fig. 3.1c), but in all cases did not correspond to the point of maximum biomass concentration. This observation can be compared with previous studies where highest C_{mag} values were achieved at OD_{565} values of 2–5 in pH-stat cultures (Wang et al., 2016; Yang et al., 2013). Our results demonstrate the importance of not only the chemical nature of the carbon source, which has been previously described by other research groups, but also its concentration within the feed. While the 50 g lactic acid L^{-1} feed culture resulted in the highest biomass achieved using our growth strategy, the highest cellular iron content and C_{mag} were obtained using the highest lactic acid feed concentration of 200 g L^{-1}. Therefore, a compromise between biomass and magnetosome production must be considered in industrial settings.

3.3.3 Application of flow cytometry to monitor physiology

Flow cytometry (FCM) was recently used by our group as a rapid, single-cell technique to study the physiology of MTB during growth in flasks (Fernández-Castané et al., 2017). In the present study, we have applied FCM to analyse and optimize fermentations. Propidium Iodide (PI) is a red DNA dye widely used to detect dead bacteria; the intact membrane of viable bacteria excludes PI, therefore live cells are PI^- and dead cells are PI^+. $DiBAC_4(3)$ (Bis-(1,3-Dibutylbarbituric Acid) Trimethine Oxonol), commonly referred to as Bis-oxonol (BOX), is a green lipophilic dye that enters the cell only if the membrane is depolarized (Nebe-von-Caron et al., 2000) allowing determination of cellular respiration. Co-staining with PI and BOX therefore permits detection of three physiological states: 'healthy' (PI^- BOX^-); 'injured' (PI^- BOX^+; the cells are intact but are depolarized); and 'dead' (PI^+ BOX^+).

Co-staining with PI and BOX showed similar results in experiments with different feed lactic acid concentrations (Fig. 3.3). It was observed that between 85–90% of cells were healthy at the start of fermentation. This relatively low proportion of healthy cells may reflect the use of a late stationary phase inoculum as is observed with *E. coli* (TW Overton, unpublished data). The size of the healthy population increased over time, reaching nearly 99% after ~27 h, roughly coinciding with the increase in C_{mag} from 1 to 2.5 between 20 h and 35 h.

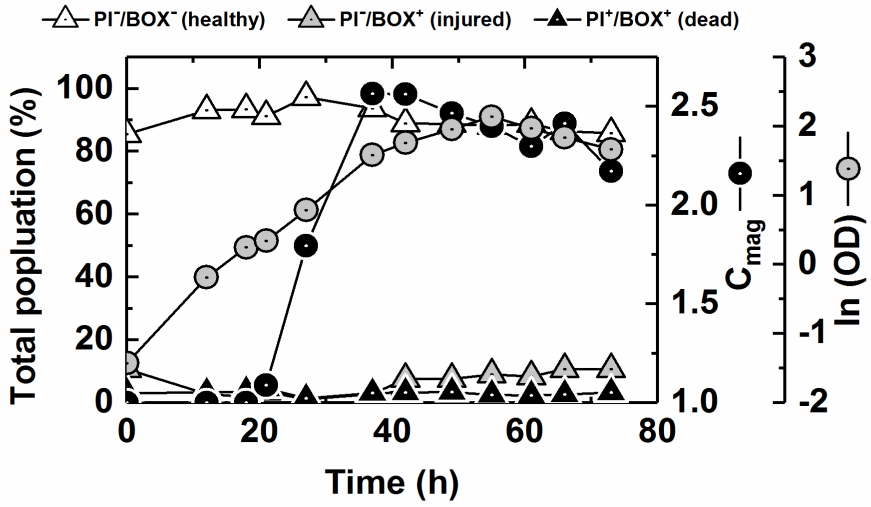

Fig. 3.3. Assessment of bacterial physiology using FCM. Bacteria from an oxygenlimited pH-stat culture with 200 g L^{-1} lactic acid and 6 g L^{-1} sodium nitrate in the feed were stained with PI and B and analysed by FCM. The percentages of cells within three differently stained populations, i.e. PI^-/BOX^- ('healthy'), PI^-/BOX^+ ('injured') and PI^+/BOX^+ ('dead'), are plotted.

Subsequently the healthy population dropped to 80 – 85% corresponding to the period (35–72 h), where growth slowed and C_{mag} fell to<2.25. The proportion of injured cells (PI^- BOX^+) was highest when the healthy population was lowest, whereas the proportion of dead cells (PI^+ BOX^+) remained low (1–5%) throughout the fermentation.

3.3.4 Application of flow cytometry to monitor cell size, shape and PHA accumulation

Cell size and optical complexity were monitored by FCM by means of light scattering. Light scattered by cells is measured by two detectors: forward scatter (FSC), measured in line

with the illuminating laser beam, broadly correlates with cell size; side scatter (SSC), measured orthogonally to the laser beam, indicates the granularity or optical complexity of cells (Day et al., 2002). Comparison of FSC and SSC data for cultures with different lactic acid feed concentrations revealed that the largest increases in both FSC and SSC were noted for cultures fed with lactic acid at 50 g L^{-1} and the smallest were observed when a feed concentration 200 g L^{-1} was employed (Fig. 3.4a–c). TEM micrographs confirm differences in cell size and granularity; cells fed with 50 g L^{-1} of lactic acid (Fig. 3.2a) exhibited a rounder shape with large white inclusions, resembling PHA aggregates as reported by Bresan, Liu and their co-workers, respectively (Bresan et al., 2016; Liu et al., 2008) whereas cells fed with 100 g L^{-1} (Fig. 3.2b) and 200 g L^{-1} lactic acid (Fig. 3.2c) were more elongated.

Given that TEM (Fig. 3.2) revealed that cells fed with different concentrations of lactic acid contained differing amounts of PHA granules, FCM was used to determine cellular PHA accumulation by staining of the cells with the green lipophilic dye Pyrromethene-546 (Pyr546; Fig. 3.4d) (Bañuelos Prieto et al., 2004; Vizcaino-Caston et al., 2016). As with the FSC and SSC data (Fig. 3.4b-c), Pyr546 fluorescence (and thus PHA concentration per cell) was highest for cells fed with 50 g L^{-1} lactic acid and lowest for 200 g L^{-1} lactic acid feed. The correlation between SSC and Pyr546 fluorescence is plotted in Fig. 3.4e. Fig. 3.4d also shows fluorescence micrographs of cells taken from the end of each fermentation stained with Pyr546, corroborating FCM and TEM data. The increased quantity of PHA in cells grown with 50 g L^{-1} lactic acid would also explain why the $Y_{x/s}$ values for this culture were lower than those recorded with the higher lactic acid feed concentrations (Table 3.1). Histograms of Pyr546 fluorescence (shown in Fig. 6.6) demonstrate, that for cultures fed with 50 and 100 g L^{-1} lactic acid, a narrow normal distribution was found, meaning that all cells within the culture exhibited similar levels of PHA accumulation. In contrast, cells fed

with 200 g L^{-1} lactic acid displayed bimodal distribution at two time-points (19–22 h and 74–96 h), indicating two populations within the culture, one PHA-rich, the other comparatively PHA-poor.

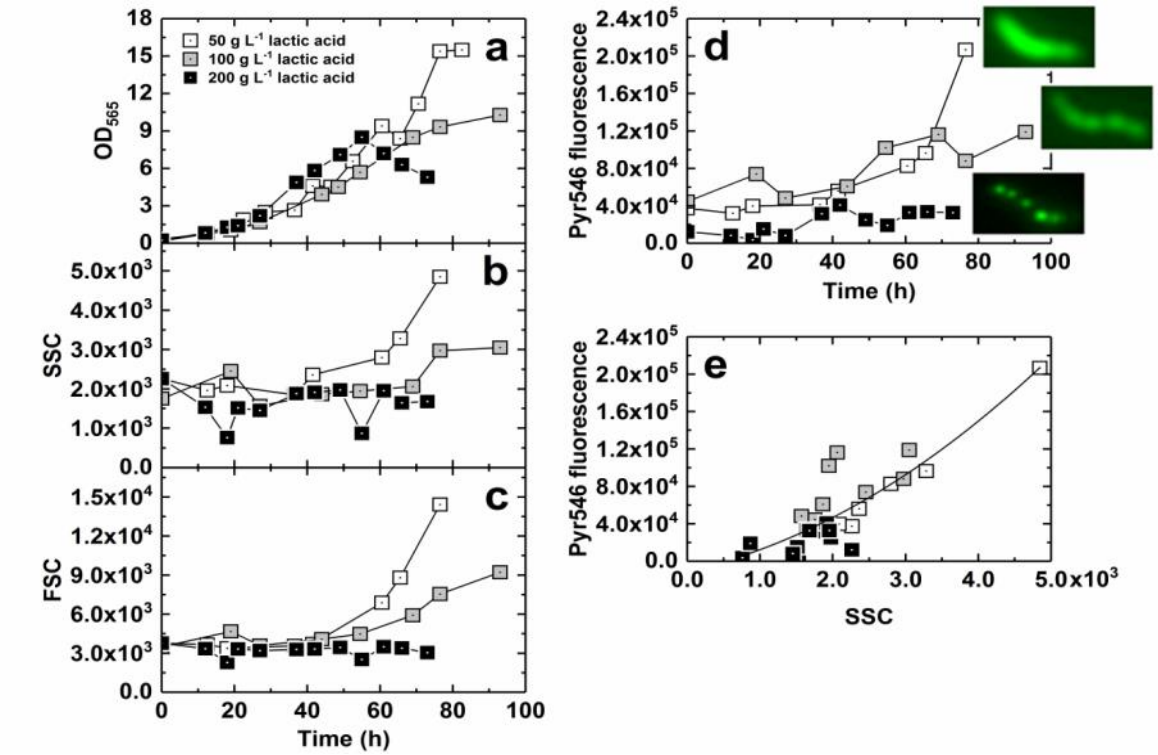

Figure 3.4. Flow cytometry analysis of scatter and PHA content of cells grown with different feed lactic acid concentrations. Samples taken from oxygen-limited pHstat fermentations with different feed lactic acid concentrations were analyzed by measurement of OD_{565} and FCM. Twenty-five thousand data points were collected for each sample and mean values are represented. Panels show OD_{565} (a), forward scatter, FSC (b), side scatter, SSC (c), and fluorescence post-staining with Pyr546 (d) plotted against time; and Pyr546 fluorescence vs. SSC (e). The insets in (d) show fluorescence micrographs of cells at the end of each fermentation after staining with Pyr546.

The formation of PHA aggregates in MTB has been previously reported. PHA is generated when there is an excess of carbon source compared to another nutrient, frequently nitrogen. As the 50 g L^{-1} lactic acid feed experiment had the highest quantity of carbon source added to the bioreactor, and lactic acid was seen to accumulate in the medium, it is logical that highest PHA accumulation occurred under these conditions. In addition, excess reducing

power in MTB is consumed through PHA formation and hydrogen release (Ban et al., 2010); this phenomenon has been observed in several studies under different culture conditions (Schultheiss et al., 2005). In this work, we demonstrate for the first time the formation of PHA in *M. gryphiswaldense* high-cell density bioreactor cultures. Our results are in agreement with previously reported studies regarding the energy competition between PHA and magnetosome formation (Raschdorf et al., 2014), the 200 g L^{-1} lactic acid feed experiment resulting in the highest magnetosome production (33.1 mg iron g^{-1} DCW) and lowest PHA formation.

3.3.5 Nitrate enhances cell growth

Previous studies reported that magnetosome formation and denitrification occur simultaneously under oxygen-limited conditions (Li et al., 2014b). The nitrate concentration has been optimized for media used in shake-flask experiments, but to the best of our knowledge no research has focused on the optimal supply of nitrate in relatively high cell density *M. gryphiswaldense* bioreactor cultures. Hence, we optimized the supply of sodium nitrate into the feed solution using 100 g L^{-1} lactic acid as a carbon source in pH-stat cultures.

Fig. 3.5a–d show plots of OD_{565}, pO_2, medium nitrate and nitrite concentrations versus time in culture for oxygen-limited experiments conducted with feed solutions containing 3, 6 or 25 g L^{-1} $NaNO_3$. The lactic acid concentration in the feed was 100 g L^{-1} for each experiment. For comparison, an experiment was also performed under aerobic conditions (pO_2>30%)

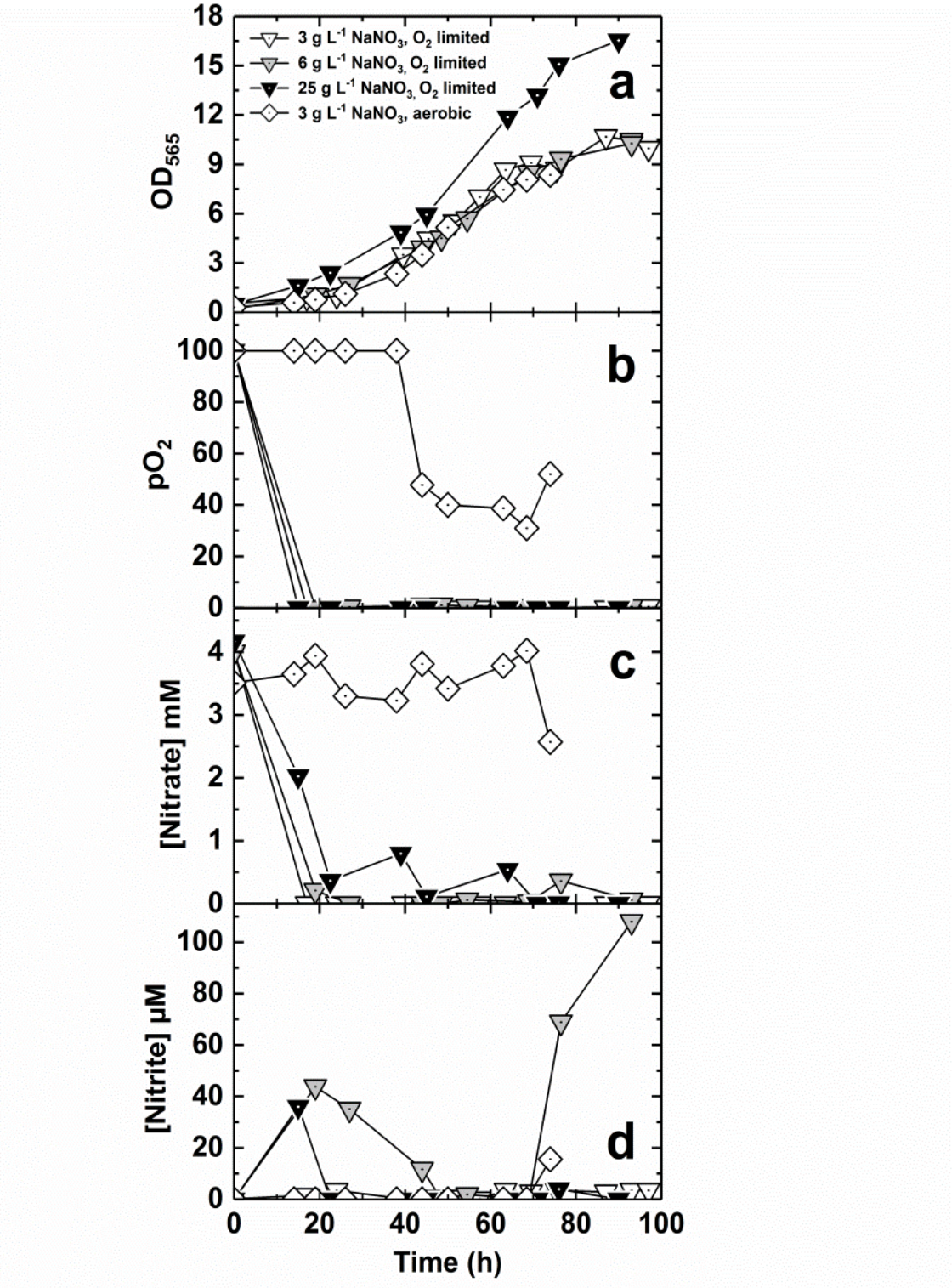

Figure 3.5. Comparison of oxygen-limited and aerobic fermentations conducted with different feed nitrate concentrations. Panels show OD_{565} (a), pO_2 (b), and nitrate (c) and nitrite (d) concentrations plotted against time. Samples were measured in duplicate for nitrate and nitrite analysis and in triplicate for analysis of iron content. Mean values are plotted.

with 6 g L^{-1} $NaNO_3$ in the feed. The nitrate concentration did not vary significantly during the

aerobic experiment, remaining around 4 mM during the exponential phase and decreasing to 2.6 mM at the end of the fermentation (Fig. 3.5c). The concentration of NO_3^- initially present in FSM was 4 mM (0.34 g L^{-1}) and, despite 54 mmol of NO_3^- being added to the fermenter during feeding (768 mL of feed was added), the NO_3^- concentration was steady (Fig. 3.5c). Nitrite concentration was also very low throughout, except for the last sampling point (15.6 µM NO_2^-). This suggests concurrent denitrification and aerobic respiration; this has previously been observed by Li et al. (Fernández-Castané et al., 2017). For oxygen-limited growth, nitrate was rapidly utilized when the pO_2 decreased to zero (Fig. 3.5b), and remained at very low concentrations in all experiments (Fig. 3.5c). In each case, nitrite concentrations transiently increased (Fig. 3.5d) following the onset of nitrate utilization (Fig. 3.5c), then decreased; nitrite concentration rose slightly during the course of some fermentations (Fig. 3.5d).

The effect of nitrate concentration in the feed had an impact on several bioprocess parameters (Table 3.4). Maximum growth rate (μ_{max}) was comparable for all cultures, whereas higher biomass concentration was achieved in the culture fed with 25 g L^{-1} sodium nitrate. The maximum growth rate was observed within the first few hours of oxygen-limited cultures. Growth rates before the point at which maximum C_{mag} was achieved (μ_b) did not show a clear correlation with nitrate concentration; however, all cultures had significantly decreased growth rates after the peak C_{mag}. Biomass to substrate yields ($Y_{x/s}$) before the time of maximum C_{mag} showed similar values except for the experiment with 3 g L^{-1} $NaNO_3$. FCM analysis (Fig. 6.7) shows that cells from cultures with the lowest nitrate feed concentration accumulated the most PHA, and had higher FSC and SSC (indicating a change in morphology) than cells grown at higher nitrate concentrations.

Table 3.4. Comparison of bioprocess parameters for cultures with varying feed sodium nitrate concentration.

$NaNO_3$ concentration in feed (g L^{-1})	μ_{max} (h^{-1})	μ^b (h^{-1})	μ^a (h^{-1})	$Y_{x/s}{}^b$	$Y_{x/s}{}^a$
3	0.08	0.047	0.018	0.55	0.3
6	0.09	0.069	0.02	0.23	0.23
25	0.08	0.052	0.015	0.26	0.23
6 (Aerobic)	0.07	0.058*		0.14*	

Key: μ^b and μ^a correspond to the growth rate before and after reaching maximum C_{mag}, and $Y_{x/s}{}^b$ and $Y_{x/s}{}^a$ are the corresponding yield coefficients; *values correspond to the exponential phase.

Table 3.5. Peak biomass (OD_{565}), iron concentration and C_{mag} measurements for pH stat cultures presented in Fig. 3.5.

Maximum value	$NaNO_3$ concentration (g L^{-1})		
	3	6	25
OD_{565}	10.7	10.3	16.6
Iron concentration (mg L^{-1})	19.2±0.2	19.4±0.3	54.3±0.4
Iron/DCW (mg g^{-1})	14.1±0.3	12.2±1.0	16.4±0.35
C_{mag}	2.58	2.35	2.14

For iron concentration values, mean values from 3 measurements are stated ± standard deviation.

Correlation of biomass and magnetosome production with nitrate supply was also investigated as shown in Table 3.5. The highest concentration of nitrate in the feed resulted in highest biomass concentration and quantity of cellular iron per litre of culture. However, C_{mag} values were>2.1 for all 3 nitrate concentrations, indicating highly magnetic cultures. Overall, whereas high feed nitrate concentration did not significantly increase the C_{mag} of bacteria, it did generate higher biomass concentration, and thus more magnetosomes per unit volume. Our results indicate that if pH-stat mode is used, $NaNO_3$ should be included in the feed solution to allow enhancement of magnetosome and biomass production. Future

work could determine if higher nitrate concentrations are able to support higher biomass concentrations.

3.4 Conclusions

We have developed a simple strategy for production of *M. gryphiswaldense* MSR-1 by employing a pH-stat operational mode adapted from previous studies. The advantage of this strategy is that it does not require tight and sophisticated control tools (gas blending, extremely sensitive oxygen probes) to achieve efficient biomass and magnetosome production. Biomass concentrations were obtained comparable to the highest published values to date (Yang et al., 2013; Zhang et al., 2011) using comparable analytical techniques. The concentration of two key nutrients in the feed solution, lactic acid and nitrate was also investigated. Lower concentrations of lactic acid in the feed increased final biomass concentration, whereas a high concentration increased cellular magnetism. There is therefore a need to balance the production of biomass and magnetosomes in the design and operation of these fermentation processes. The highest nitrate concentration tested (25 g L^{-1}) gave rise to the highest biomass concentration.

Flow cytometry has been shown to be a useful analytical strategy for the determination of bacterial physiology, morphology and PHA content, which can be used to guide process development. Bacterial ‘health’ was steady throughout fermentations. Cellular PHA content was shown to be inversely correlated to feed lactic acid concentration, and also correlated with scatter measurements.

Our study represents significant progress towards the implementation of rapid analytical techniques that will aid in the manufacture magnetosomes in industrial settings, itself a prerequisite of the application of magnetosomes in clinical and biotechnological applications. In conclusion, our work provides the research community with a relatively simple method to produce large amounts of magnetosomes using in *M. gryphiswaldense* MSR-1 grown in bioreactors.

CHAPTER 4

A fully scalable platform for the production and purification of magnetosomes from *Magnetospirillum gryphiswaldense* MSR-1

4.1 Introduction

Magnetosomes are nanometer-sized magnetic particles made by magnetotactic bacteria (MTB) under microaerobic conditions (Heyen and Schüler, 2003) with a size range of 35 – 120 nm, and are structured as chains within cells (Blakemore, 1975; Schüler, 2008). They are comprised of a core made of magnetite (Fe_3O_4) or greigite (Fe_3S_4) crystals (Lang, 2009), coated in a lipid bilayer containing a specific set of transmembrane proteins (Arakaki et al., 2008; Yan et al., 2012), with each coated particle unit connected side-by-side by a long filament of specific actin-like proteins (Uebe and Schüler, 2016) running the full length of the chain. The magnetosome membrane proteins (MMPs) can be used as anchors for the co-expression of fusion proteins using genetic engineering techniques (Bird et al., 2015). This, combined with several other unique properties conveying salient advantages over the use of chemically manufactured magnetic particles, means that magnetosomes have diverse potential in applications in biotechnology and medicine (see e.g.:(Alphandéry et al., 2011; Matsunaga et al., 2001; Mériaux et al., 2015; Tanaka et al., 2004a; Yoza et al., 2003). However, to realise such future applications widely requires development of commercial scale manufacturing platforms for magnetosome-based products. Previous chapters described the development of:

(i) a collection of new process analytical methods for assessing MTB growth, viability, physiology, biomineralization of magnetic iron minerals and changes in PHA content (Chapter 2); and
(ii) a robust pH-stat fermentation strategy appropriate for production of *Magnetospirillum gryphiswaldense* MSR-1 and magnetosomes therein (Chapter 3).

This work details experiments aimed at advancing a fully scalable integrated manufacturing platform for production, extraction, recovery and purification of magnetosomes. Specifically we investigate:

(i) cellular magnetic response, magnetosome size distribution, relative PHA content, and cell morphology during a pH-stat fermentation;

(ii) disruption of 20% (w/v) suspensions of centrifugally harvested *M. gryphiswaldense* MSR-1 in an industrial high pressure homogenizer (and small scale small scale ultrasonic devices) focussing on efficiency of magnetosome extraction and impact of the disruption process on magnetosome chain length, and influence of time in culture on the aforementioned parameters;

(iii) operating limits of bar magnets and commercial high gradient magnetic separator (HGMS) filter cartridges commonly employed for magnetosome purification, but specifically designed for selection of lymphocytes using dilute suspensions of (0.5 – 5% w/v) disrupted *M. gryphiswaldense* MSR-1 suspensions;

(iv) application of a 'state-of-the-art' rotor-stator HGMS for the recovery and partial purification of magnetosomes from 20% (w/v) disrupted MSR-1 cells; and finally

(v) a novel scalable alternative to traditional small scale sucrose density gradient centrifugation for final purification, namely magnetic micellar aqueous two-phase extraction.

4.2 Materials and methods

4.2.1 Strains, growth media and culture conditions

Magnetospirillum gryphiswaldense MSR-1 was obtained from Deutsche Sammlung von Mikroorganismen und Zellkulturen GmbH (DSMZ, Germany) and used for all experiments. Unless indicated otherwise, all chemicals were purchased from Sigma-Aldrich (Poole, Dorset, UK). Cryostocks of *M. gryphiswaldense* in 5% (v/v) DMSO were routinely grown in flask standard medium (FSM): 3.5 g L^{-1} potassium l-lactate; 100 µM iron citrate; 0.1 g L^{-1} KH_2PO_4; 0.15 g L^{-1} $MgSO_4 \cdot 7H_2O$; 2.38 g L^{-1} HEPES; 0.34 g L^{-1} $NaNO_3$; 0.1 g L^{-1} yeast extract; 3 g L^{-1} soy bean peptone; and 1 mL L^{-1} EDTA-chelated trace element solution

(EDTA-TES; (Widdel and Bak, 1992) replacing $MnCl_2$ for $MnSO_4 \cdot H_2O$. EDTA-TES contained: 5.2 g L^{-1} EDTA disodium salt; 2.1 g L^{-1} $FeSO_4 \cdot 7H_2O$; 30 mg L^{-1} H_3BO_3; 85.4 mg L^{-1} $MnSO_4 \cdot H_2O$; 190 mg L^{-1} $CoCl_2$; 4 mg L^{-1} $NiCl_2 \cdot 6H_2O$; 2 mg L^{-1} $CuCl_2 \cdot 2H_2O$; 44 mg L^{-1} $ZnSO_4 \cdot 7H_2O$ and 36 mg L^{-1} $Na_2MoO_4 \cdot 2H_2O$. Pre-cultures used for bioreactor inoculation were grown in FSM without iron source. The pH of FSM was adjusted to 7.0 with NaOH (Heyen and Schüler, 2003). Cells were grown at 30°C in a shaking incubator at 150 rpm.

The batch medium for bioreactor experiments consisted of FSM without iron citrate and feed solution contained: 50 – 200 g L^{-1} lactic acid; 3 – 25 g L^{-1} $NaNO_3$; 18 mL L^{-1} 25 – 28% $NH_3 \cdot H_2O$; 6 g L^{-1} yeast extract; 2.4 g L^{-1} $MgSO_4 \cdot 7H_2O$; 6 g L^{-1} $K_2HPO_4 \cdot 3H_2O$; 70 mL L^{-1} Mineral Elixir and 2 g L^{-1} $FeCl_3 \cdot 6H_2O$. The mineral elixir (pH 7) contained: 1.5 g L^{-1} nitrilotriacetic acid; 3 g L^{-1} $MgSO_4 \cdot 7H_2O$; 0.5 g L^{-1} $MnSO_4 \cdot 2H_2O$; 1 g L^{-1} NaCl; 0.1 g L^{-1} $FeSO_4 \cdot 7H_2O$; 0.18 g L^{-1} $CoSO_4 \cdot 7H_2O$; 0.1 g L^{-1} $CaCl_2 \cdot 2H_2O$; 0.18 g L^{-1} $ZnSO_4 \cdot 7H_2O$; 0.01 g L^{-1} $CuSO_4 \cdot 5H_2O$; 0.02 g L^{-1} $KAl(SO_4)_2 \cdot 12H_2O$; 0.01 g L^{-1} H_3BO_3; 0.01 g L^{-1} $Na_2MoO_4 \cdot 2H_2O$; 0.03 g L^{-1} $NiCl_2 \cdot 6H_2O$ and 0.3 g L^{-1} $Na_2SeO_3 \cdot 5H_2O$.

4.2.2 Cell harvesting and disruption

MSR-1 cells were harvested using a Beckman centrifuge (Beckman J2-21) at 7,500 g_{av} for 20 min, with a temperature control set at 4°C. Supernatant was removed and cells were stored at -20ºC for further use.

In cell disruption process, cells were first thawed at 4°C, and then suspended with 50 mM HEPES buffer, pH 8.0, to a final wet cell concentration of 20% (w/v).

Small scale disruptions were performed using 6 mL portions of cell suspension contained in 15 mL Falcon tubes. Cells were either: disrupted on ice using a Status US70 ultrasonic (20 kHz, 60 W) probe sonicator (Philip Harris Scientific, Lichfield, Staffs, UK) operated in ten bursts of 1 min duration (50% duty cycle) at 70% amplitude (power) with 1 min cooling of the probe in ice cold water between bursts; or treated in an L&R Ultrasonics 55 W T-9 ultrasonic bath (L&R Manufacturing Company, Kearny, NJ, USA) for 0.5 to 2 h.

High-pressure homogenization trials were initially conducted with 50 mL volumes of cell suspension using a 0.75 kW TS Bench Top High Pressure Cell Disruptor (Constant Systems Ltd, Daventry, Northants, UK) operated at various disruption pressures, *P* (5 – 20 kpsi) using 1 – 5 discrete passes, *N*. In later experiments larger quantities of cell suspension (250 mL) were subjected to a single pass at 10 kpsi.

4.2.3 Lab-scale recovery of magnetosomes

At small scale magnetosomes were recovered from disrupted cell suspensions using permanent bar magnets either with or without commercial HGMS cartridges intended for magnetic affinity cell sorting, MACS (Miltenyi et al., 1990).

MACS® LS separation columns[2] (Miltenyi Biotech GmbH, Germany) vertically positioned within a 0.5 T MidiMACS™ separator (Miltenyi Biotech GmbH, Germany) or between two 1.2 – 1.4 T '50 x 15 x 15 mm' Neodymium-Iron-Boron (NdFeB) block magnets (Q-50-15-15-N, Supermagnete, Gottmadingen, Germany), were equilibrated with 12 mL of 10 mM HEPES buffer pH 8.0, before loading with 2 mL or 5 mL volumes of varying concentrations (0.5 – 5% w/v) of MTB homogenate (corresponding to the application of 10 – 250 mg of weight cell

[2]A plastic syringe set-up featuring: a 1.2 mL syringe packed with a matrix of coated non-porous ferromagnetic spheres, creating a void volume of 0.4 mL; an 8 mL buffer reservoir; and a manual plunger.

mass). After the loading step, columns were washed *in situ* with a further 6 mL of equilibration buffer, before removing to 'zero field' and flushing with a further 12 mL of the same buffer.

Block magnets were also used to recover magnetosomes without using MACS cartridges. In this case single '60 x 30 x 15' mm NdFeB magnet (Q-60-30-15-N, Supermagnete) were placed against vertically positioned 50 mL Falcon tubes containing 25 mL of 20% (w/v) MTB homogenates for 0.5 – 1 h. The cloudy cell debris containing bulk phases were carefully aspirated off using a pipette, before adding 25 mL of 10 mM HEPES pH 8.0 buffer, removing from the magnet and resuspending the wet magnetic cakes with the aid of a vortex mixer. This procedure was repeated a further 9 times.

Fractions collected from all of the above procedures were retained for analysis of iron and protein contents and in some cases TEM analysis and were stored at 4 or -20ºC as appropriate.

4.2.4 Description and general operation of the bioHGMF system

The magnetic separator model 'chemagic 15 Durchfluss-Separator Birmingham' (PerkinElmer chemagen Technologie GmbH, Baesweiler, Germany) employed in this study is based on Franzreb and Reichert's (2006) patented 'rotor-stator' magnetic filter system. It is an improved version of the earlier similarly sized ProMagic system used by Brown et al. (2013)[3] and was developed specifically for the Birmingham team through a cooperative development involving M. Franzreb (Karlsruhe Institute of Technology, Eggenstein-

[3]Larger 'rotor-stator' magnetic separator prototypes have been used for demonstration of HGMF at technical scales (Müller et al., 2015; Garcia et al., 201) and cGMP rotor-stator HGMS are now available (Ebeler et al., 2018; https://www.andritz.com/products-en/group/separation/disc-drum-filters/hgms-high-gradient-magnetic-separator).

Leopoldshafen, Germany), ABBIS® bio process automation / Vulkan TechnicMaschinen-Konstruktions GmbH/ (Wiesbaum, Germany) and PerkinElmer chemagen Technologie GmbH (Baesweiler, Germany).

The main components of the bioHGMF system are described below and identified in Fig. 4.1a.

- Duran bottles of various size as reservoirs for feedstock, wash/elution buffer and CIP solution, and for collecting fractions.
- A variable speed bidirectional peristaltic pump.
- Two computer-controlled six-way valves for regulating liquid flow within the HGMF rig.
- An air-cooled 'ON/OFF' 0.28 T solenoid electromagnet equipped with bore temperature measurement.
- A separator chamber within the magnet bore housing a specially designed 'rotor-stator' magnetic filter arrangement (Figs 4.1c & 1d) coupled to a variable speed motor. The 'rotor-stator' filter (internal diameter = 60 mm; working volume = 250 mL) features a rotating shaft mounted with densely perforated discs interlocked with a two-part stationary assembly of densely perforated discs, to create an alternating arrangement of rotatable and fixed filter disks, spaced 3 mm apart (Fig. 4.1c & d) which play the role of matrix wires employed in conventional HGMS systems. According to the manufacturer, the magnetic filter capacity is sufficient to handle >25 g of chemically synthesized magnetic M-PVA supports.[4]
- A hollow copper coil between the separator chamber and the magnet bore for 'active cooling' with chilled (4ºC) tap water (Fig. 4.1b).

[4]In studies, employing a slightly smaller 'rotor-stator' filter operated close to its maximum holding capacity of ~20 g of M-PVA particles particle loss was estimated at just 0.1% per full operating cycle (Brown et al., 2013).

- A laptop computer equipped with TwinCAT IO control software (Beckhoff Automation Gmbh & Co KG, Verl, Germany) and Altova Authentic® protocol editing software (Altova GmbH, Vienna, Austria). Once programmed, the computer was able to record the temperature of the magnet, and control: the switching of the valve positions; the speed and direction of the pump; rotation of the rotor; and switching the magnet 'ON' and 'OFF' as required.

A schematic overview of the steps involved in magnetosome processing by HGMF system is presented in Fig. 4.2. To capture magnetosomes requires pumping disrupted *M. gryphiswaldense* suspensions to filter with the magnetic field switched 'ON' (Fig. 4.2. LOADING). Magnetosomes are strongly attracted to the magnetized surfaces of the perforated steel discs and are therefore retained within the filter, whereas cell debris and other non-magnetic components pass unhindered and are collected. Cell debris and other biological materials (loosely adsorbed or entrained within the magnetosome filter cake and suspended within the interstitial fluid after the loading phase) are displaced in subsequent washing steps performed *in situ* (Fig. 4.2, WASHING). For each of these, wash buffer (50 mM HEPES pH 8.0) is pumped to the filter, the magnetic field is then switched 'OFF' and the filter discs connected to the central motor driven shaft are rotated at 600 rpm (50% rotor power). The strong shear forces generated in the interfacial regions between the rotating and the fixed filter discs are sufficient to detach, resuspend and wash magnetosomes. At the end of each washing cycle magnetosomes are recaptured within the filter by turning the stirrer 'OFF' and magnetic field back 'ON', and the washings are collected. On completing the last wash cycle magnetosomes were recovered from the rotor-stator filter in elution and flushing cycles by resuspending with wash buffer with the stirrer 'ON' and field 'OFF', and then displaced from the filter chamber with the aid of the system's peristaltic pump (Fig. 4.2, ELUTION & FLUSH). Detailed descriptions of the HGMF experiments conducted are in the following section.

4.2.5 Recovery of magnetosomes from disrupted *M. gryphiswaldense* MSR-1 cells by HGMF

Prior to commencing HGMF, ice cooled (4ºC) 50 mM HEPES buffer pH 8.0 was recirculated through the whole system for 5 min at 14.4 L h^{-1} at' zero field' with stirrer 'OFF'. Following system equilibration 250 mL of cell homogenised (prepared by single pass disruption of a 20% (w/v) suspension of exponential phase *Magnetospirillum gryphiswaldense* MSR-1 in 50 mM HEPES buffer pH8.0 at 10 kpsi) was applied to the filter at a flow rate of either 0.6 or 3.6 L h^{-1} with the magnetic field turned 'ON' and stirrer 'OFF'. Magnetosomes were captured in the magnetized filter, whereas magnetosome-depleted feedstock passed through (Fig. 4.2, LOADING), and was collected as the 'non-retained' fraction. In some experiments the non-retained fraction was reloaded onto the magnetic filter multiple times in order to boost magnetosome recovery from the feedstock and increase the mass of magnetosomes retained.

With the field still 'ON', 250 mL of 50 mM HEPES buffer, pH 8.0, was then pumped through the filter (at either 0.6 L h^{-1} for 25 min or 3.6 L h^{-1} for 5 min in order to flush out any residual of feedstock and fill the filter and lines with wash buffer (Fig. 4.2, WASHING, left). The output from the rig was collected ('Wash 1'), before stopping the pump and resuspending the magnetosome particles in wash buffer by switching the magnetic field 'OFF and the stirrer 'ON' for 1 min at 600 rpm (Fig. 4.2, WASHING, right). Recollection of magnetosomes was initiated by switching the stirrer 'OFF' and the magnetic field back 'ON' for 1 min without pumping the process stream around the recycle loop; before initiating the next cycle by continuing collection of the washings at a flow rate of 0.6 or 3.6 L h^{-1} for 2 min (Fig. 4.2, WASHING, left). This washing regime as carried out three times, and the washes from the cycles were collected separately.

The first of two to five sequential elution cycles was then performed by pumping 300 mL of 50 mM HEPES pH 8.0 buffer into the filter at 7.2 L h^{-1} for 2.5 min at 'zero field' without stirring (Fig. 4.2, ELUTION, left). Eluting magnetosomes were collected in 100 mL aliquots. The flow was then shut off flow and the stirrer switched back 'ON' for 2 min at 600 rpm (Fig. 4.2, ELUTION, right) in preparation for the next elution cycle. In some experiments after completing the last elution cycle the filter chamber was flushed copiously with 720 mL portions of 50 mM HEPES buffer pH 8.0 at 7.2 L h^{-1} at 'zero field' without stirring until the flushed liquid was clear (Fig. 4.2, FLUSH). If not, pumping was stopped and the stirrer was switched 'ON' for 1 min at 'zero field', before performing a second flush cycle. All experiments runs concluded with cleaning-in-place (CIP) using 300 mL of 20% (v/v) ethanol for cell debris detachment delivered at 7.2 L h^{-1} with the stirrer switched 'OFF' (Fig. 4.2, CIP). Periodic measurements of the temperature of liquid streams (waste and product) exiting the rig during operation (2 – 4 h duration) were conducted off-line with an infrared Volcraft® IR 260-8S thermometer (Conrad Electronic SE, Wenberg-Köblitz, Germany). Fractions issuing from the runs were collected on ice. The volumes were recorded, small aliquots from each were removed for immediate analysis of protein and iron contents and preparation of samples for TEM, and the rest was stored at -20º C until required.

4.2.6 Further purification by density gradient centrifugation

Following partial purification at lab and HGMF scales magnetosome enriched samples (1 L containing 30 –35 mg of iron) were further purified by layering onto 4 mL cushions of 60% (w/v) sucrose in 10 mM HEPES buffer pH 8.0 contained in 10 mL Oak Ridge High-Speed

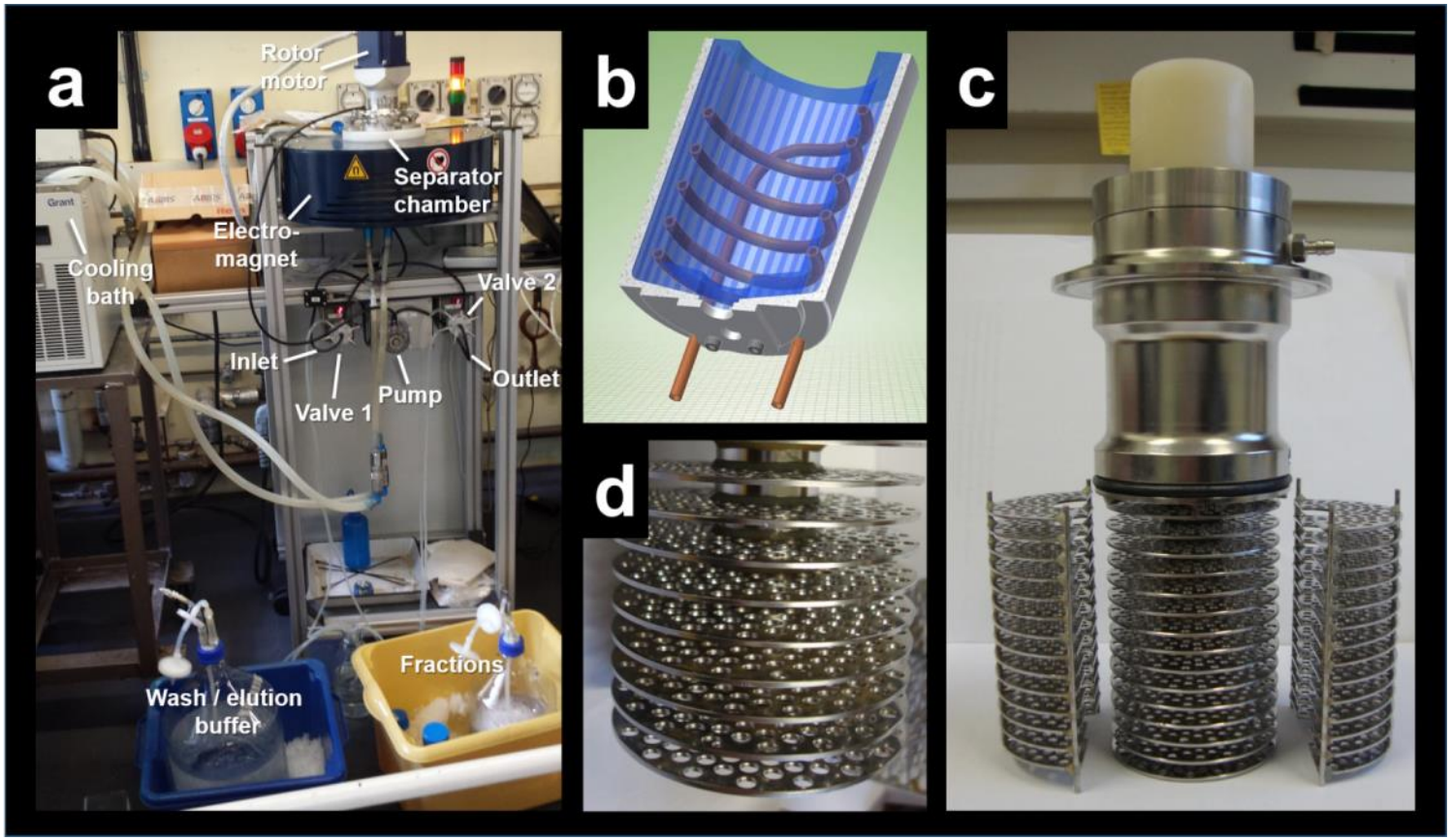

Figure 4.1. Durchflussseparator. (a) Annotated photograph of the chemagic 15 ‘rotor-stator’ magnetic separator set-up employed in this work. (b) Schematic of the filter chamber’s active cooling system (in reality the coil winding density is greater than illustrated). (c) Disassembled filter showing perforated filter discs mounted on a rotating shaft and two part stationary perforated filter assembly. (d) Close-up of rotating filter discs showing the perforations.

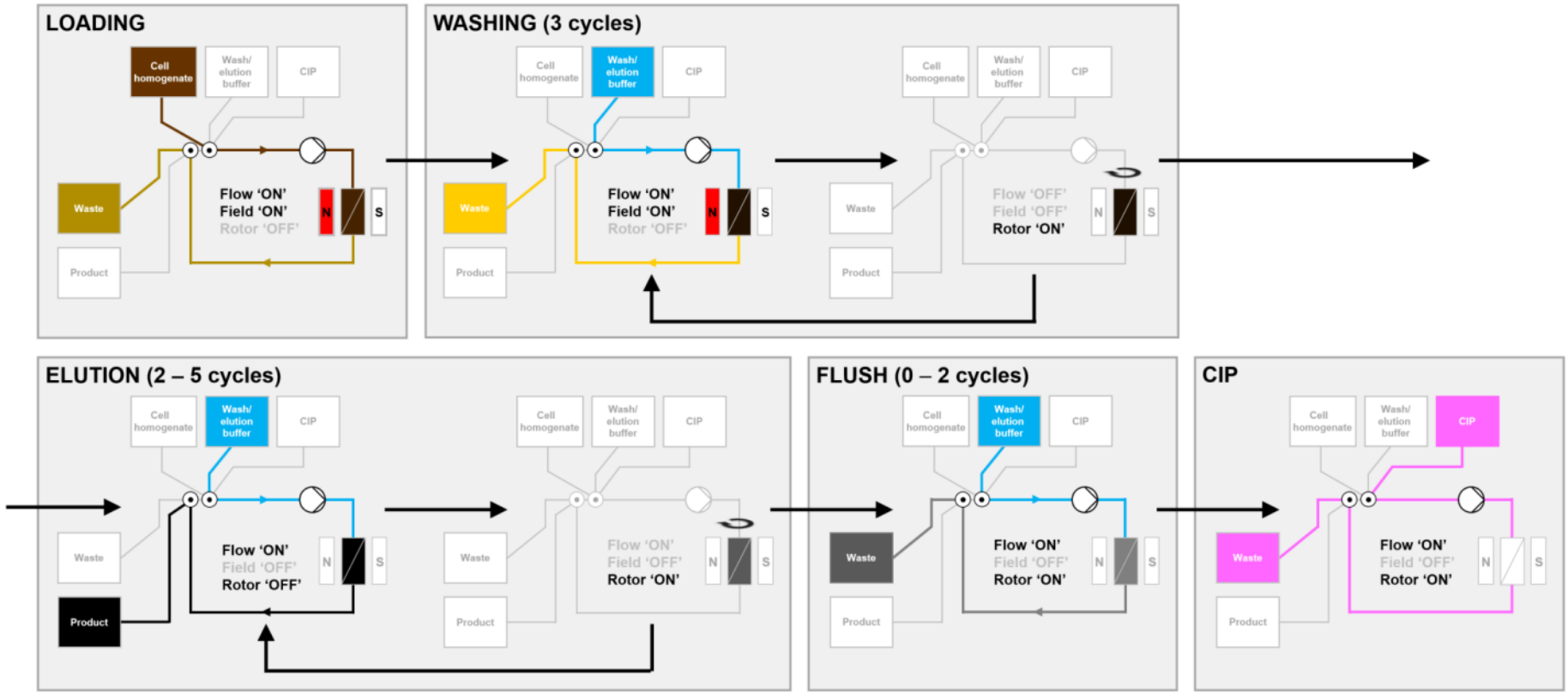

Figure 4.2. Schematic illustrations of the bioHGMF set-up employed in this study (see text for details). The equipment layout, general operation cycles and status of components (pump, magnet and rotor) and flow paths at the different stages are shown.

PPCO screw-cap round-bottomed centrifuge tubes (Model 3119-0010, Thermo Fisher Scientific, Loughborough, Leics, UK), before centrifuging at 50,000 g_{av} in the fixed angle rotor 'model 12111' (10 × 10 mL) of a Sigma 3K30 centrifuge (Sigma Laborzentrifugen GmbH, Osterode am Harz, Germany) for 2.5 h at 4°C. After centrifugation, the 'light' sucrose top phases were carefully removed using a Pasteur pipette, and 'heavy' magnetosome particles collected at the bottoms of the tubes, were resuspended in 10 mM HEPES buffer pH 8.0.

4.2.7 Magnetic aqueous two-phase extraction

Eluate fractions from HGMF experiments were employed for evaluation of magnetic aqueous two-phase extraction as a low cost scalable alternative to lab-based sucrose density gradient centrifugation. Two different aqueous two-phase systems were explored, i.e.: a classical PEG/phosphate combination (120 g L^{-1} PEG 8000 / 0.36 M K_2HPO_4 + 0.25 M KH_2PO_4, pH 8.0) (Divyashree et al., 2009); and a micellar aqueous two-phase system (15% – 20% w/v Eumulgin ES in 50 mM sodium phosphate, pH 7.0) used previously for demonstration of a continuous magnetic extraction process (Fischer et al., 2013). Two and half millilitre eluate samples containing 60 – 70 mg of iron were loaded on top of 10 mL of each mixed ATPS contained in Falcon® 6-well (i.d. = 34.6 mm, depth = 20 mm) flat-bottom cell culture plates (Corning, B.V. Life Sciences, Amsterdam, The Netherlands), which were immediately sealed and placed on top of a powerful Nd-Fe-B permanent magnet block (1.32 – 1.37 T, 110×89×19.5 mm; Supermagnete) before transferring to an incubator (MaxQ™ 4000 Benchtop Model SHKE4000-8C; Thermo Fisher Scientific, Loughborough, Leics, UK) without shaking, held at temperatures between 25 and 31°C. One hour later[5] the plate and magnet were carefully retrieved from the incubator and the separated phases were rapidly

[5]Preliminary experiments confirmed at least 0.5 h was required to meet the target temperature.

transferred (<5 min)[6] into different containers for subsequent determination of iron, protein, and PHA contents, and preparation for TEM analysis.

4.2.8 Analytical methods

Optical density: Culture optical densities at 565 nm (OD_{565}) were measured using a spectrophotometer (Evolution 300 UV-Vis, Thermo Scientific, UK) and data was collected using VISION*pro* software.

Cellular magnetism: Immediately after recording an optical density value the magnetic response of cells (C_{mag}) was measured on the same sample using a magnetic measurement system mounted within the spectrophotometer and built around its cuvette holder. For details of the C_{mag} monitoring system refer to Chapter 2 and Fernández-Castané et al. (2017).

Flow cytometry: A BD Accuri C6 flow cytometer (Becton, Dickinson and Company, Oxford, UK) was used to analyse bacteria and cell homogenates and determine efficiencies of cell disruption. Samples were resuspended in phosphate-buffered saline (PBS) and stained with SYTO™ 62. Samples were excited with a 488 nm solid-state laser. Forward scatter (FSC), side scatter (SSC) and fluorescence data were collected as detailed earlier (Chapters 2 & 3; Fernández-Castané et al., 2017, 2018).

Determination of protein content: Protein contents were determined using Pierce™ BCA Protein Assay Kits (Thermo Fisher Scientific, Loughborough, UK) and a Biochrom® Anthos

[6]These experiments were performed during a hot summer when the ambient temperature in the lab exceeded 25ºC; thus significant drops in temperature within the timeframe of phase recovery were unlikely.

Zenyth 340 microplate reader (Biochrom Ltd, Cambridge, Cambs, UK). For the measurements of total protein content (i.e. soluble plus insoluble) equal volumes of 2 M NaOH were mixed with turbid samples, and then heated at 99°C for 10 min before analysis.

Determination of iron content: Flame Atomic Absorption Spectroscopy (FAAS) was employed to determine iron contents in cell homogenates and in fractions collected during magnetosome recovery. A single element iron (248.3 nm) hollow cathode lamp (SMI-LabHut Ltd, Gloucester, Glos, UK) operated at a current of 30 mA with an acetylene (0.7 L min^{-1}) / air (4.0 L min^{-1}) flame in a Perkin Elmer AAnalyst 300 Atomic Absorption Spectrometer (Waltham, MA, USA). Sample preparation was done in triplicates as described previously (Chapter 3; (Heyen and Schüler, 2003; Fernández-Castané et al., 2018).

Transmission electron microscopy (TEM): Cell pellets or magnetosome containing samples were prepared for TEM by centrifuging at 16,873 g_{av} for 3 min in the FA-45-18-11 fixed angle (45º) rotor of an Eppendorf model 5418 centrifuge (Eppendorff, Hamburg, Germany), resuspending in 1 mL of 2.5% (v/v) glutaraldehyde in 0.1 M potassium phosphate, pH 7.2, and incubating for 1 h on a TAAB R052 rotator mixer (TAAB Laboratories Ltd, Reading, Berks, UK) at 4 rpm. The glutaraldehyde-fixed samples were subsequently dehydrated by sequential resuspension for 15 min each in increasing concentrations of ethanol in water (2×50%, 2×70%, 2×90% v/v) and twice in pure ethanol followed by twice in propylene oxide. Sedimented material from the last dehydration step were embedded in Mollenhauer (1964) resin by infiltration of the pellet with a solution containing 50% (v/v) Embed-812 (Electron Microscopy Sciences, Hatfield, PA, USA) in propylene oxide for 12 h on a rotator at 4 rpm in fume cupboard, followed by curing in undiluted Mollenhauer resin at 60ºC for 48 h on a rotator in a fume cupboard. Thin sections (120 nm) were cut from the resin block using diamond knives on a Reichart-Jung Ultracut Ultramicrotome (Leica Microsystems GmbH,

Wetzlar, Geramny). The cut sections were examined using a JEOL 1200EX TEM electron microscope (Jeol Ltd, Akishima, Japan) operated at 80 kV, in the transmission mode, with the beam current at 60 µA. Magnetosome chain lengths were determined by analysing TEM images. Size distributions for each sample were represented by plots of '% Cumulative mass undersize vs. Number of crystal units per chain', from which a characteristic median chain length, L_{50}, can be obtained. At least 800 magnetosome crystal units or 65 chains of magnetosomes were counted per sample.

PHA assay: PHA content in samples was determined using a fluorescence based assay. Pyrromethene-546 (Pyr-546) working solution (0.1 mg mL^{-1}) was added to 20% (w/v) suspended cells in 50 mM HEPES buffer pH 8.0 prior to disruption to a final concentration of 2 µg mL^{-1}. Fluorescence was measured with Mithras LB 940 microplate reader (Berthold Technologies, Bad Wildbad, Germany).

4.3 Results and discussion

4.3.1 Magnetosome chain length influences C_{mag}

Bioprocessing of magnetosomes starts with their biosynthesis during fermentation; changes in fermentation parameters gives rise to changes in the number, size and arrangement of magnetosomes within MTB. These differences would likely influence subsequent downstream processing of magnetosomes. It has been previously reported that the magnetic response (C_{mag}) of *M. gryphiswaldense* MSR-1 cells depends on the magnetosome content and arrangement (Schüler, 2008; Schüler et al., 1995; Schüler and Baeuerlein, 1998). In bioreactor experiments, the maximum C_{mag} values occurred before maximum biomass concentration was achieved (Fernandez-Castane et al., 2018; Wang et al., 2016; Yang et al., 2013). It has also been reported that higher C_{mag} values correspond to longer magnetosome

chains (Katzmann et al., 2013); therefore fermentation harvest time influences magnetosome chain length (Sun et al., 2011). Katzmann and co-workers observed that the length of magnetosome chains also varies with changing oxygen and growth temperature (Katzmann et al., 2013).

In this study, to characterise the starting material for our magnetosome bioprocessing route, we determined the number of magnetosomes and chain length in *M. gryphiswaldense* MSR-1 cells sampled at different time points (71.5, 112.5, 162.5 and 211.5 h) from a high cell density culture (Fig. 4.3a). TEM imaging and manual visual analysis (see Analytical Methods) were used to determine the size distributions of magnetosome chains (Fig. 4.3b).

C_{mag} values peaked during exponential phase before 71.5 h into the fermentation, and gradually dropped thereafter, whilst OD_{565} and intracellular iron concentration continued to rise (Fig. 4.3a). Magnetosome chain length was also the highest at 71.5 h among the four time points, and decreased progressively with time (Fig. 4.3b). For example, the maximum chain length in cells at 71.5 h was 32 crystal units, but it dropped to 10 after 211.5 h cultivation, 50% of the chains (mass basis) were between 8 and 18 units long at 71.5 h *cf.* 3 – 6.5 units at 211.5 h, and the median chain length fell from 12.5 to 4 crystal units.

These findings are consistent with previously reported transitions in cell shape and size from elongated to shorter rounder aspect on moving from exponential to stationary phase (Chapter 2; Fernández-Castané et al., 2017), increased PHA accumulation (Fig. 4.4; Chapter 2; Fernández-Castané et al., 2017), and observations that magnetosome length is tightly correlated with cell length (Staniland et al., 2010; Katzmann et al., 2011).

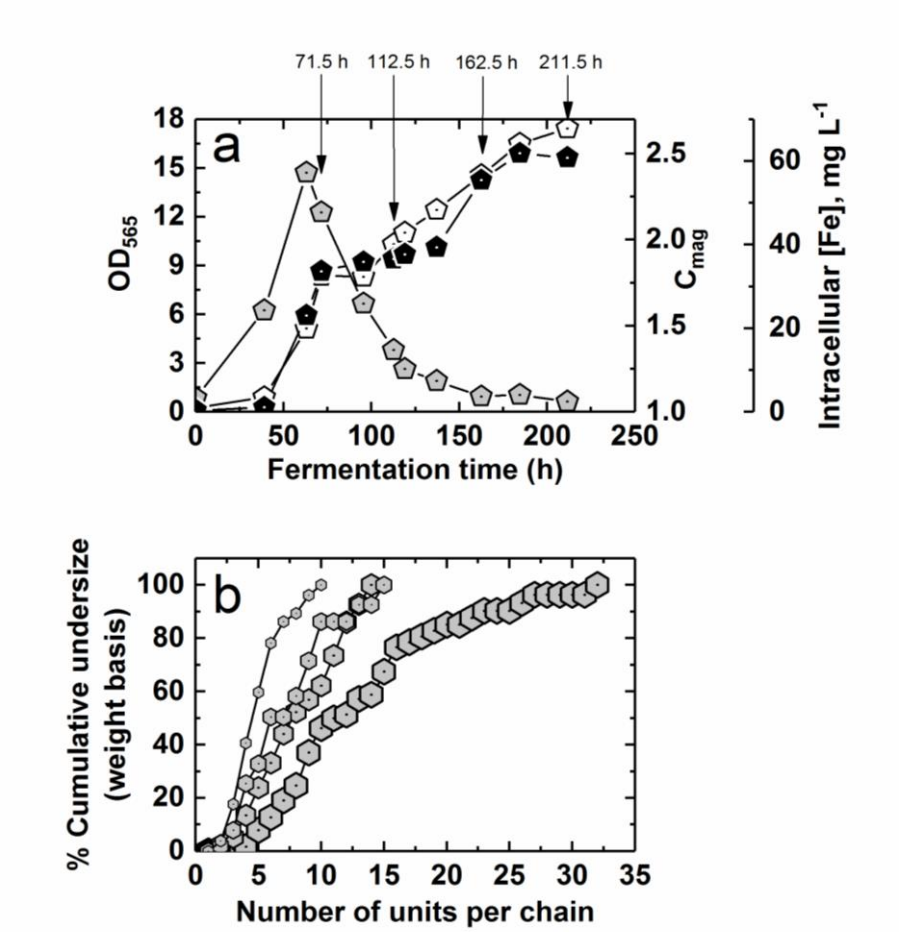

Figure 4.3. Influence of fermentation time during pH stat cultivation of *M. gryphiswaldense* MSR-1 on: (a) OD_{565} (white pentagons), C_{mag} (grey pentagon), and intracellular iron concentration (black pentagons); and (b) magnetosome chain length (grey hexagons of four different sizes reflecting different time points, i.e. the largest for 71.5 h, second largest for 112.5 h, second smallest for 162.5 h, and the smallest for 211.5 h in culture). At least 70 magnetosome chains were counted at each time point, and the size distributions (b) are presented by plots of '% cumulative mass undersize vs. number of units per chain'.

4.3.2 Comparison of magnetosome release methods

Several small scale mechanical methods have been employed for disruption of MTB, including French Pressing[7] (Ginet et al., 2011; Gorby et al., 1988; Grünberg et al., 2001;

[7]French pressure cell has been widely employed in MTB disruption, but pressures used for disruption vary widely between the different studies.

Xiang et al., 2007), probe (Kobayashi et al., 2006) and bath[8] based ultrasound methods (Alphandéry et al. 2009; Alphandéry et al. 2011; Alphandéry et al. 2012), but far little attention has been paid to development of standardized/optimised procedures, nor to comparative head-to-head evaluations of different methods on the basis of the disruption

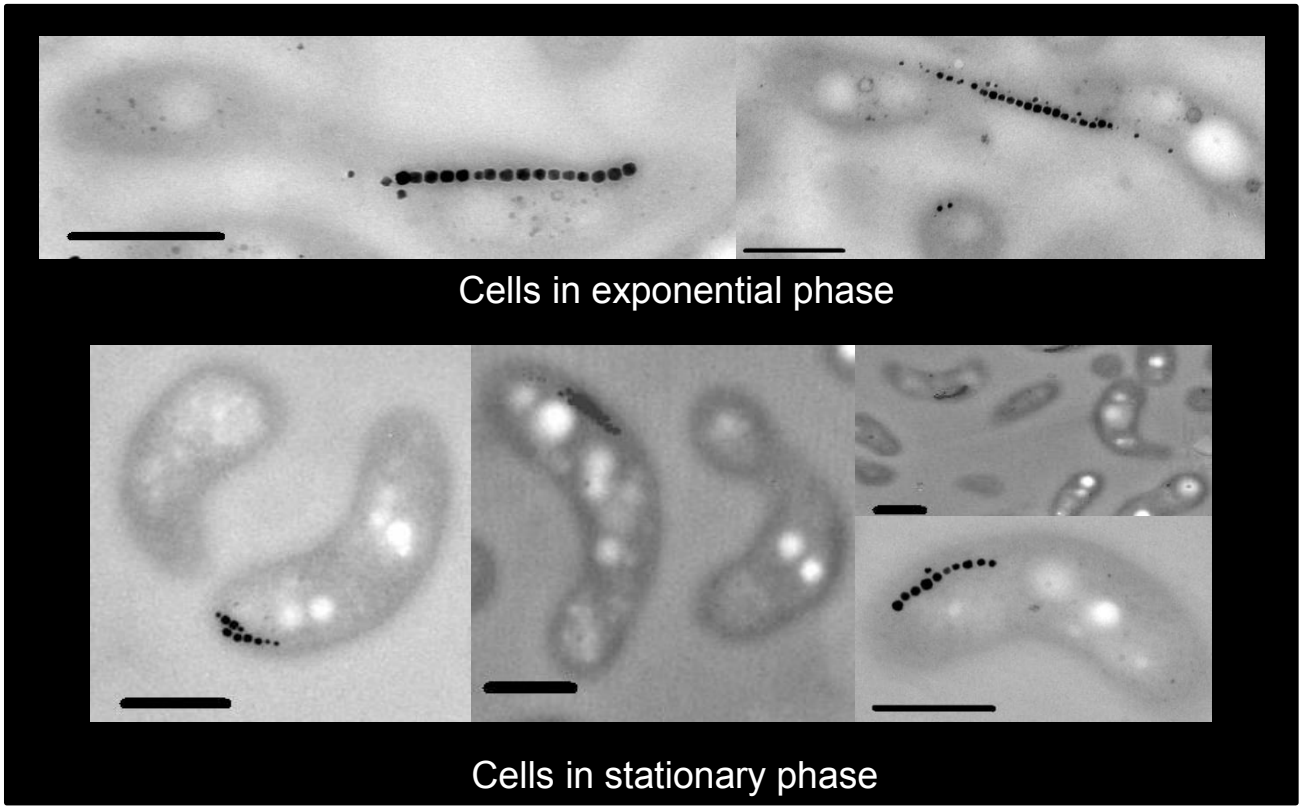

Figure 4.4. TEM images of exponential phase (71.5 h) and stationary phase (162.5 h) *M. gryphiswaldense* MSR-1 cells. Each scale bar represents 0.5 μm.

efficiency and impact of the disruption process on the size distribution of released magnetosome chains. In this study we have performed a systematic examination of the disruption of *M. gryphiswaldense* MSR-1 cells with: a Constant Systems Cell Disruptor CSCD),[9] which forces samples at high velocity through a specially designed valve assembly:

[8]Alphandéry and co-workers (2009, 2011, 2012) reported the use of ultrasonic bath at 30 W between 2 – 3 h to disrupt the cells and subsequently, release magnetosomes from *Magnetospirillum magneticum* AMB-1 followed by ten washing steps to purify the magnetic nanoparticles.
[9]A small industrial high-pressure homogenizer.

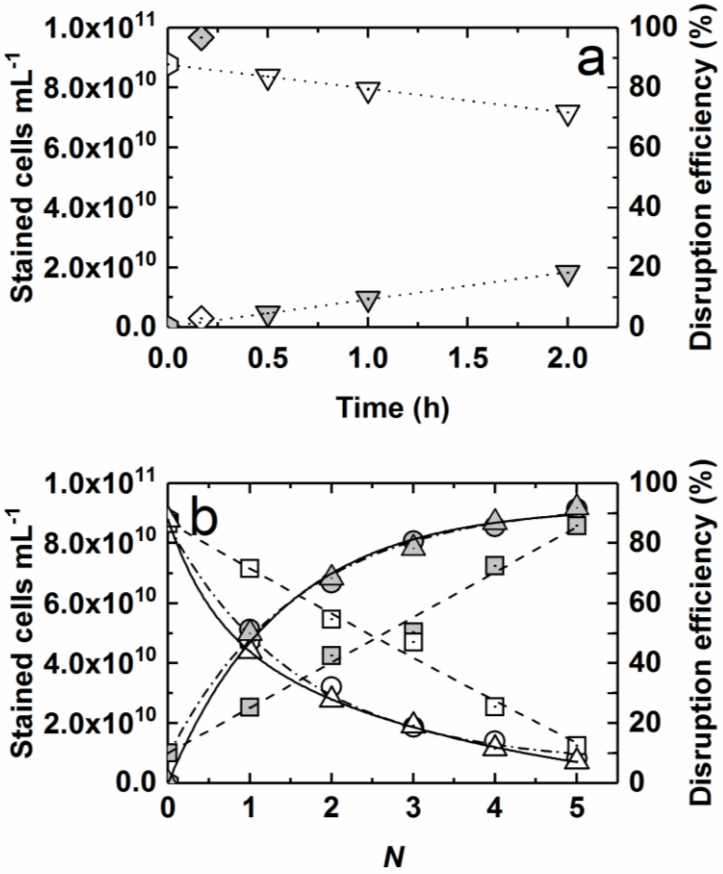

Figure 4.5. Comparison of ultrasonic bath, probe sonication and CSCD for disruption of 20% (w/v) suspensions of stationary phase *M. gryphiswaldense* MSR-1 cells. Plots show intact cell concentration (white symbols) and disruption efficiency (grey symbols) vs. (a) time of lab scale ultrasonic treatments; and (b) number of discrete passes at various operating pressures (5–20 kpsi) in the CSCD. Key: no disruption (hexagons); ultrasonic bath (down triangles and dotted line); probe sonicator (diamonds); 5 kpsi (squares and dashed line), 10 kpsi CSCD (circles and dash-dotted line) and 20 kpsi (up-triangles and solid unbroken line) in the CSCD.

cells are disrupted by different forces produced by interactions between the fluid and solid walls of the valve unit (Ayazi Shamlou et al., 1995; Middelberg, 1995; Kleining and Middelberg, 1996, 1998); and two lab-scale ultrasonic devices – an ultrasonic bath and a probe sonicator. A wet cell concentration of 20% (w/v) used in previous reports (Grünberg et al., 2004; Lang and Schüler, 2008) was also employed in this work. At this biomass concentration, the iron concentration was between 300 – 400 mg L^{-1}. Initial studies employed cells harvested at the stationary phase of growth. Cell disruption efficiency before

and after different disruption treatments was determined using flow cytometry to count the number of cells stained with the DNA dye, SYTO™ 62, per millilitre. Figures 4.5a and 4.5b compare the efficiency of disruption of stationary phase MSR-1 cells by the three apparatus. Unsurprisingly probe sonication demonstrated the highest efficiency of >95% after a 10 min treatment (Fig. 4.5a), whilst the ultrasonic bath was the least efficient, breaking only 20% cells after 2 h (Fig. 4.5a). CSCD disruption efficiency was tested at P = 5, 10, 20 kpsi whilst varying N.

The kinetics of CSCD disruption of stationary phase *M. gryphiswaldense* MSR-1 approximates to first order. A single pass through the disruptor disruption efficiency ruptured ~50% of the cells at 10 kpsi, two passes increased breakage to ~75%, and with every subsequent pass breakage increased, reaching >90% at N = 5 (Fig. 4.5b). Figure 4.6 compares size distributions of magnetosome chains before and after release from stationary and exponential phase MSR-1 cells by CSCD disruption at various combination of P and N, and Figures 4.7a and 4.7b show derivative plots of median chain length, L_{50} measured in crystal units, versus disruption efficiency and N, respectively. Though the largest size of magnetosome chain in intact stationary phase cells was 23 crystal units long, ~75% were below 15 crystal units, and the median magnetosome chain length, L_{50} was 11.5 crystal units. Exponential phase cells contained some longer magnetosomes (20% between 17 and 32 units length), but the L_{50} of exponential phase cells was slightly smaller than that of the stationary phase cells (i.e. 11 *cf.* 11.5) (Fig. 4.7). With increasing P and N the size distribution curves gradually shifted left to smaller chains and became increasingly steep (Fig. 4.6), providing clear evidence that chains of magnetosomes in intact cells were fractured into shorter and shorter chains during the cell disruption process (see Fig. 6.9 for

supporting TEM images). Scrutiny of 'L_{50} vs disruption efficiency' plots (Fig. 4.7a) for

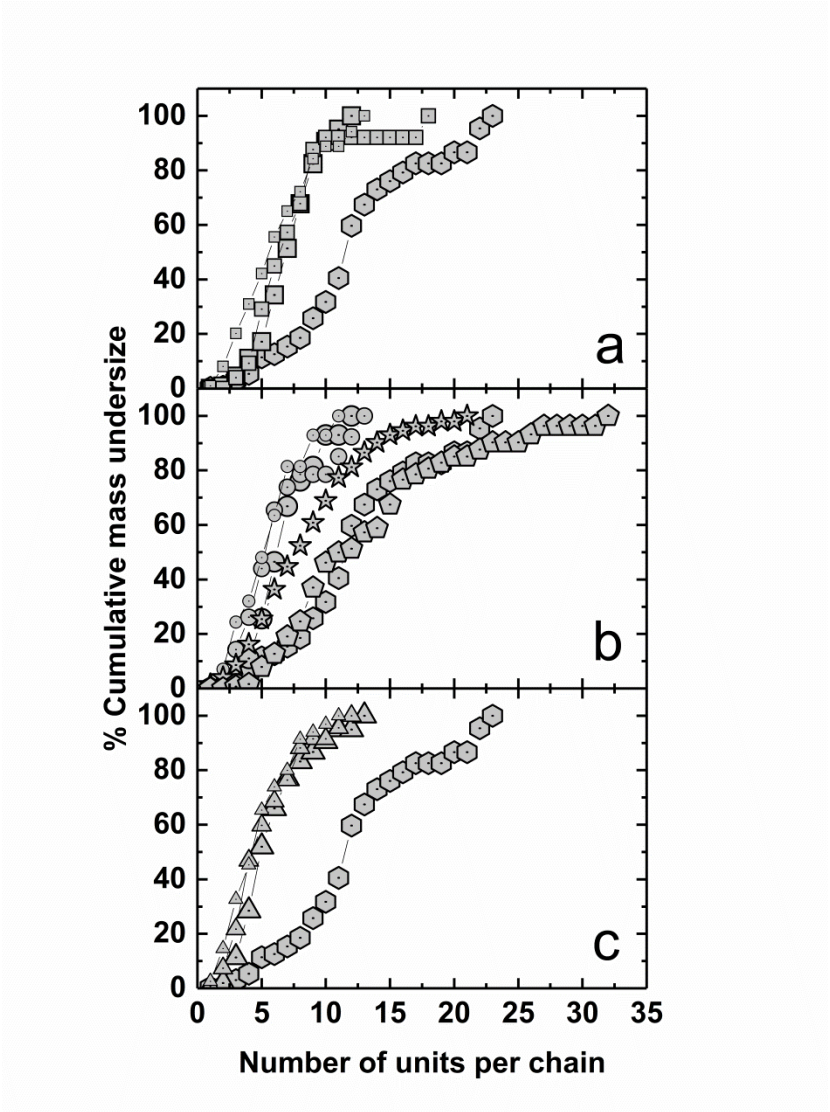

Figure 4.6. Effect of number of discrete passes, *N* and operating pressure, *P*, during disruption of 20% (w/v) suspensions of stationary and exponential phase *M. gryphiswaldense* MSR-1 cells in the CSCD on resulting magnetosome size distribution. Data are plotted as '% Cumulative mass undersize vs. number of units per chain'. At least 65 chains of magnetosomes were counted. Panels show operation at (a) 5 kpsi, (b) 10 kpsi, and (c) 20 kpsi. Key: intact stationary phase cells (grey hexagons); stationary phase cells after 3, 4 and 5 passes at 5 kpsi (grey squares decreasing in size with increasing *N*), stationary phase cells after 2, 3, and 4 passes at 10 kpsi (grey circles decreasing in size with increasing *N*), and stationary phase cells after 2, 3, and 4 passes at 20 kpsi (grey up-triangles decreasing in size with increasing *N*); intact exponential phase cells (grey pentagons); and exponential phase cells after 1 pass at 10 kpsi (grey stars).

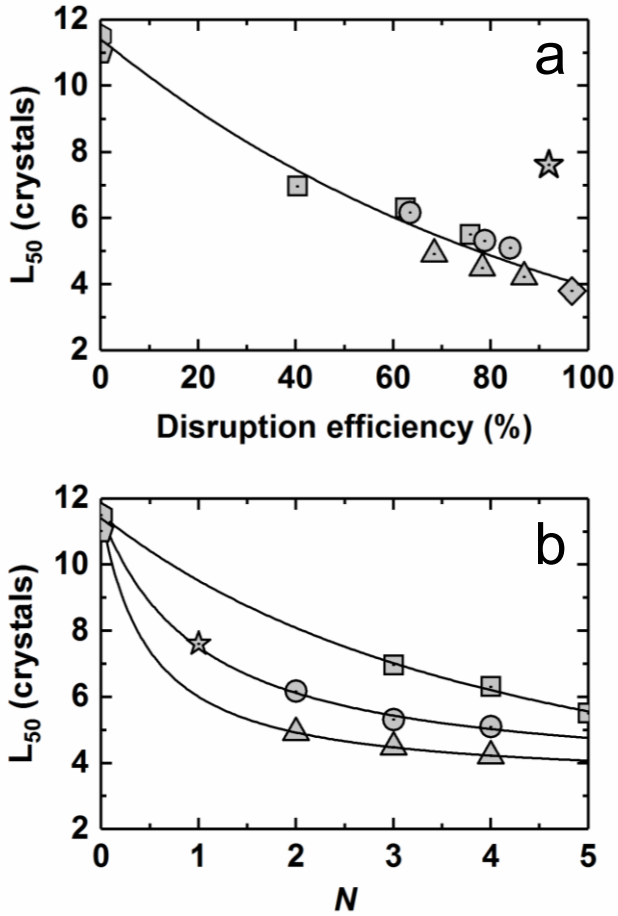

Figure 4.7. Dependence of median magnetosome chain length, L_{50} on (a) disruption efficiency and (b) variation in *N* and *P*, during disruption of 20% (w/v) suspensions of stationary and exponential phase *M. gryphiswaldense* MSR-1 cells. Key: intact stationary cells (grey hexagon); stationary phase cells after 10 min of probe sonication (grey diamond); stationary phase cells after 5 kpsi (grey squares), 10 kpsi (grey circles) and 20 kpsi (grey up-triangles) CSCD disruption; intact exponential phase cells (grey pentagon); and exponential phase cells after a single pass CSCD disruption at 10 kpsi (grey stars).

stationary phase cells reveals a clear trend, i.e. increasing disruption efficiency leads to progressive reduction in median magnetosome chain length. Moreover, over the range of pressures used (5 – 20 kpsi) plots of 'L_{50} vs *N*' (Fig. 4.7b) imply chain degradation in the CSCD is a first order process. To achieve efficient magnetosome recovery requires high disruption efficiencies of >80%, but under such conditions the L_{50} drops from 11.5 crystal units in the intact cell to below 5. Clearly, in the case of stationary phase cells there is a need to trade-off the degree of cell disruption and consequent recovery of magnetosomes from the cell against chain degradation inflicted during the disruption process. This does not

apply to exponential phase cells, which proved much easier to disrupt, i.e. one pass at 10 kpsi resulted in a disruption efficiency of 92% and small reduction in L_{50} from 11 (in intact cells) to 7.6 units long (Fig. 4.7a). Figure 4.8 investigates protein and iron release from stationary phase MSR-1 cells as functions of cell disruption efficiency. The release of protein follows first order kinetics, but iron release appears biphasic in nature, i.e. in the first phase (5 – 70% disruption) substantially hindered *cf.* protein release, in the second phase (>70% disruption) becoming increasing less so. This finding is understandable. Unlike much smaller sized proteins, release of much larger magnetosome chains from damaged cells is likely hindered. Increasing extents of disruption and concomitant reduction in chain length however, remove this barrier and so facilitate magnetosome escape. Beyond 70% disruption magnetome chains are reduced to increasingly small sizes (L_{50} = 5 and 3.8 units at 70% and 97% disruption respectively) thus magnetosome escape becomes easier, approaching the ease with which proteins are released (see Fig. 6.10). As noted earlier (Fig. 4.7a) exponential phase MSR-1 cells are much easier to disrupt than stationary phase cells. The quantities of protein (Fig. 4.9a) and iron (Fig. 4.9b) released from exponential phase cells in a single pass through the CSCD at 10 kpsi matched those released from stationary phase cells exposed to 5 passes at twice the operating pressure (Fig. 4.9a), and the magnetosomes released were significantly larger; compare size distribution profiles (Figs 4.6b and 4.6c) and L_{50} values (Fig. 4.7). Earlier reports established that the kinetics of disruption of unicellular microorganisms in industrial high pressure homogenizers follow first-order kinetics (Follows et al., 1971; Keshavarz-Moore et al., 1990a). Later studies showed that disruption kinetics in high pressure homogenizers depend on the type of microorganism, the conditions under which it is grown, the cell's age, wall strength, shape and size (Keshavarz-Moore et al., 1990b; Ayazi Shamlou et al., 1995; Siddiqi et al., 1995). For example, when *E. coli is* grown on a synthetic medium it is more easily disrupted than when grown on complex medium, and *S*. *cerevisiae* cells become increasingly more difficult to break on moving from exponential through to late stationary phase (Siddiqi et al., 1995). The observation here that a single pass of exponential phase *M. gryphiswaldense* MSR-1 cells at

a moderate pressure achieves near complete cell rupture shares similarities with Keshavarz-Moore and co-workers (1990b) study of a disruption of the filamentous fungus *Rhizopus nigricans*, who observed virtually complete release of soluble protein after the first pass at 10 MPa (<1.5 kpsi), with no increase in the amount of protein released at 50 MPa (7.25 kpsi). Against the above, the easier disruption of exponential phase MSR-1 cells *cf.* their stationary phase counterparts most likely reflects a more elongated shape and weaker wall structures.

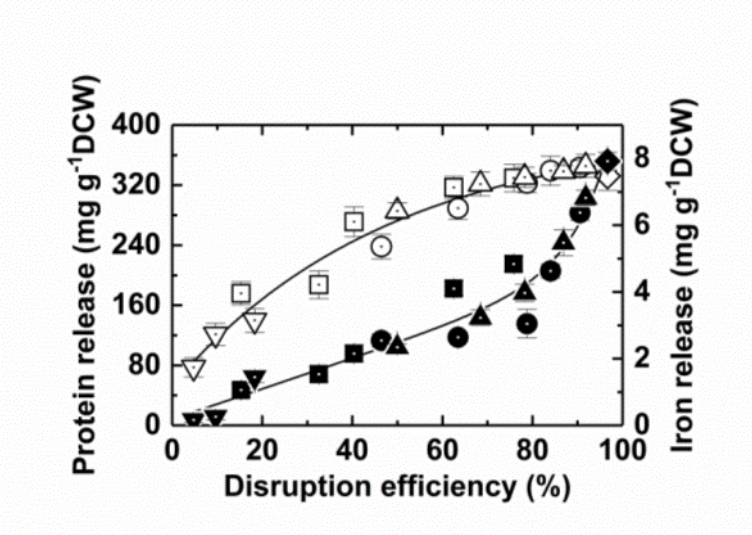

Figure 4.8. Dependence of protein (white symbols) and iron (black symbols) release on disruption efficiency of stationary phase *M. gryphiswaldense* MSR-1 cells. Key: ultrasonic bath treatment (down-triangles); 10 min probe sonication (diamonds); and 1 – 5 discrete passes through the CSCD at 5 kpsi (squares), 10 kpsi (circles) and 20 kpsi (up-triangles).

Of the lab-based ultrasonic treatments previously used by others, 10 min of probe sonication delivered the most complete rupture of stationary phase cells (97%) releasing 87% of the magnetosomal iron (Fig. 4.8), but inflicted the greatest damage on magnetosome chains reducing L_{50} to just 3.8 crystal units (Fig. 4.7a), whilst 2 h in the ultrasonic bath released too few magnetosomes (16% of the total; Fig. 4.8) from stationary phase cells for accurate size distribution analysis.

For reasons of scalability, ease of disruption and reduced chain degradation, in all subsequent downstream process development work (high gradient magnetic fishing and magnetic aqueous two-phase extraction) we employed exponential phase *M. gryphiswaldense* MSR-1 cells disrupted at 10 kpsi in a single pass through the CSCD. However, for small scale evaluations of MACS and bar magnet separations samples generated from the disruption experiments just described were employed (i.e. stationary phase cells disrupted in ultrasonic devices, exponential and stationary phase cells broken in the CSCD).

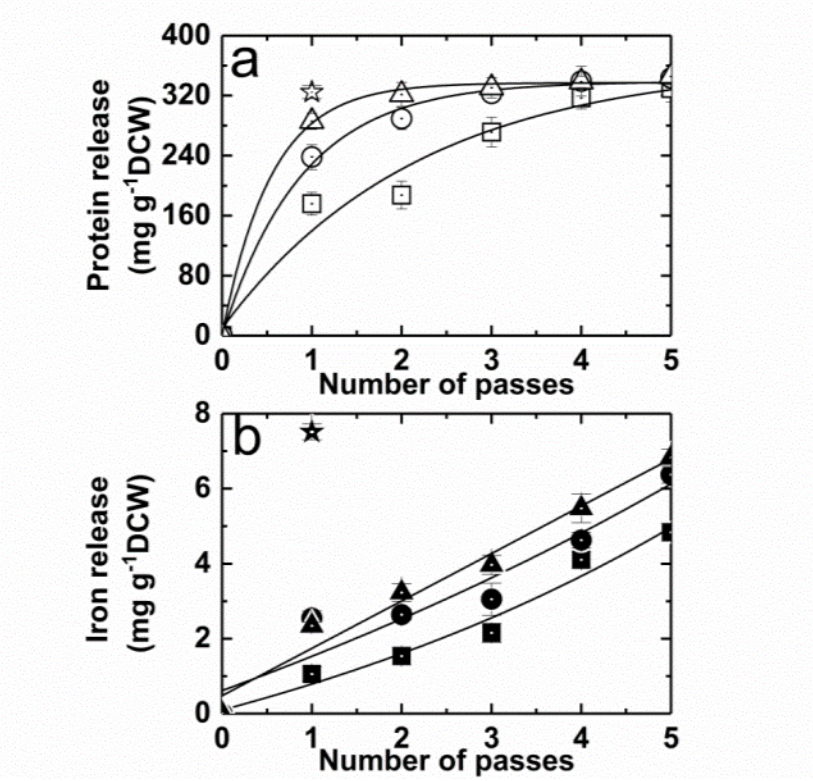

Figure 4.9. Dependence of (a) protein and (b) iron release on variation in *N* and *P*, during disruption of 20% (w/v) suspensions of stationary and exponential phase *M. gryphiswaldense* MSR-1 cells in the CSCD. Key: protein release (white symbols); iron release (black symbols); stationary phase cells after disruption at 5 kpsi (squares), 10kpsi (circles) and 20 kpsi (triangles); and exponential phase cells after disruption at 10 kspi (star).

4.3.3 Magnetosome recovery from CSCD homogenate by employing MACS cartridges

Magnetic-activated cell sorting (MACS) cartridges, comprising a cartridge filled with magnetic beads and a permanent magnet generating a 0.5 T magnetic field. MACS have been used for multiple applications such as separation of a large amount of cells (Miltenyi et al., 1990), rare cells from complex animal tissue (Lee and Lufkin, 2012) and have been used for magnetosome recovery (Grunberg et al., 2001; Uebe et al., 2011). However, to the best of our knowledge, no study has addressed the retention capacity and efficiency of such a technology. Hence, we performed a series of preliminary experiments to evaluate non-retained iron (washing steps), the recovery of magnetosomes (elution steps), and trapped iron after elution steps. We compared recovery yields from homogenates disrupted from stationary and exponential phase cells, trapped iron in MACS cartridges after elution, and elution efficiency calculated by the ratio of eluate and the sum of eluate and trapped iron (Fig. 4.10).

For MACS cartridge experiments, cell homogenates were diluted to ≤ 50 grams of wet cell weight per litre to avoid blockage of the cartridge. As shown in Fig. 4.10, the percentage of iron lost during cartridge loading (grey bars) increased at lower biomass concentrations. When 5 mL of homogenate having a cell concentration of 5 g L^{-1} (25 mg cells in wet weight) was loaded onto the cartridges, on average 30 % of the loaded iron was not retained on the columns in all the four experiments. When increasing the amount of disrupted cells loaded to the MACS column to 250 mg wet weight, iron yields were around 60 %, however, the cell homogenate from ultrasonic bath blocked the column. The elution yields (black bars) increased when the amount of biomass loaded increased, but it did not reach to a higher level. The non-retained iron in washing steps decreased when the amount of loaded cell homogenate increased, but the mass balance can't be reached when higher concentrations of cells were employed. For example, 13.6 % of iron was not retained in the column when bar magnets of 1.4 T were attached to the column, and 64.4 % of iron was collected in the

elution fraction after removing those bar magnets. Despite this, there was still 22.0 % of iron kept on the column that could not be eluted or washed out. This is hypothesised to be that cell debris cannot flow through the holes among the magnetic beads packed in the cartridge which kept the solid iron in the packed cartridge. A comparison between a commercial magnet and a bar magnet was done to evaluate the retention of magnetosomes (the second and the third experiments). Results showed that there was not a significant difference in recovery yield when the loading amount was the same. The comparison between different loaded samples after diverse disruption methods did not show yield or mass balance alteration either, except the homogenate after an ultrasonic bath. This is hypothesised to be due to the cell disruption efficiency using an ultrasonic bath was as low as 20%, therefore, numerous intact cells remained (i.e. much bigger than cell debris particles), which enhanced the trapping of solid iron in MACS cartridges. The elution efficiency was used to calculate the percentage of eluted iron retained on the MACS cartridges after washing steps. This illustrates that the more biomass loaded onto the columns, the lower the elution efficiency is (Fig. 4.11). Results showed that nearly 100% elution efficiency was achieved when 10 mg wet weight of disrupted cells was loaded (2 mL of 5 g L^{-1} sample).

According to our results, we considered that MACS cartridges have limited capacity in terms of the number of magnetosomes applied before the filters behave as depth filters, trapping biological material. Thus, sample dilution is necessary before loading the homogenate to MACS cartridges after cell disruption, however, this increases the working volume in the recovery steps. The maximum amount of cell debris that could be loaded onto a cartridge was determined to be 5 ml at a diluted concentration of 50 g L^{-1}. In this cell concentration, the iron amount is 0.5 mg, which means only 0.3 mg of the iron could be collected after each MACS cartridge. Moreover, the eluate contained cell debris which was blocked in the columns but eluted by flushing pressure. Thus, because of the non-scalable nature of the column, we moved to other magnetic recovery strategies.

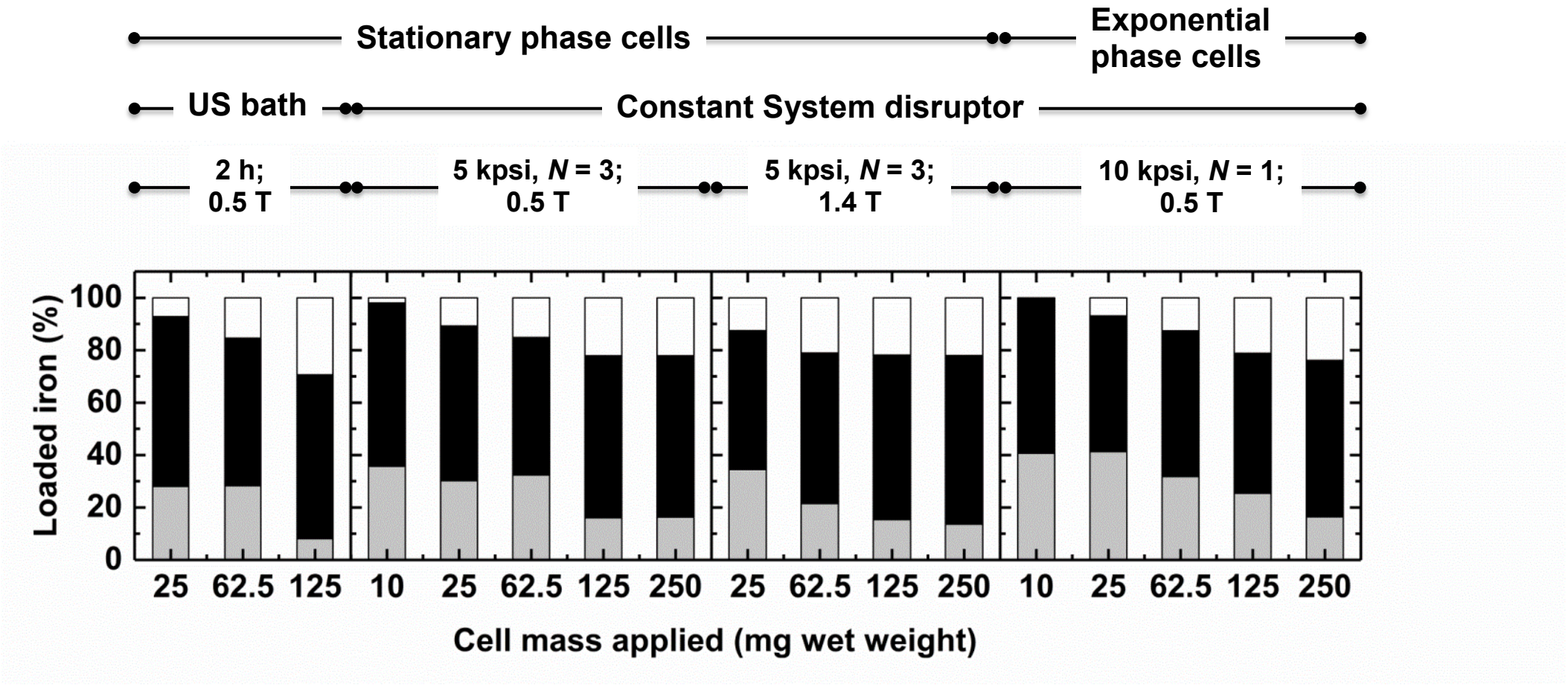

Figure 4.10. Effect of biomass loading on magnetosome (iron) recovery from MACS filters challenged with variously prepared 20% (w/v) *M. gryphiswaldense* MSR-1 homogenates. Key: non-retained iron recovered during loading and washing of magnetized MACS filters (grey bars); iron eluted from MACS filters at 'zero field' (black bars); and trapped iron (white bars).

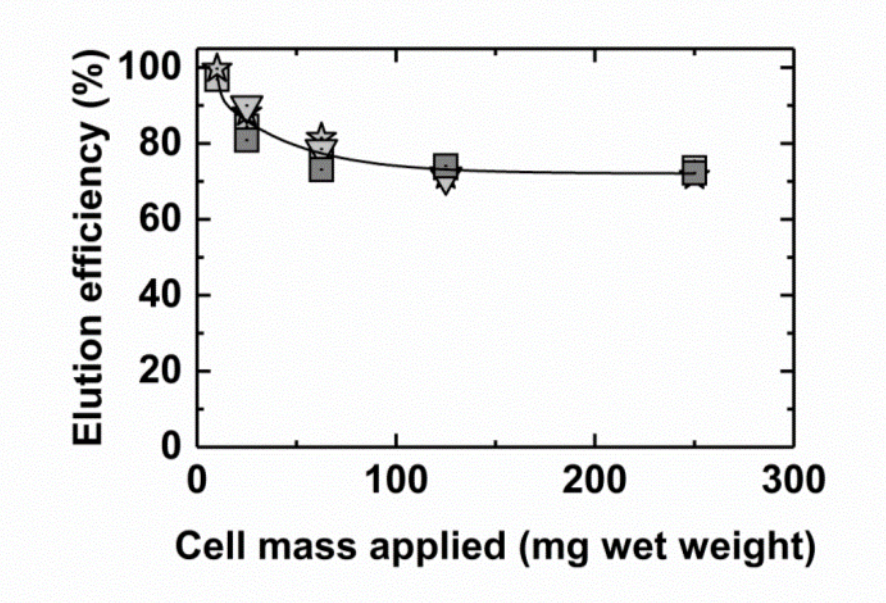

Figure 4.11. Dependence of magnetosome (iron) elution efficiency at 'zero field' on prior biomass loading of magnetized MACS filters. Elution efficiencies are calculated from the four data sets presented in Fig. 4.10. Key: stationary phase cells disrupted in an ultrasonic bath (2h, 55 W) and loaded on MACS filters in a 0.5 T field (grey down-triangles); stationary phase cells disrupted in the CSCD (*P* = 5 kpsi, *N* = 3) and loaded on MACS filters in 0.5 T (grey squares) or 1.4 T (dark grey squares) fields; and exponential phase cells disrupted in the CSCD (*P* = 10 kpsi, *N* = 1) and loaded on MACS filters in a 0.5 T field (grey stars).

4.3.4 Employment of bar magnet for the recovery of magnetosomes from homogenate

Another magnetic separation method that is commonly applied for the small-scale recovery of magnetosomes is serial washing. In Serial washing, a bar magnet is used to hold magnetic particles by placing it next to the container of homogenate and remove all the other non-magnetic debris after cell disruption. Using bar magnets and a series of washes represents a cost-effective alternative to the MACS cartridges. Bar magnets were employed to extract magnetosomes from homogenate after cells were disrupted using 10 washes of 10 mM Tris·HCl buffer (Alphandéry et al. 2011; Alphandéry et al. 2012). However, this strategy presents several limitations such as scalability, time consumption, and the necessity of manual operation.

Before each washing step (especially the first three washing steps after homogenisation), 60 minutes was required to let magnetic particles move toward the wall of the container next to the bar magnet. This might be because of the high viscosity of homogenate when it contains a large amount of cell debris. Unexpectedly, magnetosome loss still occurred, especially over the first three washing steps when a large amount of cell debris was contained in the homogenate (Table 4.1), which indicated that a longer time was required between each washing step.

Table 4.1. Comparison of magnetosome (iron) loss during washing steps after lab based ultrasonic and CSCD disruption of 20% (w/v) stationary phase *M. gryphiswaldense* MSR-1 cells. Errors indicate standard deviation, σ_{n-1} (n = 3).

	Magnetosome loss (%)		
Washing steps	Ultrasonic bath (2 h)	Probe sonication (10 min)	CSCD (*P* = 10 kpsi, *N* = 3)
1	20.5±0.4	7.8±0.2	14.3±1.3
2	16.0±1.3	1.8±0.4	7.5±0.9
3	15.6±0.9	1.1±0.2	8.4±0.1
4	11.2±0.6	0.6±0.1	3.4±0.2
5	10.4±0.4	0.2±0.1	1.0±0.1
6	3.8±0.14	0.2±0.0	0.7±0.0
7	3.5±0.12	0.1±0.0	0.3±0.0
8	1.4±0.08	0	0.4±0.0
9	0.7±0.0	0	0.2±0.0
10	0	0	0
Total loss (%)	59.2	11.5	31.7
Total recovery (%)	40.8	88.5	68.3

The amount of iron lost was greatest after cellular disruption using an ultrasonic bath, and the least using a probe sonicator. The magnetic response to a supplied magnetic field from

the strongest to the weakest from different cell disruption methods should be: ultrasonic bath > Constant System Cell Disruptor> probe sonication, depending on the chain length (from the longest to the shortest (Fig. 4.7a)). In contrast to this, the yield of magnetosomes showed that the highest yield was achieved after the release by probe sonication, whilst the lowest yield was observed after that by the ultrasonic bath. The reason might be variation in cell debris size, as bigger cell debris will interfere with the motion of magnetosomes towards the magnet.

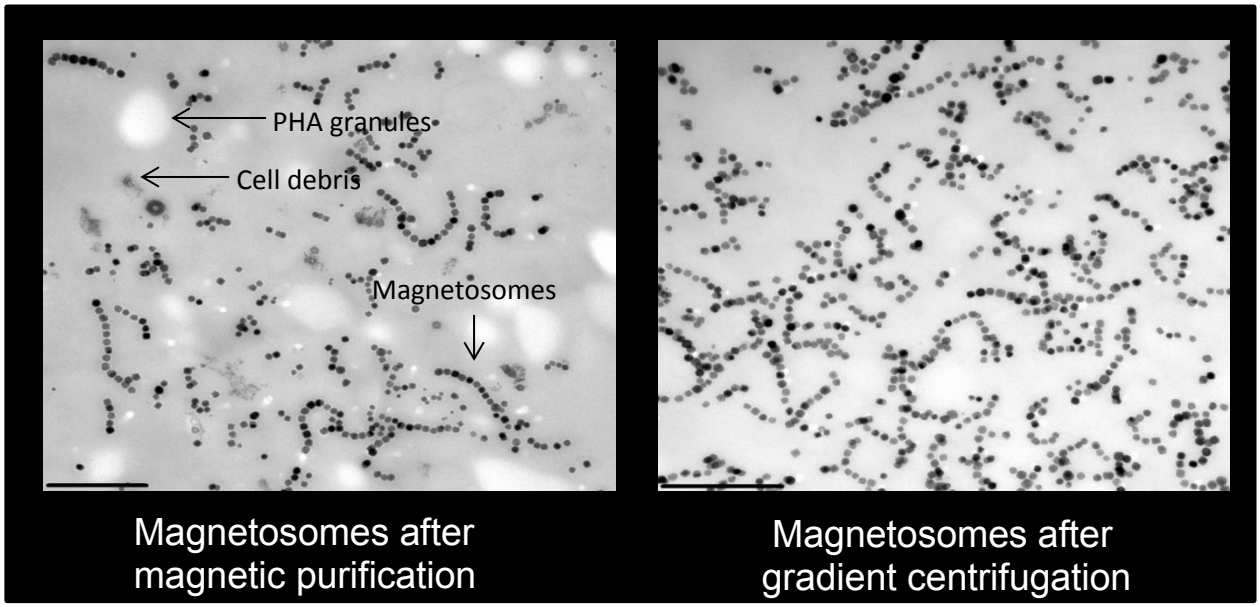

Figure 4.12. TEM images of magnetosomes from stationary phase M. gryphiswaldense MSR-1 cells following disruption in the CSCD (P = 10 kpsi, N = 3) and sequential purification on a magnet block and by sucrose gradient centrifugation. Each scale bar represents 0.5 µm

TEM pictures were taken after washing stages to illustrate the purification efficiency of washing steps (Fig. 4.12, left). Clear magnetosome chains can be observed as well as single magnetosomes and PHA aggregates. This demonstrates the advantage of limiting the production of PHA in fermentation. Also, some studies have demonstrated that there were proteins associated with PHA granules (Bresan et al., 2016; Jendrossek and Pfeiffer, 2014; Wahl et al., 2012) which may bind to magnetosome surface proteins. Thus, a density

gradient centrifugation (sucrose cushion) step was successfully used to remove PHA (Fig. 4.12, right).

As serial washing is a manual, time consuming, non-scalable method, presenting relatively low iron recovery and non-efficient PHA separation method, we used high gradient magnetic fishing (HGMF; Figs 4.1 and 4.2) for magnetosome purification.

4.3.5 Magnetosome recovery by HGMF

High gradient magnetic fishing was designed as a protein purification method by using magnetic adsorbent particles (Hubbuch et al., 2001). It allows adsorption, washing, elution and cleaning of the supports to be conducted in semi-continuous multi-cycle processing (Franzreb et al., 2006). Here we used HGMF to try to hold the released magnetosomes when the magnetic field is on and wash off impurities such as cell debris and proteins. Homogenate (250 mL) containing magnetosomes and cell debris prepared with one cycle in the high pressure homogeniser of exponential phase cells at 10 kpsi was loaded into the chamber of the rotor-stator at a flowrate of 3.6 L h^{-1} when the magnetic field was on. After being washed three times, 53.6% (20.5 mg) of solid iron was washed out, and then 21.8% (8.4 mg) solid iron was assembled in elution fractions. An additional 10.8 mg of solid iron was collected from the rotor-stator upon cleaning, although that iron could not be flushed out with HEPES buffer. Detailed results for magnetosome recovery in the single load cycle of HGMF are shown in Fig. 4.14 (Run 1) and Table 4.2a. We considered the iron measured had originated from magnetosomes because we only measured the iron in the pellet. This suggests that the solid iron that was spun down was only from magnetic particles, and the free iron was in the supernatant. The purification factor was calculated from the ratio of iron to protein contents in every fraction divided by the iron/protein ratio in the homogenate

before every experiment. The purification factor in this single experiment reached 8.9, and the average purification factor of the first four elution fractions was 7.9.

Table 4.2. Purification tables for the recovery of magnetosomes in HGMF operations. (a) single cycle of HGMF with high loading and washing flowrates (3.6 L h^{-1}) (Run 1), (b) multiple loading cycles of HGMF with high loading and washing flowrates (3.6 L h^{-1}) (Run 2), (c) single cycle of HGMF with low loading and washing flowrates (0.6 L h^{-1}) (Run 3), (d) reload of non-retained fractions from (c), single cycle of HGMF with low loading and washing flowrates (0.6 L h^{-1}), (e) single cycle of HGMF with a low loading flowrate (0.6 L h^{-1}), and high washing flowrate (3.6 L h^{-1}) (Run 4).

Table 4.2a. single cycle of HGMF with high loading and washing flowrates (3.6 L h^{-1}) (Run 1)

Fraction	Iron (mg)	Protein (mg)	Purification factor	Yield (%)
Homogenate	38.3±0.3	2200±27	1.0	100
Non-retained	14.1±0.2	1312±36	0.5	36.7
Wash 1	2.4±0.1	483±12	0.3	6.1
Wash 2	2.7±0.1	275±25	0.5	6.9
Wash 3	1.5±0.1	101±19.8	0.8	3.8
Elution fraction 1	3.6±0.0	27.7±0.5	7.4	9.3
Elution fraction 2	1.9±0.1	17.0±1.2	6.6	5.1
Elution fraction 3	1.5±0.0	9.8±0.2	8.9	3.9
Elution fraction 4	1.0±0.2	6.3±1.8	8.8	2.5
Elution fraction 5	0.4±0.0	11.5±3.6	1.9	1.0
Combined elutions	8.4	72.2	6.7	21.8
Trapped	4.2	82.6	2.9	10.8
Mass balance (%)	86.2	105.7		

To absorb more solid iron on the rotor-stator filter and increase the yield of magnetosomes in elution fractions, multiple load cycles of HGMF were applied for magnetosome recovery in a subsequent experiment (Fig. 4.13a). Figure 4.13b illustrates the iron concentration of non-retained fractions after each loading steps. The iron concentration was reduced from 58.3 mg L^{-1} to 23.7 mg L^{-1}, then after the next 9 more loading steps, the iron concentration

decreased to 16.9 mg L^{-1}. During these 10 loading steps, the loading volume (250 mL) was kept constant. After 3 washes, 47.5% (13.3 mg) of solid iron was washed out, while in the elution fractions, 41% of iron had been collected (Table 4.2b).

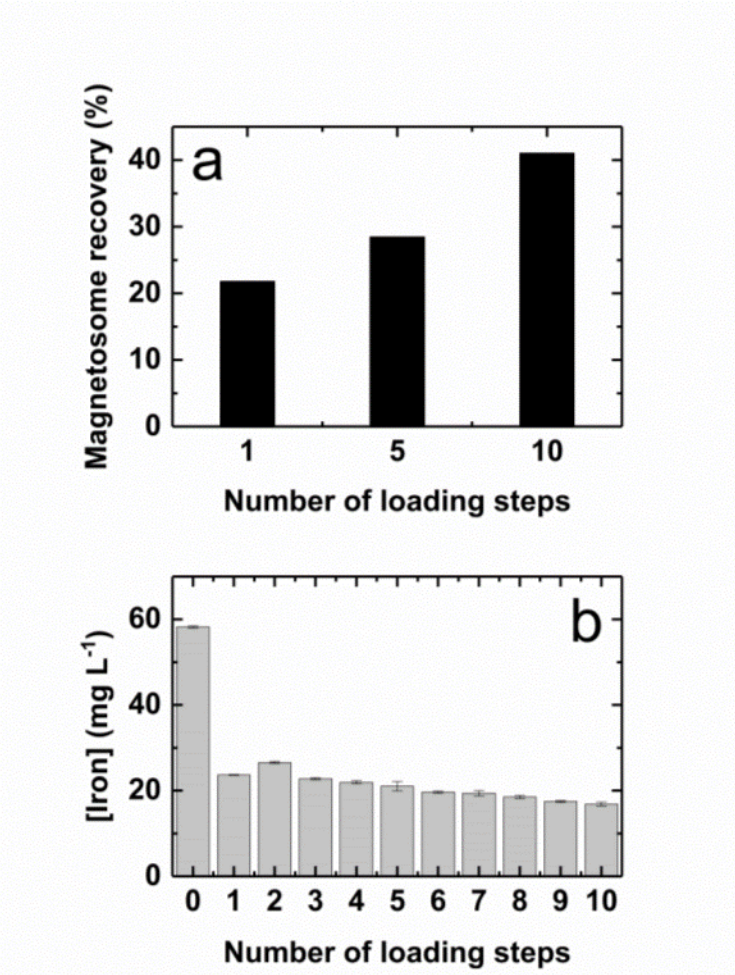

Figure 4.13. Impact of recycle loading during HGMF on magnetosome recovery. Plots show (a) magnetosome recovery vs. number of loading steps, and (b) iron concentration profile in the non-retained fraction during reloading.

The effect of multiple load cycles HGMF enhanced the performance of the rotor-stator filter compared to the single load HGMF, but the yield was only about 40% after a long operation time (Fig. 4.14, Run 2 and Table 4.2b). Thus, we evaluated another method to keep the magnetosomes in the filter during the washing steps, to reduce the flowrate of loading and washing steps.

Table 4.2b. Multiple loading cycles of HGMF with high loading and washing flowrates (3.6 L h^{-1}) (Run 2)

Fraction	Iron (mg)	Protein (mg)	Purification factor	Yield (%)
Homogenate	28.0 ±0.2	2898±43	1.0	100
Non-retained	6.6±0.2	1680±24	0.6	23.6
Wash 1	2.6±0.0	435±9	0.2	9.4
Wash 2	2.3±0.0	309±11	0.6	8.2
Wash 3	1.8±0.2	157±3	1.0	6.3
Elutions fraction 1-3	3.0±0.0	296±6	1.9	10.7
Elutions fraction 4-6	5.1±0.2	72.2±5.9	3.4	18.2
Elutions fraction 7-9	2.3±0.1	32.2±3.5	4.2	8.2
Combined elutions	10.4	401	2.7	37.1
Flushed out	1.1±0.2	87.7±3.2	1.3	3.9
Total recovery	11.5	489	2.4	41.0
Trapped	2.3	110	2.2	8.4
Mass balance (%)	96.9	109.7		

First, we changed the flowrate of both loading and washing steps from 3.6 L h^{-1} to 0.6 L h^{-1}, whereas the flowrate of the elution steps was kept at 7.2 L h^{-1} (Fig. 4.14, Run 3 and Table 4.2c)). In this cycle of HGMF, only 9.4% of solid iron was washed out before the elution step, and 70.5% of iron was collected in the elution fractions. However, 20% of the magnetosomes remained in the chamber of the 'rotor-stator' after elution. Therefore to increase the magnetosome yield by collecting more magnetosomes within the filter, the non-retained homogenate and wash fractions were re-applied and another cycle of HGMF was conducted. After this cycle, another 7.3 mg of solid iron, which was 8.8% of total iron loaded in the first cycle of HGMF, has been gathered in the elution fractions (Fig. 4.14, Run 3 and Table 4.2d). Thus, 79.3% of solid iron was collected in those two single cycle HGMFs. However, a purification factor of just 1.6 (Table 4.2c) illustrates that protein impurities cannot

be washed out from the rotor-stator chamber efficiently after the washing flowrate was reduced to 0.6 L h^{-1}. Figure 4.14 (Run 3) demonstrates that proteins were not only flushed out in washing steps but also at the beginning of the elution. The loading and washing steps in the first single cycle of HGMF took 100 min, which was much longer than the multiple load cycles of HGMF mentioned above (51 min). Moreover, the second single cycle of HGMF only collected 8.8% of total solid iron, but a lot of time was spent during the loading step. This is because the loaded volume had increased due to the washing steps in the first cycle. The unexpectedly high purification factor in the second single cycle of HGMF illustrated that magnetosome proteins had degraded during a long time of rotor-stator operation, because agglomerated magnetosomes on the magnetic filter were visible to the naked eye.

Table 4.2c Single cycle of HGMF with low loading and washing flowrates (0.6 L h^{-1}) (Run 3)

Fraction	Iron (mg)	Protein (mg)	Purification factor	Yield (%)
Homogenate	82.9±0.2	2222±54	1.0	100
Non-retained	0	16.8±0.6	N/A	0
Wash 1	4.2±0.0	536±17	0.2	5.0
Wash 2	2.0±0.0	494±31	0.1	2.4
Wash 3	1.7±0.0	338±18	0.1	2.0
Elutions fraction 1-3	6.0±0.10	340±20	0.5	7.2
Elutions fraction 4-6	10.3±0.1	214±7	1.3	12.4
Elutions fraction 7-9	10.9±0.2	118±7	2.5	13.1
Elutions fraction 10-12	10.3±0.1	71.3±3.9	3.9	12.4
Elutions fraction 13-17	11.2±0.1	61.1±3.5	4.8	13.5
Combined elution	48.7	804	1.6	
Flushed out	9.9±0.1	82.6±1.9	3.2	11.9
Total recovery	58.5	886.4	1.8	70.5
Mass balance (%)	80.0	102.2		

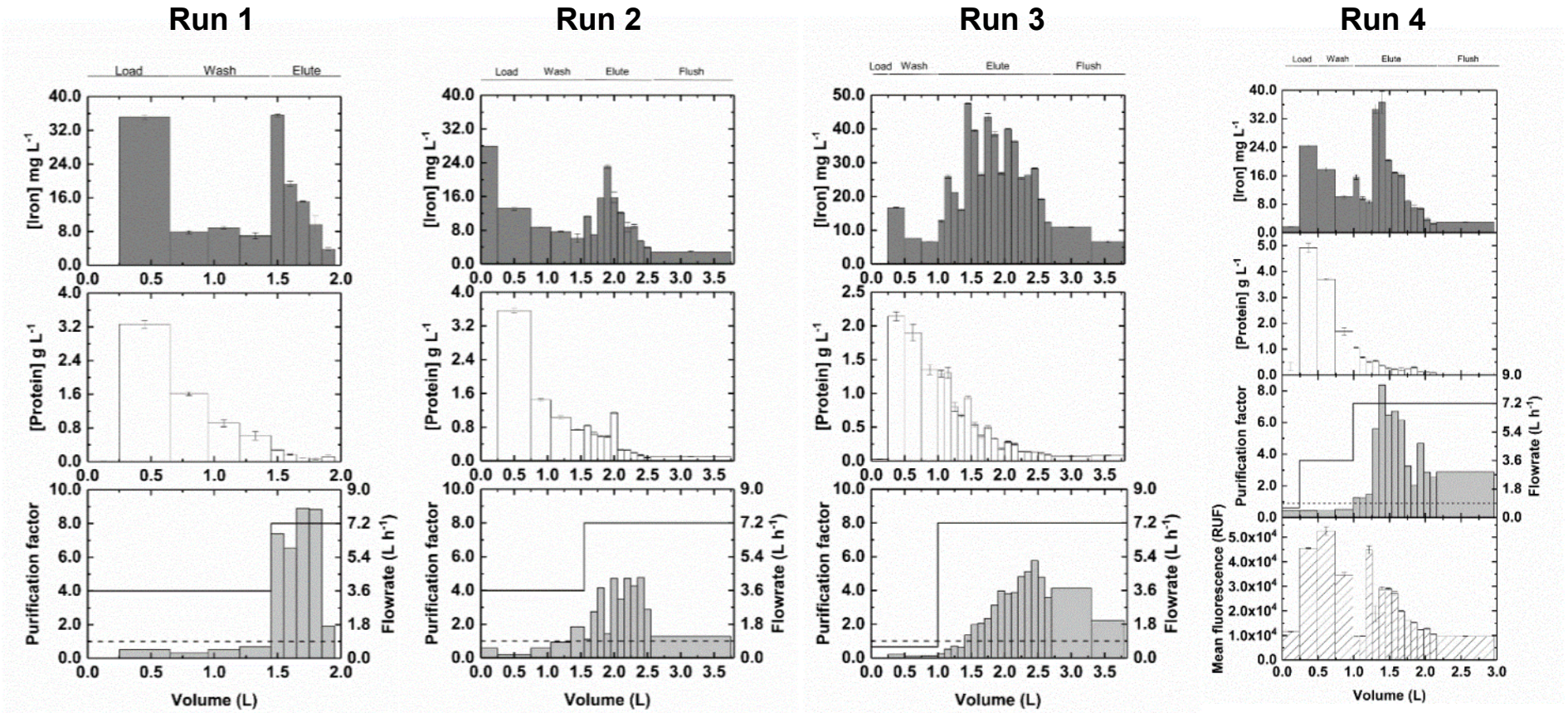

Figure 4.14. Tracking of magnetosomes, protein and PHA during HGMF of 20% (w/v) disrupted *M. gryphiswaldense* MSR-1 cells. Key: Run 1 – single cycle of HGMF with high loading and washing flowrates (3.6 L h-1); Run 2 – multiple load cycles of HGMF with high loading and washing flowrate (3.6 L h-1; Run 3 – single cycle of HGMF with low loading and washing flowrates (0.6 L h-1); and Run 4 – single cycle of HGMF with low loading flowrate (0.6 L h-1, but high washing flowrate (3.6 L h-1). The solid lines indicate the flowrate used, and the dashed lines indicate a purification factor equal to 1.

Table 4.2d. Reload of non-retained fractions from (c)

Fraction	Iron (mg)	Protein (mg)	Purification factor	Yield (%)
Reload	6.5±0.0	1282±16	0.9	N/A
Non-retained & wash 1	3.6±0.3	821±7	0.8	N/A
Wash 2	0.6±0.1	175±15	0.6	N/A
Wash 3	0.3±0.0	80.3±2.4	0.7	N/A
Elution 1	3.2±0.0	110±2	5.1	N/A
Elution 2	1.4±0.0	30.1±0.8	8.2	N/A
Elution 3	1.9±0.1	43.9±2.3	7.4	N/A
Combined elution	7.3	202	6.6	N/A
Flushed out	0.8±0.0	18.0±2.3	7.4	N/A
Trapped	2.6	16.0	28.6	N/A
Mass balance in total (%)	97.4	98.2		

With the aim of improving the removal of protein impurities and the capture of solid iron at the same time, another single cycle of HGMF was performed. The flowrate of loading step was still 0.6 L h^{-1}, but for the washing steps, the flowrate was increased to 3.6 L h^{-1} (Fig. 4.14, Run 4 and Table 4.2e). In this cycle, magnetosome loss before elution was 35.1%, while the yield of magnetosomes in elution steps was 50.3%, equating to an elution efficiency from the filter of 78%. Moreover, the magnetosomes were purified 3.3 fold with respect to protein (Table 4.2e).

In this series of HGMF experiments, the best overall increase in magnetosome purity was achieved in the first single cycle HGMF run (Table 2a, Run 1), i.e. the purification factors for the combined elution pool, and elution fractions 3 and 4 were 6.7, 8.8 and 8.9 respectively, but the magnetosomes yield (combined elutions 1 – 5) was only <22%. Because of the high flowrate used in loading and washing steps, cell debris and other impurities (soluble protein and insoluble materials) were effectively flushed out of the filter, however, there was also a loss of magnetosomes. To compensate for this, multiple-load-cycle HGMF was employed to

boost the filter's magnetosome loading, whilst keeping a high flowrate (3.6 L h^{-1}) during loading and washing stages for effective displacement of non-magnetic impurities. Figure 4.13b shows that the iron concentration in the first non-retained fraction was 22 mg L^{-1} *cf.* 58 mg L^{-1} in the load, thus the rotor-stator filter captured 59% of the solid iron in the first loading cycle. However, only an extra 12% was recovered over the next 9 cycles. As the volumes of each cycle were the same, we conclude that the use of multiple loading cycles is not an effective way to improve magnetosome capture within the filter. Meanwhile, compared with the single cycle HGMF, the ratio of flushed proteins has reduced, which caused the purification factors in the elution fractions to be lower. The highest purification factor in Fig. 4.14 (Run 2) was 4.7, therefore, another alternative for enhancing magnetosome capture, reducing the flowrate of load and wash steps to 0.6 L h^{-1}, was attempted (Fig. 4.14, Run 3; Table 4.2c). After reducing the flowrate, magnetosome loss before elution steps was decreased to 9.4%, but only 62.3% of the protein was flushed out at the same time. The protein maintained in the chamber of the rotor-stator resulted in reducing the purification factors in elution fractions. The elution fraction with the highest purification factor was 5.8, and the purification factors of first 4 elution fractions were lower than 1 (Fig. 4.14, Run 3). Thus, the purification efficiency needed to be improved, although the yield of magnetosomes in elution fractions was as high as 70.5%.

Two methods of enhancing the purification factor have been considered after the aforementioned HGMF experiments. First, increasing the buffer volume in washing steps, and second, increasing the flowrate in washing steps.

The experiment of single load cycle HGMF with a low flowrate loading and washing steps took 100 min, so if the volume of wash steps had been enlarged, the time spent on the steps before elution would be longer. Furthermore, the purification factor of the trapped

magnetosomes on the rotor-stator filter after the second single load cycle HGMF shows that the magnetosome proteins have degraded after a long time of operation. Thus, increasing the flowrate of washing steps was used to improve the purification factor in elution fractions.

Table 4.2e. single cycle of HGMF with a low loading flowrate (0.6 L h^{-1}), and high washing flowrate (3.6 L h^{-1}) (Run 4)

Fraction	Iron (mg)	Protein (mg)	Purification factor	Yield (%)
Homogenate	38.4±0.1	3302±53	1.0	100
Non-retained	0.4±0.0	80.2±42.7	0.4	1.0
Wash 1	6.1±0.1	1229±46	0.4	16.0
Wash 2	4.4±0.2	925±8	0.4	11.6
Wash 3	2.5±0.1	423±36	0.5	6.5
Elutions fraction 1-3	3.0±0.3	204±4	1.3	7.9
Elutions fraction 4-6	8.3±0.5	107±7	6.8	21.5
Elutions fraction 7-9	3.8±0.1	60.8±10.8	5.7	9.8
Elutions fraction 10-13	1.9±0.2	57.2±5.6	3.2	4.8
Combined elutions	17.0	428	3.4	44.1
Flushed out	2.4±0.1	71.4±0.0	2.9	6.2
Total recovery	19.3	500	3.3	50.3
Trapped	5.2	135	3.4	13.5
Mass balance (%)	98.9	99.5		

In the single load cycle of HGMF (Run 4; Table 4.2e) in which flowrates for loading and washing were 0.6 L h^{-1} and 3.6 L h^{-1}, respectively, 35.1% of solid iron and 80.5% of proteins were lost before elution. The efficient removal of protein conveyed better purification efficiency in elution steps, and the highest purification factor was 8.4 in the 5th elution fraction (Fig. 4.14, Run 4), which was close to the value achieved in the first single load cycle HGMF. The yield of magnetosomes was 50.3%, which was a good yield with efficient

removal of impure proteins. In Run 2 and Run 3, the highest purification factors were 4.7 and 5.8 in the 9th and the 15th elution fraction, respectively. However, the most efficiently iron-eluted fractions were the 4th or 5th among Run 2, 3 and 4. This result indicates that iron-rich elution fractions in Run 2 and 3 contained large amounts of proteins, whilst the highest purification factors appeared nearly the end of those elution steps with low iron concentration. In Run 4, both the highest iron concentration and purification factor turned up in the 5th elution fraction and most of the purification factors in the elution fractions afterwards were higher than 3. Thus, Run 4 increased the purification factor in the elution step, and collected a relatively high magnetosome yield.

After magnetosome extraction with HGMF, further purification of the elution fractions was needed to remove PHA and other residual impurities. Fluorescence data in Fig. 4.14 (Run 4) illustrates that PHA cannot be washed out just as efficiently as protein impurities. In the loading and washing steps of HGMF, 52% of PHA was flushed out, and 36.9% of PHA was collected in elution fractions (Fig. 4.14, Run 4). Fig. 15 (left) indicates that a large amount of PHA contained in the elution fractions after HGMF (Run 4). This result, along with TEM images (Fig. 4.12), demonstrates that PHA granules and magnetosomes were co-eluted.

4.3.6 Magnetosome purification using ATPS after HGMF

Although sucrose gradient centrifugation removed PHA from magnetosome samples previously recovered from cell homogenate on a bar magnet (Fig. 4.12), it is not a scalable technique. Accordingly, for the task of separating magnetosomes from residual PHA and cell debris, a magnetically enhanced density based separation approach was explored. Figure 4.16 shows a schematic illustration of the principles of this methodology. A classical method adapted from Divyashree et al. (2009) with PEG/phosphate combination was tested first.

Table 4.3. PHA and magnetosomes partitioning in the magnetic PEG 8000-potassium phosphate aqueous two-phase system. Key: sample 1: 20% (w/v) MSR-1 homogenate of exponential phase MSR-1 cells prepared by disruption in the CSCD (*P* = 10 kpsi , *N* = 1) ; sample 2: 10 – fold diluted 'sample 1' homogenate; sample 3: mixed elution fractions after HGMF; sample 4: 10-fold diluted 'sample 3'mixed elution fractions after HGMF. All the iron concentrations mentioned above were measured before centrifugation.

Samples	Iron concentration in samples ($mg \cdot L^{-1}$)	PHA in top phase (%)	PHA at interphase (%)	Iron in bottom phase (%)	Iron at interphase (%)
1	318.8	90.6	0	16.2	0
2	31.88	91.9	0	32.3	0
3	32.40	92.4	0	43.7	0
4	3.24	92.5	0	54.1	0

Table 4.3 shows different amounts of PHA that were applied and magnetosome separation in a system containing PEG 8000 and potassium phosphate. Results indicate that more than 90% of PHA remained after HGMF stage, which is stained by Pyr-546 can be separated from the bottom phase, but magnetosomes cannot be captured into the bottom phase efficiently by a permanent magnet. Given that magnetosome yield from HGMF elution fraction was only 43.7%, and that yield was increased insufficiently up to 54.1% after the loaded amount of iron was reduced to one tenth. We also tried to load homogenate containing a similar amount of iron into the ATPS after cell disruption by high pressure homogeniser to the sample taken from mixed HGMF elution fractions and diluted fractions but the iron yield in the bottom phase was only 16.2% and 32.3%, respectively.

Then, another aqueous two-phase system, Eumulgin ES, employed by Fischer and co-workers (2013), which has been reported to successfully separate magnetic nanoparticles under a magnetic field with a separation efficiency of >87%, was employed. Table 4.4

demonstrates that the permanent magnet can efficiently capture magnetic nanoparticles at the bottom of the ATPS. Both magnetosome yields with 15 and 20% (w/v) Eumulgin ES were >95% (96.3% and 97.7%, respectively), and >90% of PHA was separated into interphase and top phase at 29°C. Moreover, iron was measured in the interphase of samples 1 & 3 resulting in separation of PHA efficient (93.8% and 94.7%, respectively) at 25°C. Fischer and Franzreb, (2011) reported that in the Eumulgin ES - 50 mM sodium phosphate system, pH 7.0, the cloud point for phase separation was 24.5°C. This explains the higher loss of PHA to the interphase at 25 *cf.* 29ºC (Table 4.4). TEM micrographs before (Fig. 4.15, left) and after (Fig. 4.15, right) purification with 15% (w/v) Eumulgin ES - sodium phosphate ATPS at 29°C highlight the efficacy of this step in removing cell debris and PHA.

Table 4.4. PHA and magnetosome partitioning in the Eumulgin-sodium phosphate (50 mM) magnetic micellar aqueous two-phase system and during sucrose gradient centrifugation. The iron concentration before centrifugation was 34.1 mg L^{-1} in all the samples.

Samples	Temperature (°C)	pH	PHA in top phase (%)	PHA at interphase (%)	Iron in bottom phase (%)	Iron at interphase (%)
20% (w/v)	25	7.0	62.6	31.2	87.6	10.0
Eumulgin ES	29	7.0	74.2	15.7	97.7	0
15% (w/v)	25	7.0	75.5	19.2	88.7	2.0
Eumulgin ES	29	7.0	89.2	6.8	96.3	0
60% (w/v) Sucrose	4	8.0	89.2	0	71.7	0

In order to determine the reason for the observed differences in the yield between the two different ATPS employed, a series of density measurements were completed. Table 4.5 indicates that the densities of the bottom phases in Eumulgin and sodium phosphate system were 1.07±0.07 and 1.09±0.02 g mL^{-1} at 25 and 29°C, respectively, which were lower than that of other chemicals we measured. The density of the bottom phase in ATPS containing PEG8000 was 1.35 g mL^{-1}, which was even higher than the 60% (w/v) sucrose solution. Thus, in the PEG8000 - potassium phosphate ATPS, the buoyancy applied from the bottom

phase resisted magnetic nanoparticles being attracted to the bottom of the plates, although a 1.37 T permanent magnet was placed underneath.

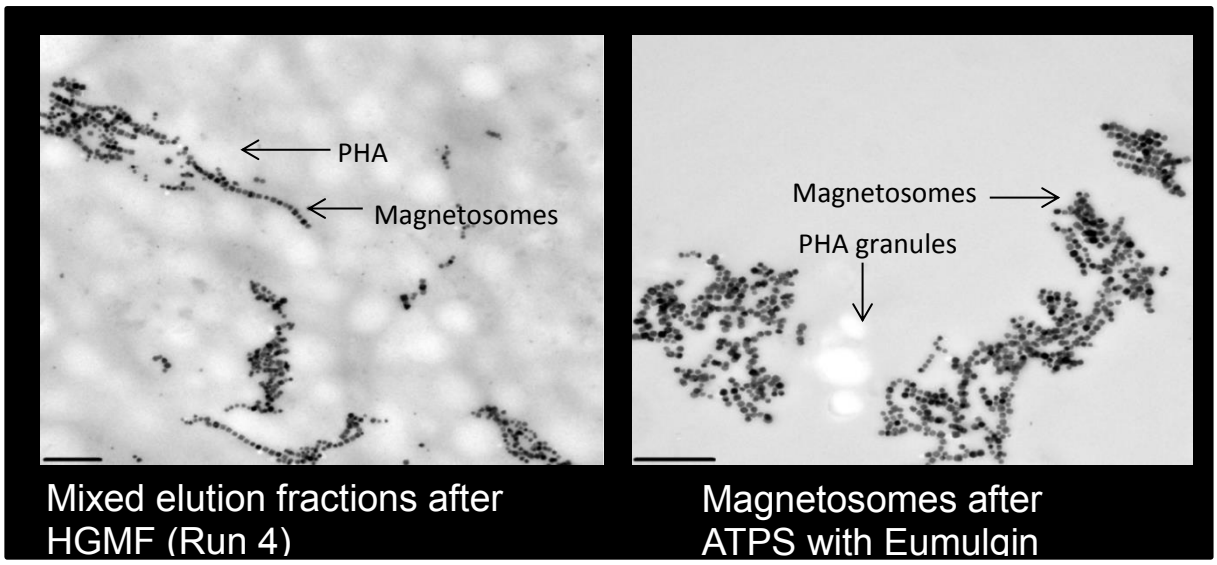

Figure 4.15. TEM images of magnetosomes from exponential phase *M. gryphiswaldense* MSR-1 cells following disruption in the CSCD (*P* = 10 kpsi, *N* = 1) and sequential purification by HGMF (Run 4) and magnetic micellar aqueous two-phase separation using a 15% (w/v) Eumulgin ES-sodium phosphate, pH 7.0 system at 29ºC. Each scale bar represents 0.5 µm.

Table 4.5 also illustrates that the density of the top phases of Eumulgin ES - sodium phosphate were between 0.94 – 0.97 g mL^{-1}, which means more than 60% of PHA granules produced by *Magnetospirillum gryphiswaldense* MSR-1 cells were lower than 0.94 g mL^{-1}. The sum of PHA in top phases and interphases were all more than 90%, thus of the density of PHA should be less than 1.07 g mL^{-1}, which also proved that PHA can be kept beyond sucrose cushion, and the bottom phase of PEG8000 - potassium phosphate ATPS. Since PHA granules can be separated efficiently, and iron yield was higher than 90%, the mixture of 15% (w/v) Eumulgin ES - 50 mM sodium phosphate system, pH 7.0 was considered. 29°C was used for incubation as the efficiency of phase separation for this system at this temperature showed the best results. By using this method, the iron yield was 96.3% in the bottom phase, and removal of PHA granules into the top phase was 96%. The yield of iron

after HGMF and aqueous two-phase separation was 48.5% (45% after adding the cell disruption efficiency of 92%), and the PHA removed was 98.5% after these two procedures. Since the density gradient of the two phases is much smaller than that when PEG8000/phosphate system was used, the efficiency of magntosome separation by using Eumulgin/phosphate after cell disruption directly has not been evaluated.

For the magnetosome separation from PHA, both sucrose gradient centrifugation and ATPS have been successfully employed, and the results indicate that both of them can separate PHA efficiently. By using a sucrose cushion, a high-speed centrifuge is required, and the amount of purified magnetosomes is limited by equipment. In contrast, ATPS is easier to scale-up, cost-effective and relatively time-saver, comparing with sucrose cushion. The yield of iron recovery using proper ATPS is higher than sucrose gradient centrifugation.

Table 4.5. Density of single phase in every ATPS, including 15% (w/v) Eumulgin ES in 50 mM sodium phosphate, pH 7.0, 20% (w/v) Eumulgin ES in 50 mM sodium phosphate, pH 7.0, 12% (w/v) PEG8000 in the mixture of 0.36 M K_2HPO_4 and 0.25 M KH_2PO_4,pH 8.0, and 60% (w/v) sucrose.

Samples	Temperature	Density (g mL^{-1})		Volume ratio
	(°C)	Top phase	Bottom phase	(Top/bottom)
20%(w/v) Eumulgin ES	25	0.95±0.04	1.07±0.07	0.94
	29	0.94±0.21	1.07±0.06	0.67
15% (w/v) Eumulgin ES	25	0.96±0.01	1.09±0.02	0.47
	29	0.97±0.02	1.08±0.02	0.28
PEG/Phosphate	29	1.03±0.14	1.35±0.09	0.77
60% (w/v) Sucrose	4	1.30±0.01		N/A

Our aqueous two-phase separation with Eumulgin ES – sodium phosphate and a permanent magnet indicates that our work is very promising to scale up, according to the research of Fischer and co-workers (2013). They demonstrated that they employed a technical-scale

'continuous magnetic extraction' process with a Eumulgin ES – sodium phosphate aqueous two-phase system and a permanent magnet to extract nano-scaled magnetic adsorbents from a crude *E. coli* cell extract with a flowrate of 9 L h^{-1}. The separation device was effective for continuous separation of a wide range of magnetic particle sorbents (from 2 µm diameter to 25 nm). The system employed by Fischer is described in Appendix 6.11.

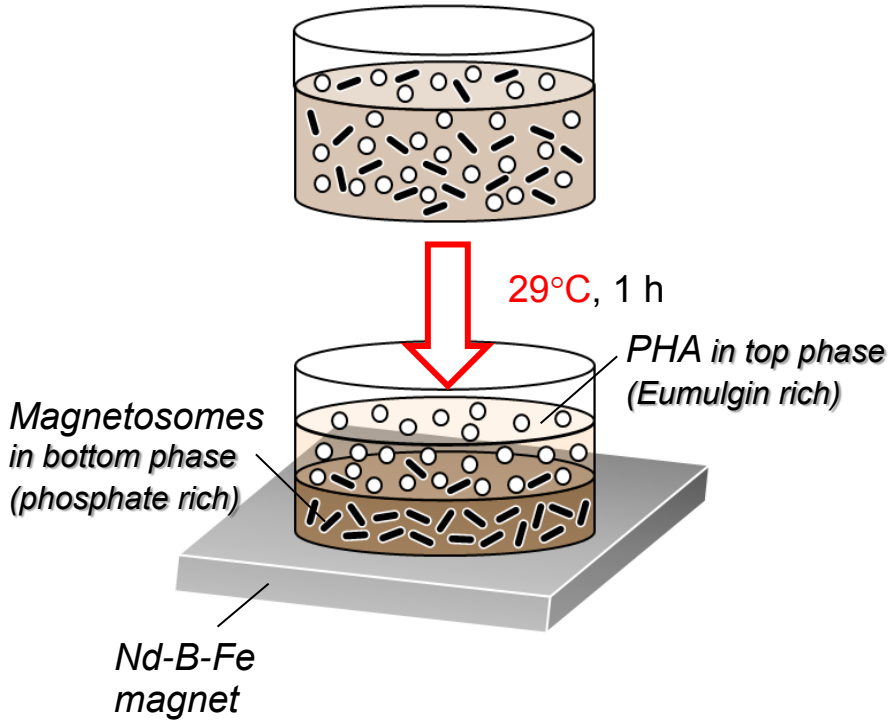

Figure 4.16. Schematic illustration of the magnetic micellar aqueous two-phase extraction approach used to separate magnetosomes from PHA.

4.4 Conclusions

The overarching aim of this chapter has been to advance a fully scalable platform for the production and purification of magnetosomes from *M. gryphiswaldense MSR-1* and, by

extension, other magnetotactic bacteria. The platform comprises the following linked steps: fermentation of the magnetotactic bacterium; centrifugal recovery of the cells; mechanical disruption to release the magnetosome chains; subsequent capture and partial purification of the magnetosomes in a 'rotor-stator' high-gradient magnetic separator; and finally, purification/polishing of the magnetosomes free of PHA granules using an aqueous micellar two-phase system we have employed previously for continuous magnetic particle based processing (Fischer et al. 2013). Specifically, we have shown that maximum cellular magnetism, long magnetosome chain lengths and lower PHA contents are favoured during the exponential phase of growth, and further that single pass disruption of such cells in an industrial high pressure homogenizer at moderate pressure ensures effective magnetosome release with minimal attritive damage. While the use of small commercial HGMS filter cartridges intended for lymphocytes separations is inappropriate for magnetosome purifications from unclarified cell disruptates, as magnetosome recovery is strongly compromised by trapped biomass, a 'state-of-art' rotor-stator HGMS proved effective for this task. Finally, we have demonstrated that a new scalable operation 'magnetically enhanced micellar aqueous two-phase extraction (Fischer et al., 2013), is a viable alternative to sucrose density gradient centrifugation for removing stubborn PHA granule impurities from magnetosome preparations. Even in its current unoptimized form the process was able to deliver a magnetosome yield of 45% whilst removing *ca.* 99% and >99% of the original PHA and protein contents. It is completely justified, because all of the unit operations in the process can be operated continuously, the two new operations HGMF and ATPS were designed to be continuous from outset.

CHAPTER 5

General Conclusions and future work

In this study we have developed flow cytometry (FCM) tools allowing the rapid analyses of cell physiology, morphology and polyhydroxyalkanoate (PHA) content of *Magnetospirillum gryphiswaldense* MSR-1. We used these new tools to optimise high efficiency biomass and magnetosome production by optimising the feed substances in fermentations. Finally, we developed methods for the extraction and purification of magnetosomes via a scalable process including homogenisation, high gradient magnetic separation and aqueous two-phase separation.

In Chapter 1, the current state of upstream and downstream processing of magnetosomes was reviewed. The lack of tools for monitoring cell physiology, morphology, PHA and free iron content during MSR-1 cultivation was addressed in Chapter 2 using FCM, allowing rapid monitoring of cell cultivation. This work simplifies measurement of fermentation parameters, in order to assess if cells are healthy, producing magnetosomes, and making PHA granules. This assessment is very important to guide the design and operation of fermentations, allowing harvest of cultures at relatively high biomass concentrations containing large numbers of magnetosomes but low PHA content, which can reduce the difficulty of the work in downstream processing. Further studies of the correlation between mean Phen Green fluorescence measured by FCM and quantitative iron measurements in liquid and solid phases within the cells should be calculated by mass balance, in order to determine if the iron taken from the substrate is being biomineralized quickly within cells.

L-lactic acid has been employed as both carbon source for cell growth and acid for pH adjustment in fermentation. Thus, in order to increase biomass yield from the substrate and reduce the production of PHA, the optimisation of the concentration of lactic acid in the feed solution has been studied. Since the feed both regulates pH and provides carbon source, this work was essential to ensure balanced control of pH and supply of nutrients supporting

growth. The C_{mag} values did not perfectly correlate to magnetosome production, especially when large amounts of PHA granules were produced, which changed the cell morphology. Thus, the measurement of intracellular solid iron, and not total ionic and solid iron, should be performed during the cell cultivation. This can be achieved quickly by using chemical lysis or probe sonication to disrupt cell samples efficiently before atomic absorption spectroscopy measurement.

The importance of nitrate concentration in the feed has also been studied. The magnetosome formation and denitrification in MSR-1 cells occur simultaneously under oxygen-limited conditions (Chapter 2), and the improvements of biomass and intracellular iron concentration have been achieved after employing nitrate in the feed solution. Clearly, the nitrate was consumed and ran out after 40 h in the fermentation experiments under microaerobic conditions. Thus, it is clear that further studies on the effects of low nitrate concentration during fermentation on magnetosome formation, and the impact of higher nitrate concentration on the accumulation of nitrite, are potentially interesting. Moreover, the influence of reducing power during magnetosome formation and cell growth should also be considered.

The purpose of the downstream processing in this study was to obtain pure magnetosomes while maintaining their chain configuration. Thus, the scalable downstream processing techniques for magnetosome extraction and purification started with optimising fermentation and cell harvest time. Next, cell disruption was optimised to allow high disruption efficiency but low damage of magnetosome chain configuration. But chain breakage by the shear force from the rotor-stator magnetic separator and by the detergents from aqueous two-phase separation should also be characterised in the future. The cell disruption graphs did not standardise a first order disruption model, because three different pressures on cell

disruption is not available to present a precise linear relationship between disruption pressure against release by Hetherington's relationship (Hetherington et al., 1971). Thus, more disruption pressures of cell disruption with Constant System Cell Disruptor (CSCD) should be investigated. The purity of purified magnetosomes should also be studied. Polyacrylamide gel electrophoresis (PAGE) or polymerase chain reaction (PCR) amplification can be used for DNA and RNA detection. Tachypleus amebocyte lysate (TAL) can be employed to measure endotoxin concentrations.

In the future, the process for functionalization of purified magnetosomes with different ligands such as 4-mercaptothylpyridine hydrochloride (4-MEP HCl), equine chorionic gonadotropin specific antibodies (anti-eCG) and protein A should be studied for immunoglobulin and glycoprotein purifications (Gomes et al., 2018; Müller et al., 2015). Given the large specific surface area, the application of magnetosome adsorbents is very promising.

CHAPER 6

Appendix

6.1 Correlation of cell concentration to OD_{565}

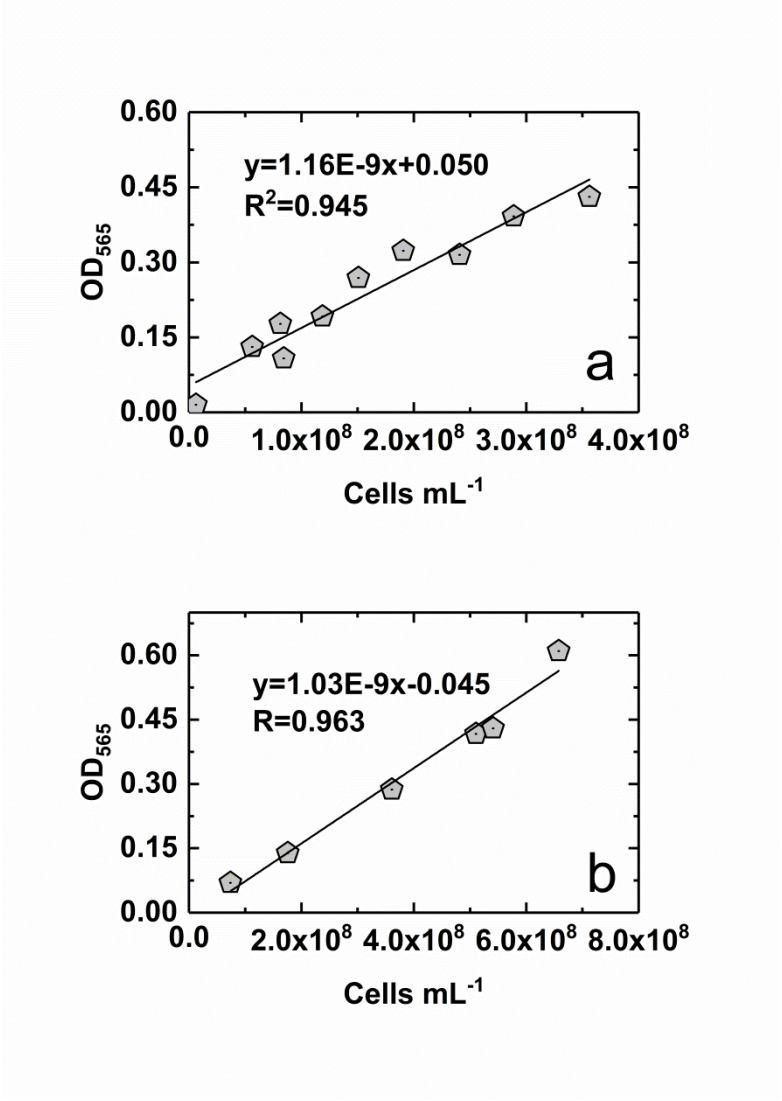

Figure 6.1. Correlation between culture OD565 and cells mL-1 measured using FCM. (a) Non-stained cells (b) cells stained with Syto62.

6.2 Influence of oxygen and iron limitation on PHA production

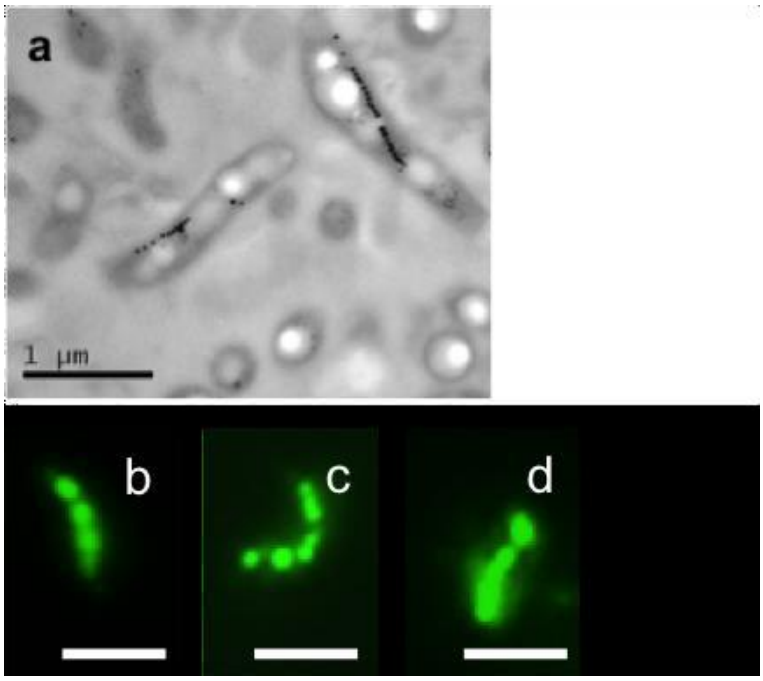

Figure 6.2. (a) TEM micrograph of *M. gryphiswaldense* MSR-1 cells harvested from an O2-limited bioreactor. Note the magnetosome chains (black) and PHA aggregates (white globules). Fluorescence images of Pyr-546 stained MSR-1 cells: (b) harvested from an O_2-limited bioreactor and after 48 h growth on (c) FSM and (d) FSM-Fe^{-} medium. The scale bars indicate a length of 2.5 µm. For the preparations of samples for TEM and TEM imaging, the reader is referred to Chapter 3 (3.2.4.4) and 4 (4.2.8).

6.3 Comparison of fluorescence microscopy and TEM images of magnetic cells during shift to aerobic conditions.

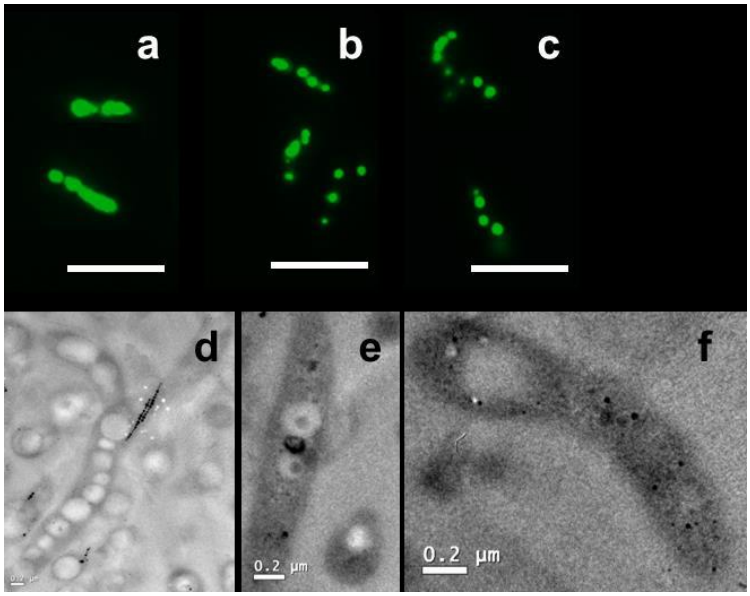

Figure 6.3. Comparison of fluorescence microscopy and TEM images of magnetic cells during shift to aerobic conditions. MSR-1 cells grown under O_2-limited conditions in a bioreactor were transferred to O_2-sufficient conditions with either iron-containing (FSM) or iron-lacking (FSM-Fe^-) media. Fluorescence images of Pyr-546 stained MSR-1 cells: (a) harvested from an O_2-limited bioreactor and after 48 h growth on (b) FSM and (c) FSM-Fe^- medium; the scale bars indicate a length of 5 µm. TEM micrographs of MSR-1 cells: (d) harvested from an O_2-limited bioreactor and after 48 h growth on (e) FSM and (f) FSM-Fe^- medium. For the preparations of samples for TEM and TEM imaging, the reader is referred to Chapter 3 (3.2.4.4) and 4 (4.2.8).

6.4 A representative pH-stat fermentation

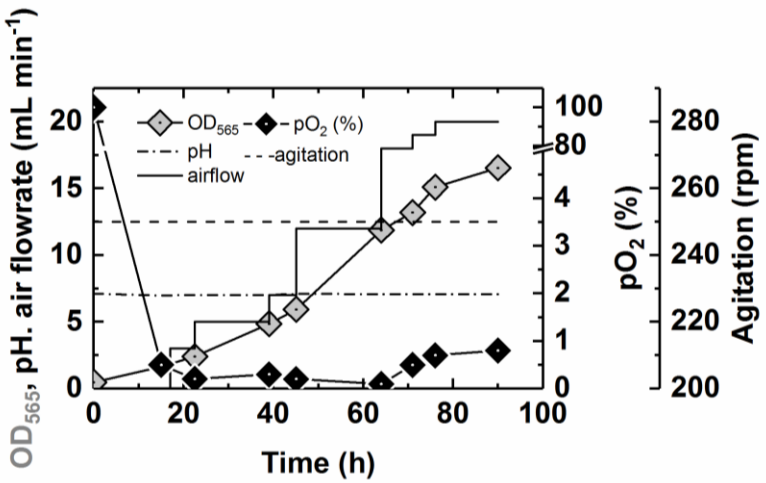

Figure 6.4. A representative pH-stat fermentation. MSR-1 was grown in FSM medium with a feed comprising 100 g L^{-1} lactic acid and 25 g L^{-1} sodium nitrate. Other parameters as explained in Results and Discussion and Materials and Methods sections.

6.5 Biomass production in relation to feed volume from different concentration of carbon source

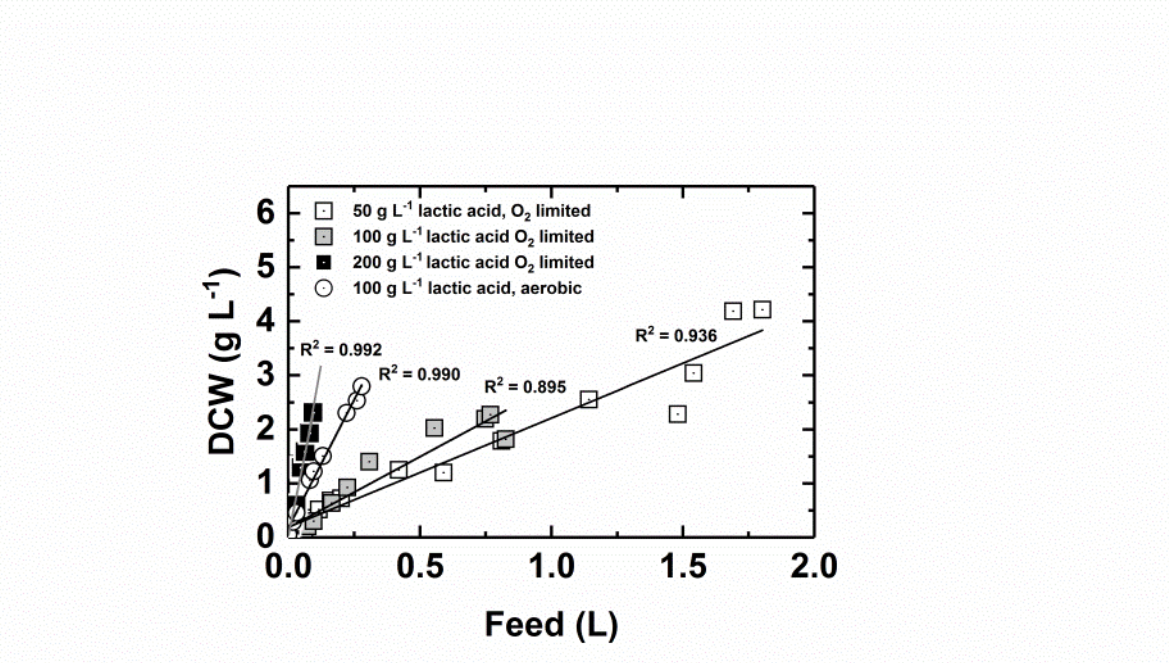

Figure 6.5. Correlation between feed volume supplied and biomass concentration. Oxygen-limited cultures with feed lactic acid concentrations of 50 g L^{-1} (white squares), 100 g L^{-1} (gray squares), and 200 g L^{-1} (black squares); aerobic culture with feed lactic acid concentration of 100 g L^{-1} (white circles).

6.6 Fluorescence intensity of samples with different concentration of carbon source at different time of cultivation

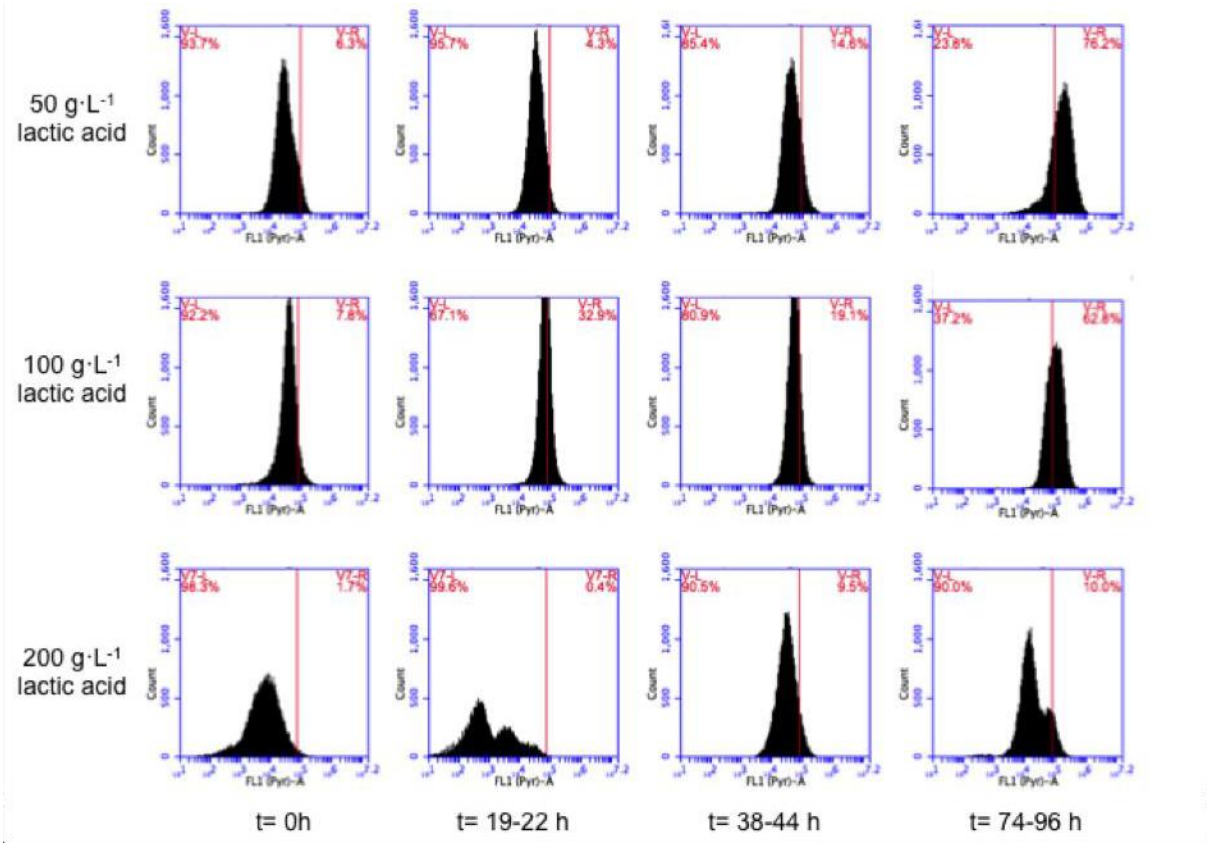

Figure 6.6. Fluorescence intensity histograms of samples collected at 0 h (start of fermentations), 19–22 h, 38–44 h or 74–96 h (end of fermentation) of oxygen-limited cultures containing 50, 100 or 200 g L^{-1} lactic acid in the feeding solution.

6.7 FCM and C_{mag} analyses with cultivations in different nitrate concentration

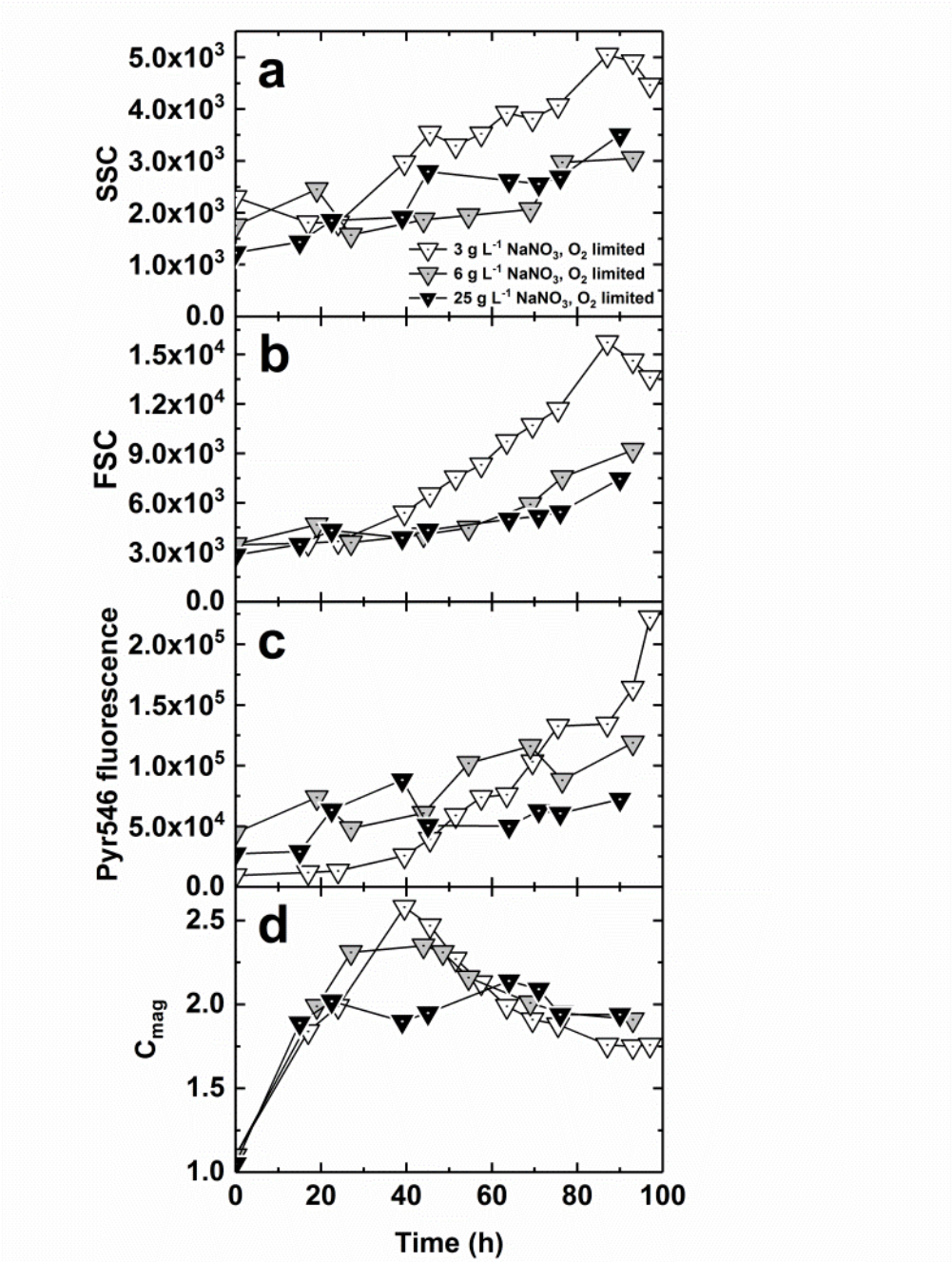

Figure 6.7. FCM and C_{mag} analysis of cells grown with different feed sodium nitrate concentrations. Plots show side scatter, SSC (a), forward scatter, FSC (b); fluorescence of Pyr546-stained cells (c), and C_{mag} values (d) plotted against time. For FCM 25,000 data points were collected for each sample and mean values are represented. Symbols: oxygen-limited pH-stat cultures with feed $NaNO_3$ concentrations of 3 g L^{-1} (white down-triangles), 6 g L^{-1} (gray down-triangles) and 25 g L^{-1} (black down-triangles).

6.8 Protein curve calibration for analyses in Chapter 4

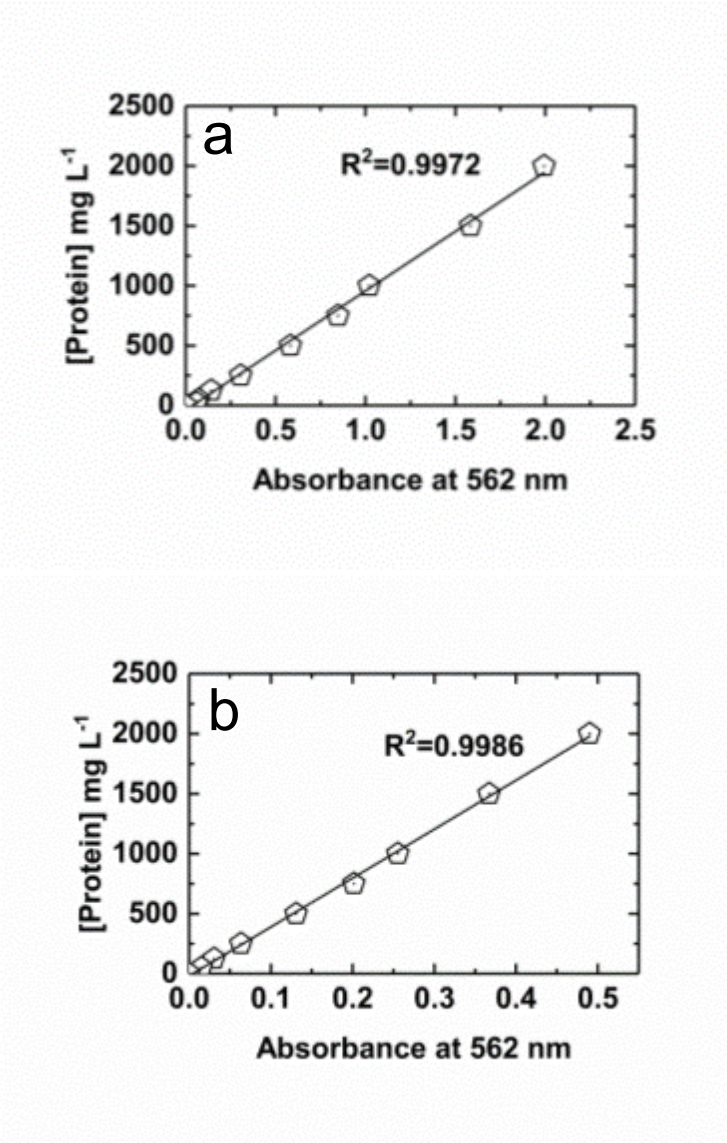

Figure 6.8. Calibration curves used for calculation of protein concentration with BCA assay at 562 nm. (a) Soluble protein calibration curve, (b) whole protein calibration curve.

6.9 TEM images of disruptions with CSCD

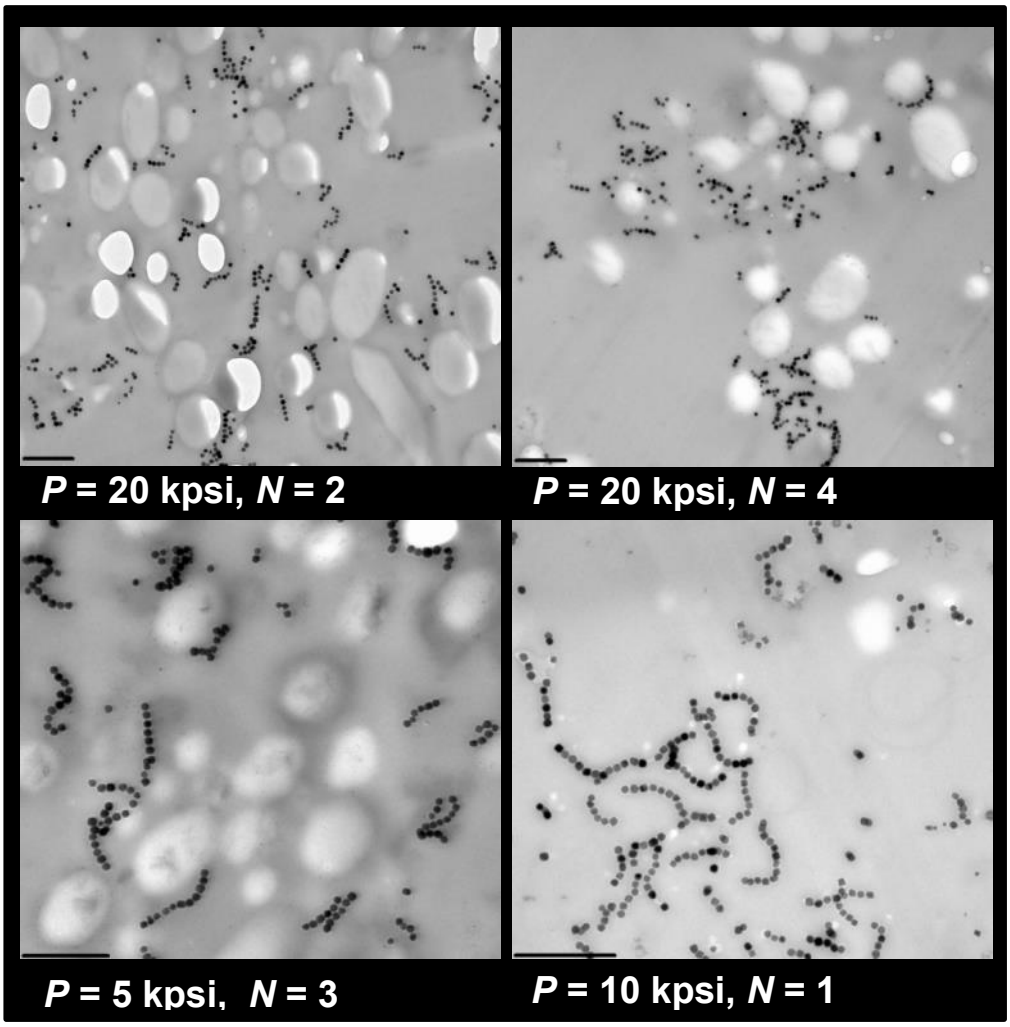

Figure 6.9. TEM images following disruption of stationary phase *M. gryphiswaldense* MSR-1 cells in the CSCD using different combinations of *P* and *N*.

6.10 Normalised magnetosome release from stationary phase cells

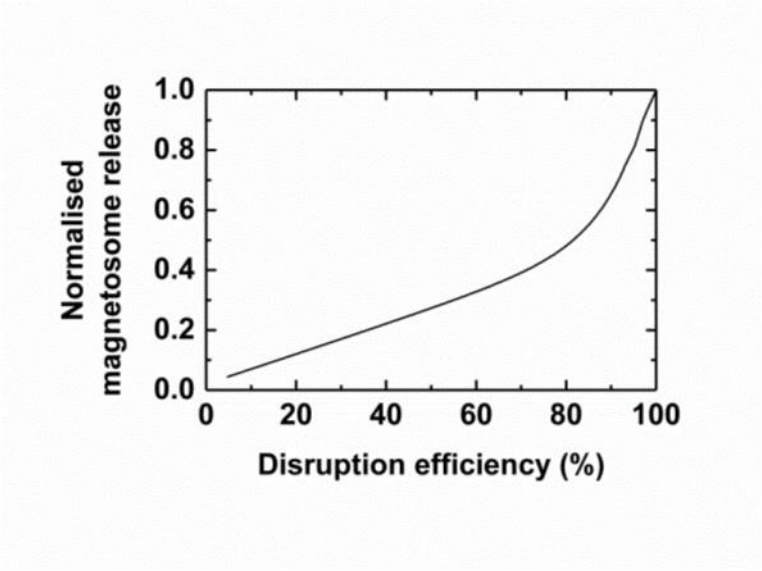

Figure 6.10. Normalised magnetosome release from stationary phase *M. gryphiswaldense* MSR-1 cells vs. disruption efficiency. Normalising the fitted iron release curve by the protein release curve provides a measure of the ease with which magnetosomes escape *cf.* protein. Maximum iron and protein release values of 9.11 and 352.77 mg g^{-1} DCW respectively were determined by extrapolating the fit curves to 100% disruption efficiency. The curve demonstrates that the ease of magnetosome release increases linearly from 5 to 70% disruption efficiency (reaching 40% of the protein release) and exponentially thereafter to equivalence (i.e. 1.0) at 100% disruption efficiency.

6.11 Continuous magnetic extraction system

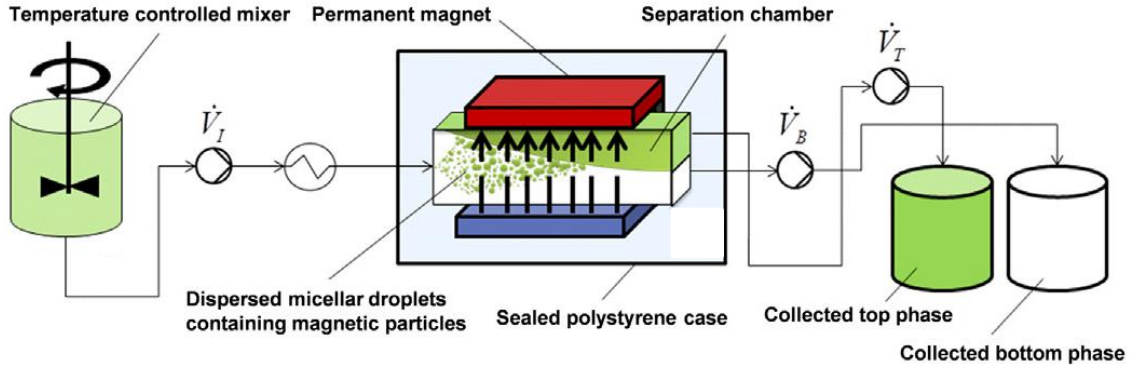

Figure 6.11. Schematic illustration of the continuous magnetic extraction process and the component part (Fischer et al., 2013).

A suspension containing magnetic adsorbents and *E. coli* extract is mixed well in a temperature contolled tank. Then the suspension is pumped into the separation chamber with a constant feed rate. After the phase separation, the top phase and the bottom phase are collected separately into different containers. In this separation system, magnetic particles are collected in the top phase, and the soluble proteins from *E. coli* extract are maintained in the bottom phase.

CHAPTER 7

References

Ali, I., Peng, C., Khan, Z.M., Naz, I., 2017. Yield cultivation of magnetotactic bacteria and magnetosomes: A review. *J. Basic Microbiol.* 57: 1-10.

Ali, I., Peng, C., Khan, Z.M., Naz, I., Sultan, M., 2018. An overview of heavy metal removal from wastewater using magnetotactic bacteria. *J. Chem. Technol. Biotechnol.* 93: 2817–2832. https://doi.org/10.1002/jctb.5648

Alphandéry, E., 2014. Applications of magnetosomes synthesized by magnetotactic bacteria in medicine. *Front. Bioeng. Biotechnol.* 2: 5.

Alphandéry, E., Ding, Y., Ngo, a. T., Wang, Z.L., Wu, L.F., Pileni, M.P., 2009. Assemblies of aligned magnetotactic bacteria and extracted magnetosomes: What is the main factor responsible for the magnetic anisotropy? *ACS Nano.* 3: 1539–1547.

Alphandéry, E., Faure, S., Raison, L., Duguet, E., Howse, P.A., Bazylinski, D.A., 2011a. Heat production by bacterial magnetosomes exposed to an oscillating magnetic field. *J. Phys. Chem. C* 115: 18–22.

Alphandéry, E., Faure, S., Seksek, O., Guyot, F., Chebbi, I., 2011b. Chains of magnetosomes extracted from AMB-1 magnetotactic bacteria for application in alternative magnetic field cancer therapy. *ACS Nano.* 5: 6279–6296.

Alphandéry, E., Guyot, F., Chebbi, I., 2012. Preparation of chains of magnetosomes, isolated from Magnetospirillum magneticum strain AMB-1 magnetotactic bacteria, yielding efficient treatment of tumors using magnetic hyperthermia. *Int. J. Pharm.* 434: 444–452.

Arakaki, A., Nakazawa, H., Nemoto, M., Mori, T., Matsunaga, T., 2008. Formation of magnetite by bacteria and its application. *J. R. Soc. Interface* 5: 977–999.

Bakhshi, P.K., Bain, J., Gul, M.O., Stride, E., Edirisinghe, M., Staniland, S.S., 2016. Manufacturing man-made magnetosomes: High-throughput *in situ* synthesis of biomimetic magnetite loaded

nanovesicles. *Macromol. Biosci.* 16: 1555-1561.

Ban, J., Jiang, W., Li, Y., Zhang, Y.P., Li, J.L., 2010. Functional analysis of hydrogenases and their effects on cell growth and magnetosome synthesis in *Magnetospirillum gryphiswaldense*. *Chinese Sci. Bull.* 55: 1271–1277.

Bañuelos Prieto, J., López Arbeloa, F., Martínez Martínez, V., López Arbeloa, I., 2004. Theoretical study of the ground and excited electronic states of pyrromethene 546 laser dye and related compounds. *Chem. Phys.* 296: 13–22.

Barber-Zucker, S., Zarivach, R., 2017. A look into the biochemistry of Magnetosome biosynthesis in magnetotactic bacteria. *ACS Chem. Biol.* 12: 13-22.

Baumgartner, J., Bertinetti, L., Widdrat, M., Hirt, A.M., Faivre, D., 2013. Formation of magnetite nanoparticles at low temperature: From superparamagnetic to stable single domain particles. *PLoS One.* 8: e57070.

Bazylinski, D.A., Frankel, R.B., 2004. Magnetosome formation in prokaryotes. *Nat. Rev. Microbiol.* 2: 217-230.

Bazylinski, D.A., Garratt-Reed, A.J., Frankel, R.B., 1994. Electron microscopic studies of magnetosomes in magnetotactic bacteria. *Microsc. Res. Tech.* 27: 389-401.

Bazylinski, D.A., Schübbe, S., 2007. Controlled biomineralization by and applications of magnetotactic bacteria. *Adv. Appl. Microbiol.* 62: 21-62.

Bazylinski, D.A., Wiliams, T., 2006. Ecophysiology of Magnetotactic Bacteria, in: Schüler, D., (Eds.). *Magnetoreception and Magnetosomes in Bacteria.* Berlin: Springer, pp. 37-75.

Bazylinski, D. a, Frankel, R.B., 2004. Magnetosome formation in prokaryotes. *Nat. Rev. Microbiol.* 2: 217–230.

Bechstein, D.J.B., Lee, J.R., Ooi, C.C., Gani, A.W., Kim, K., Wilson, R.J., Wang, S.X., 2015. High performance wash-free magnetic bioassays through microfluidically enhanced particle specificity. *Sci. Rep.* 5: 11693.

Bird, S.M., Galloway, J.M., Rawlings, A.E., Bramble, J.P., Staniland, S.S., 2015. Taking a hard line with biotemplating: Cobalt-doped magnetite magnetic nanoparticle arrays. *Nanoscale.* 7: 7340-51.

Blakemore, R., 1975. Magnetotactic bacteria. *Science.* 190: 377–379.

Blakemore, R.P., Frankel, R.B., 1981. Magnetic navigation in bacteria. *Sci. Am.* 245: 58-65.

Blakemore, R.P., Maratea, D., Wolfe, R.S., 1979. Isolation and pure culture of a freshwater magnetic spirillum in chemically defined medium. *J. Bacteriol.* 140: 720-729.

Borg, S., Rothenstein, D., Bill, J., Schüler, D., 2015. Generation of multishell magnetic hybrid nanoparticles by encapsulation of genetically engineered and fluorescent bacterial magnetosomes with ZnO and SiO_2. *Small*. 11: 4209–4217.

Borlido, L., Moura, L., Azevedo, A.M., Roque, A.C.A., Aires-Barros, M.R., Farinha, J.P.S., 2013. Stimuli-responsive magnetic nanoparticles for monoclonal antibody purification. *Biotechnol. J.* 8: 709-717.

Boucher, M., Geffroy, F., Prévéral, S., Bellanger, L., Selingue, E., Adryanczyk-Perrier, G., Péan, M., Lefèvre, C.T., Pignol, D., Ginet, N., Mériaux, S., 2017. Genetically tailored magnetosomes used as MRI probe for molecular imaging of brain tumor. *Biomaterials.* 121: 167-178.

Bresan, S., Sznajder, A., Hauf, W., Forchhammer, K., Pfeiffer, D., Jendrossek, D., 2016. Polyhydroxyalkanoate (PHA) granules have no phospholipids. *Sci. Rep.* 6: 26612.

Brown, G.N., Müller, C., Theodosiou, E., Franzreb, M., Thomas, O.R.T., 2013. Multi-cycle recovery of lactoferrin and lactoperoxidase from crude whey using fimbriated high-capacity magnetic cation exchangers and a novel “rotor-stator” high-gradient magnetic separator. *Biotechnol.*

Bioeng. 110: 1714–1725.

Brusentsov, N.A., Gogosov, V. V., Brusentsova, T.N., Sergeev, A. V., Jurchenko, N.Y., Kuznetsov, A.A., Kuznetsov, O.A., Shumakov, L.I., 2001. Evaluation of ferromagnetic fluids and suspensions for the site-specific radiofrequency-induced hyperthermia of MX11 sarcoma cells *in vitro*. *J. Magn. Magn. Mater.*225: 113-117.

Cai, F., Li, J., Sun, J., Ji, Y., 2011. Biosynthesis of gold nanoparticles by biosorption using *Magnetospirillum gryphiswaldense* MSR-1. *Chem. Eng. J.* 175: 70-75.

Cao, P., Müller, T.K.H., Ketterer, B., Ewert, S., Theodosiou, E., Thomas, O.R.T., Franzreb, M., 2015. Integrated system for temperature-controlled fast protein liquid chromatography. II. Optimized adsorbents and "single column continuous operation." *J. Chromatogr. A.* 1403: 118-131.

Cao, Y., Bai, G., Chen, J., Tian, W., Wang, S., Yang, W., 2006. Preparation and characterization of magnetic microspheres for the purification of interferon alpha-2b. *J. Chromatogr. B. Analyt. Technol. Biomed. Life Sci.* 833: 236-244.

Cao, Y., Tian, W., Gao, S., Yu, Y., Yang, W., Bai, G., 2007. Immobilization staphylococcal protein A on magnetic cellulose microspheres for IgG affinity purification. *Immobil. Biotechnol.* 35: 467-480.

Chen, C., Wang, S., Li, L., Wang, P., Chen, C., Sun, Z., Song, T., 2016. Bacterial magnetic nanoparticles for photothermal therapy of cancer under the guidance of MRI. *Biomaterials*. 104: 352–360.

Chen, C.Y., Chen, C.F., Yi, Y., Chen, L.J., Wu, L.F., Song, T., 2014. Construction of a microrobot system using magnetotactic bacteria for the separation of *Staphylococcus aureus*. *Biomed. Microdevices.* 16: 761-70.

Dasdag, S., 2014. Magnetotactic bacteria and their application in medicine. *J. Phys. Chem. Biophys.* 4: 141.

Day, J.P., Kell, D.B., Griffith, G.W., 2002. Differentiation of phytophthora infestans sporangia from

other airborne biological particles by flow cytometry. *Appl. Environ. Microbiol.* 68: 37-45.

Divyashree, M.S., Shamala, T.R., Rastogi, N.K., 2009. Isolation of polyhydroxyalkanoate from hydrolyzed cells of Bacillus flexus using aqueous two-phase system containing polyethylene glycol and phosphate. *Biotechnol. Bioprocess Eng.* 14: 482–489.

Dunnill, P., Lilly, M.D., 1974. Purification of enzymes using magnetic bio-affinity materials. *Biotechnol. Bioeng.* 16: 987–990.

Faivre, D., Menguy, N., Pósfai, M., Schüler, D., 2008. Environmental parameters affect the physical properties of fast-growing magnetosomes. *Am. Mineral.* 13: 1700448.

Felfoul, O., Mohammadi, M., Taherkhani, S., De Lanauze, D., Zhong Xu, Y., Loghin, D., Essa, S., Jancik, S., Houle, D., Lafleur, M., Gaboury, L., Tabrizian, M., Kaou, N., Atkin, M., Vuong, T., Batist, G., Beauchemin, N., Radzioch, D., Martel, S., 2016. Magneto-aerotactic bacteria deliver drug-containing nanoliposomes to tumour hypoxic regions. *Nat. Nanotechnol.* 11: 941-947.

Fernandez-Castane, A., Li, H., Thomas, O.R.T., Overton, T.W., 2018. Development of a simple intensified fermentation strategy for growth of *Magnetospirillum gryphiswaldense* MSR-1: physiological responses to changing environmental conditions. *N. Biotechnol.* 46: 22–30.

Fernández-Castané, A., Li, H., Thomas, O.R.T., Overton, T.W., 2017. Flow cytometry as a rapid analytical tool to determine physiological responses to changing O_2 and iron concentration by *Magnetospirillum gryphiswaldense* strain MSR-1. *Sci. Rep.* 7: 1–11.

Fischer, H., Mastrogiacomo, G., Löffler, J.F., Warthmann, R.J., Weidler, P.G., Gehring, A.U., 2008. Ferromagnetic resonance and magnetic characteristics of intact magnetosome chains in *Magnetospirillum gryphiswaldense*. *Earth Planet. Sci. Lett.* 270: 200-208.

Fischer, I., Franzreb, M., 2011. Direct determination of the composition of aqueous micellar two-phase systems (AMTPS) using potentiometric titration-A rapid tool for detergent-based

bioseparation. *Colloids and Surface A: Physicochem. Eng. Asp.* 377: 97–102.

Fischer, I., Hsu, C.-C., Gärtner, M., Müller, C., Overton, T.W., Thomas, O.R. T., Franzreb, M., 2013. Continuous protein purification using functionalized magnetic nanoparticles in aqueous micellar two-phase systems. *J. Chromatogr. A*. 1305: 7–16.

Flies, C.B., Peplies, J., Schüler, D., 2005. Combined approach for characterization of uncultivated magnetotactic bacteria from various aquatic environments. *Appl. Environ. Microbiol.* 71: 2723-2731.

Frankel, R.B., 1984. Magnetic guidance of organisms. Annu. Rev. *Biophys. Bioeng.* 13: 85-103.

Frankel, R.B., Blakemore, R.P., Wolfe, R.S., 1979. Magnetite in freshwater magnetotactic bacteria. *Science.* 203: 1355–6.

Frankel, R.B., Papaefthymiou, G.C., Blakemore, R.P., O'Brien, W., 1983. Fe_3O_4 precipitation in magnetotactic bacteria. *BBA - Mol. Cell Res.* 763: 147–159.

Franzreb, M. 2003. Magnettechnologie in der Verfahrenstechnik wässriger Medien. Thesis (PhD), Karlsruher Institut Für Technologie.

Franzreb, M., Siemann-Herzberg, M., Hobley, T.J., Thomas, O.R.T., 2006. Protein purification using magnetic adsorbent particles. *Appl. Microbiol. Biotechnol.* 70: 505–516.

French, C., Keshavarz-Moore, E., Ward, J.M., 1996. Development of a simple method for the recovery of recombinant proteins from the *Escherichia coli* periplasm. *Enzyme Microb. Technol.* 19: 332–338.

Frey, N.A., Peng, S., Cheng, K., Sun, S., 2009. Magnetic nanoparticles: Synthesis, functionalization, and applications in bioimaging and magnetic energy storage. *Chem. Soc. Rev.* 38: 2532-2542.

Galloway, J.M., Bramble, J.P., Staniland, S.S., 2013. Biomimetic synthesis of materials for technology.

Chem. A. Eur. J. 19: 8710-8725.

García-Torreiro, M., Lu-Chau, T.A., Lema, J.M., 2016. Effect of nitrogen and/or oxygen concentration on poly(3-hydroxybutyrate) accumulation by *Halomonas boliviensis*. *Bioprocess Biosyst. Eng.* 39: 1365–1374.

Geng, J., Beloin, C., Ghigo, J.M., Henry, N., 2014. Bacteria hold their breath upon surface contact as shown in a strain of *Escherichia coli*, using dispersed surfaces and flow cytometry analysis. *PLoS One.* 9: e102049.

George, M.W., Romas, J.K., Lee, J., 1983. Magnetic separations in biotechnology. *Trends Biotechnol.* 1: 144–148.

Ginet, N., Pardoux, R., Adryanczyk, G., Garcia, D., Brutesco, C., Pignol, D., 2011. Single-step production of a recyclable nanobiocatalyst for organophosphate pesticides biodegradation using functionalized bacterial magnetosomes. *PLoS One*. 6: 4–10.

Gomes, C., 2006. Advances in high-gradient magnetic fishing for bioprocessing. Thesis (PhD). Technical University of Denmark.

Gomes, C.S.G., Fashina, A., Fernández-Castané, A., Overton, T.W., Hobley, T.J., Theodosiou, E., Thomas, O.R.T., 2018. Magnetic hydrophobic-charge induction adsorbents for the recovery of immunoglobulins from antiserum feedstocks by high-gradient magnetic fishing. *J. Chem. Technol. Biotechnol.* 93: 1901–1915.

Gorby, Y. a., Beveridge, T.J., Blakemore, R.P., 1988. Characterization of the bacterial magnetosome membrane. *J. Bacteriol.* 170: 834–841.

Große, C., Scherer, J., Koch, D., Otto, M., Taudte, N., Grass, G., 2006. A new ferrous iron-uptake transporter, EfeU (YcdN), from *Escherichia coli*. *Mol. Microbiol.* 62: 120-131.

Grünberg, K., Müller, E.C., Otto, A., Reszka, R., Linder, D., Kube, M., Reinhardt, R., Schüler, D., 2004.

Biochemical and proteomic analysis of the magnetosome membrane in *Magnetospirillum gryphiswaldense*. *Appl. Environ. Microbiol.* 70: 1040–1050.

Grünberg, K., Wawer, C., Tebo, B.M., Schuler, D., 2001. A large gene cluster encoding several magnetosome proteins is conserved in different species of magnetotactic bacteria. *Appl. Environ. Microbiol.* 67: 4573–4582.

Grzenia, D.L., Carlson, J.O., Wickramasinghe, S.R., 2008. Tangential flow filtration for virus purification. *J. Memb. Sci.* 67: 4573-4582.

Gu, J.L., Tong, H.F., Lin, D.Q., 2016. Evaluation of magnetic particles modified with a hydrophobic charge-induction ligand for antibody capture. *J. Chromatogr. A*. 1460: 61–67.

Guo, F., Liu, Y., Chen, Y., Tang, T., Jiang, W., Li, Y., Li, J., 2011. A novel rapid and continuous procedure for large-scale purification of magnetosomes from *Magnetospirillum gryphiswaldense*. *Appl. Microbiol. Biotechnol.* 90: 1277–1283.

Halling, P.J., Dunnill, P., 1980. Magnetic supports for immobilized enzymes and bioaffinity adsorbents. *Enzyme Microb. Technol.* 2:2-10.

Hamdous, Y., Chebbi, I., Mandawala, C., Le Fèvre, R., Guyot, F., Seksek, O., Alphandéry, E., 2017. Biocompatible coated magnetosome minerals with various organization and cellular interaction properties induce cytotoxicity towards RG-2 and GL-261 glioma cells in the presence of an alternating magnetic field. *J. Nanobiotechnology.* 15: 74.

Hausmann, R., Hoffmann, C., Franzreb, M., Höll, W.H., 2000. Mass transfer rates in a liquid magnetically stabilized fluidized bed of magnetic ion-exchange particles. *Chem. Eng. Sci.* 55: 1477–1482.

Heebøll-Nielsen, A., Dalkiær, M., Hubbuch, J.J., Thomas, O.R.T., 2004a. Superparamagnetic adsorbents for high-gradient magnetic fishing of lectins out of legume extracts. *Biotechnol.*

Bioeng. 87: 311–323.

Heebøll-Nielsen, A., Justesen, S.F.L., Hobley, T.J., Thomas, O.R.T., 2004b. Superparamagnetic cation–exchange adsorbents for bioproduct recovery from crude process liquors by high-gradient magnetic fishing. *Sep. Sci. Technol.* 39: 2891–2914.

Hetherington, P.J., Follows, M., Dunnill, P., Lilly, M.D., 1971. Release of protein from baker's yeast (*Saccharomyces cerevisiae*) by disruption in an industrial homogeniser. *Trans. Instn. Chem. Engrs.* 49: 142-148.

Hettwer, D., Wang, H., 1989. Protein release from *Escherichia coli* cells permeabilized with guanidine-HCl and triton X100. *Biotechnol. Bioeng.* 33: 886–895.

Heyen, U., Schüler, D., 2003. Growth and magnetosome formation by microaerophilic Magnetospirillum strains in an oxygen-controlled fermentor. *Appl. Microbiol. Biotechnol.* 61: 536–544.

Heywood, B.R., Bazylinski, D.A., Garratt-Reed, A., Mann, S., Frankel, R.B., 1990. Controlled biosynthesis of greigite (Fe_3S_4) in magnetotactic bacteria. *Naturwissenschaften.* 77: 536-538.

Hirschbein, B., Brown, D., Whitesides, G., 1982. Magnetic separations in chemistry and biochemistry. *Chemtech*. 12: 172–179.

Holschuh, K., Schwämmle, A., 2005. Preparative purification of antibodies with protein A - An alternative to conventional chromatography. *Journal of Magnetism and Magnetic Materials.* 293: 345-348.

Hubbuch, J.J., 2002. Development of adsorptive separation system for recovery of proteins from crude bioprocess liquors. Thesis (PhD). Technical University of Denmark.

Hubbuch, J.J., Matthiesen, D.B., Hobley, T.J., Thomas, O.R., 2001. High gradient magnetic separation versus expanded bed adsorption: a first principle comparison. *Bioseparation*. 10: 99–112.

Hubbuch, J.J., Thomas, O.R.T., 2002. High-gradient magnetic affinity separation of trypsin from porcine pancreatin. *Biotechnol. Bioeng.* 79: 301–313.

Hughes, D.E., Wimpenny, J.W.T., Lloyd, D., 1971. The disintegration of micro-organisms. *Methods in Microbiology.* 5:1-54.

Jacob, J.J., Suthindhiran, K., 2016. Magnetotactic bacteria and magnetosomes – Scope and challenges. *Mater. Sci. Eng. C.* 68:919-928.

Jendrossek, D., Pfeiffer, D., 2014. New insights in the formation of polyhydroxyalkanoate granules (carbonosomes) and novel functions of poly(3-hydroxybutyrate). *Environ. Microbiol.* 16: 2357–2373.

Kacmar, J., Carlson, R., Balogh, S.J., Srienc, F., 2006. Staining and quantification of poly-3-hydroxybutyrate in *Saccharomyces cerevisiae* and *Cupriavidus necator* cell populations using automated flow cytometry. *Cytometry A.* 69: 27-35.

Karmann, S., Panke, S., Zinn, M., 2017. The bistable behaviour of *Pseudomonas putida* KT2440 during PHA depolymerization under carbon limitation. *Bioengineering.* 4: 58.

Karnchanasri, K., 2013. Bi-layered chromatography matrices for the purification of biological nanoplexes. Thesis (PhD), University of Birmingham.

Katzmann, E., Eibauer, M., Lin, W., Pan, Y., Plitzko, J.M., Schüler, D., 2013. Analysis of magnetosome chains in magnetotactic bacteria by magnetic measurements and automated image analysis of electron micrographs. *Appl. Environ. Microbiol.* 79: 7755–7762.

Katzmann, E., Scheffel, A., Gruska, M., Plitzko, J.M., Schüler, D., 2010. Loss of the actin-like protein MamK has pleiotropic effects on magnetosome formation and chain assembly in Magnetospirillum gryphiswaldense. *Mol. Microbiol.* 77: 208-224.

Kessler, B., Witholt, B., 2001. Factors involved in the regulatory network of polyhydroxyalkanoate

metabolism. *J. Biotechnol.* 86: 97-104.

Klumpp, S., Faivre, D., 2012. Interplay of magnetic interactions and active movements in the formation of magnetosome chains. *PLoS One.* 7: e33562.

Kobayashi, A., Kirschvink, J.L., Nash, C.Z., Kopp, R.E., Sauer, D. a., Bertani, L.E., Voorhout, W.F., Taguchi, T., 2006. Experimental observation of magnetosome chain collapse in magnetotactic bacteria: Sedimentological, paleomagnetic, and evolutionary implications. *Earth Planet. Sci. Lett.* 245: 538–550.

Komeili, A., Li, Z., Newman, D.K., Jensen, G.J., 2006. Magnetosomes are cell membrane imaginations organized by the actin-like protein MamK. *Science.* 311: 242-245.

Lagendijk, E.L., Validov, S., Lamers, G.E.M., De Weert, S., Bloemberg, G. V., 2010. Genetic tools for tagging Gram-negative bacteria with mCherry for visualization in vitro and in natural habitats, biofilm and pathogenicity studies. *FEMS Microbiol. Lett.* 305: 81-90.

Lang, C., 2009. Magnetosome-specific expression of chimeric proteins in *Magnetospirillum gryphiswaldense* for applications in cell biology and biotechnology. Thesis (PhD): Ludwig-Maximilians-Universität München.

Lang, C., Pollithy, A., Schuler, D., 2009. Identification of promoters for efficient gene expression in *Magnetospirillum gryphiswaldense*. *Appl. Environ. Microbiol.* 75: 4206-10.

Lang, C., Schüler, D., 2008. Expression of green fluorescent protein fused to magnetosome proteins in microaerophilic magnetotactic bacteria. *Appl. Environ. Microbiol.* 74: 4944–4953.

Lang, C., Schüler, D., 2006. Biogenic nanoparticles: production, characterization, and application of bacterial magnetosomes. *J. Phys. Condens. Matter*. 18: S2815–S2828.

Laurent, S., Forge, D., Port, M., Roch, A., Robic, C., Vander Elst, L., Muller, R.N., 2008. Magnetic iron oxide nanoparticles: Synthesis, stabilization, vectorization, physicochemical characterizations

and biological applications. *Chem. Rev.* 108: 2064-2110.

Lee, M.Y., Lufkin, T., 2012. Development of the “three-step macs”: A novel strategy for isolating rare cell populations in the absence of known cell surface markers from complex animal tissue. *J. Biomol. Tech.* 23: 69–77.

Lee, S., Ahn, J.H., Choi, H., Seo, J.M., Cho, D., Koo, K., 2015. Natural magnetic nanoparticle containing droplet for smart drug delivery and heat treatment. *Conference of the IEEE Engineering in Medicine and Biology Society*. 2015: 3541-3544.

Lee, Y.H., Chen, S. Y., Wiesner, R.J., Huang, Y. F., 2004. Simple flow cytometric method used to assess lipid accumulation in fat cells. *J. Lipid Res.* 45: 1162-1167.

Lefèvre, C.T., Abreu, F., Lins, U., Bazylinski, D.A., 2011. A Bacterial Backbone: Magnetosomes in Magnetotactic Bacteria, in: Rai, M., Duran, N., (Eds.). *Metal Nanoparticles in Microbiology*. Berlin:Springer, pp. 75–102.

Lefèvre, C.T., Song, T., Yonnet, J.-P., Wu, L.-F., 2009. Characterization of bacterial magnetotactic behaviors by using a magnetospectrophotometry assay. *Appl. Environ. Microbiol.* 75: 3835–3841.

Li, J., Cai, F., Lv, H., Sun, J., 2013. Selective competitive biosorption of Au(III) and Cu(II) in binary systems by *Magnetospirillum gryphiswaldense*. *Sep. Sci. Technol.* 48: 960-967.

Li, Y., Bali, S., Borg, S., Katzmann, E., Ferguson, S.J., Schüler, D., 2013. Cytochrome cd1 nitrite reductase NirS is involved in anaerobic magnetite biomineralization in *Magnetospirillum gryphiswaldense* and requires nirn for proper d1 heme assembly. *J. Bacteriol.* 195: 4297–4309.

Li, Y., Katzmann, E., Borg, S., Schüler, D., 2012. The periplasmic nitrate reductase nap is required for anaerobic growth and involved in redox control of magnetite biomineralization in *Magnetospirillum gryphiswaldense*. *J. Bacteriol.* 194: 4847-4856.

Li, Y., Raschdorf, O., Silva, K.T., Schüler, D., 2014a. The terminal oxidase cbb3 functions in redox control of magnetite biomineralization in *Magnetospirillum gryphiswaldense*. *J. Bacteriol.* 196: 2552–2562.

Li, Y., Sabaty, M., Borg, S., Silva, K.T., Pignol, D., Schüler, D., 2014b. The oxygen sensor MgFnr controls magnetite biomineralization by regulation of denitrification in *Magnetospirillum gryphiswaldense*. *BMC Microbiol*. 14:153.

Ling, D., Lee, N., Hyeon, T., 2015. Chemical synthesis and assembly of uniformly sized iron oxide nanoparticles for medical applications. *Acc. Chem. Res.* 48: 1276–1285.

Lins, U., McCartney, M.R., Farina, M., Frankel, B.B., Buseck, P.R., 2006. Crystal habits and magnetic microstructures of magnetosomes in coccoid magnetotactic bacteria. *An. Acad. Bras. Cienc.* 78: 463-474.

Liu, J., Ding, Y., Jiang, W., Tian, J., Li, Y., Li, J., 2008. A mutation upstream of an ATPase gene significantly increases magnetosome production in *Magnetospirillum gryphiswaldense*. *Appl. Microbiol. Biotechnol.* 81: 551-558.

Liu, X., Guan, Y., Yang, Y., Ma, Z., Wu, X., Liu, H., 2004. Preparation of superparamagnetic immunomicrospheres and application for antibody purification. *J. Appl. Polym. Sci.* 94: 2205-2211.

Lohße, A., Borg, S., Raschdorf, O., Kolinko, I., Tompa, É., Pósfai, M., Faivre, D., Baumgartner, J., Schülera, D., 2014. Genetic dissection of the mamAB and mms6 operons reveals a gene set essential for magnetosome biogenesis in *Magnetospirillum gryphiswaldense*. *J. Bacteriol.* 196: 2658-2669.

Lohße, A., Kolinko, I., Raschdorf, O., Uebe, R., Borg, S., Brachmann, A., Plitzko, J.M., Müller, R., Zhang, Y., Schüler, D., 2016. Overproduction of magnetosomes by genomic amplification of

biosynthesis-related gene clusters in a magnetotactic bacterium. *Appl. Environ. Microbiol.* 82: 3032-3041.

Ma, M., Wu, Y., Zhou, J., Sun, Y., Zhang, Y., Gu, N., 2004. Size dependence of specific power absorption of Fe3O4 particles in AC magnetic field. J. Magn. Magn. Mater. https://doi.org/10.1016/S0304-8853(03)00426-8

Ma, Z.Y., Guan, Y.P., Liu, H.Z., 2005. Synthesis of monodisperse nonporous crosslinked poly(glycidyl methacrylate) particles with metal affinity ligands for protein adsorption. *Polym. Int.* 54: 1502–1507.

Mair, L., Ford, K., Alam, M.R., Kole, R., Fisher, M., Superfine, R., 2009. Size-uniform 200 nm particles: Fabrication and application to magnetofection. *J. Biomed. Nanotechnol.* 5: 182-191.

Maratea, D., Blakemore, R.P., 1981. *Aquaspirillum magnetotacticum* sp. nov., a Magnetic Spirillum. *Int. J. Syst. Bacteriol.* 31: 452-455.

Marghussian 2015. Magnetic properties of nano-glass ceramics, in: Marghussian (Eds.). *Nano-glass ceramics: Processing, properties, and applications*. Oxford: William Andrew, pp. 181-223.

Maruyama, K., Takeyama, H., Nemoto, E., Tanaka, T., Yoda, K., Matsunaga, T., 2004. Single nucleotide polymorphism detection in aldehyde dehydrogenase 2 (ALDH2) gene using bacterial magnetic particles based on dissociation curve analysis. *Biotechnol Bioeng.* 87: 687-694.

Mathuriya, A.S., 2016. Magnetotactic bacteria: nanodrivers of the future. *Crit. Rev. Biotechnol.* 36: 788-802.

Mathuriya, A.S., 2015. Magnetotactic bacteria for cancer therapy. *Biotechnol. Lett.* 37: 491-498.

Matsunaga, T., Kawasaki, M., Yu, X., Tsujimura, N., Nakamura, N., 1996. Chemiluminescence enzyme immunoassay using bacterial magnetic particles. *Anal. Chem.* 68: 3551-3554.

Matsunaga, T., Nakayama, H., Okochi, M., Takeyama, H., 2001. Fluorescent detection of cyanobacterial DNA using bacterial magnetic particles on a MAG-microarray. *Biotechnol. Bioeng.* 73: 400–405.

Matsunaga, T., Sakaguchi, T., Tadakoro, F., 1991. Magnetite formation by a magnetic bacterium capable of growing aerobically. *Appl. Microbiol. Biotechnol.* 35: 651-655.

Matsunaga, T., Suzuki, T., Tanaka, M., Arakaki, A., 2007. Molecular analysis of magnetotactic bacteria and development of functional bacterial magnetic particles for nano-biotechnology. *Trends Biotechnol.* 25: 182-188.

Mériaux, S., Boucher, M., Marty, B., Lalatonne, Y., Prévéral, S., Motte, L., Lefèvre, C.T., Geffroy, F., Lethimonnier, F., Péan, M., Garcia, D., Adryanczyk-Perrier, G., Pignol, D., Ginet, N., 2015. Magnetosomes, biogenic magnetic nanomaterials for nrain molecular imaging with 17.2 T MRI scanner. *Adv. Healthc. Mater.* 4: 1076-1083.

Meyer, A., Berensmeier, S., Franzreb, M., 2007. Direct capture of lactoferrin from whey using magnetic micro-ion exchangers in combination with high-gradient magnetic separation. *React. Funct. Polym.* 67: 1577-1588.

Miltenyi, S., Müller, W., Weichel, W., Radbruch, A., 1990. High gradient magnetic cell separation with MACS. *Cytometry.* 11: 231–8.

Moffat, G., Williams, R.A., Webb, C., Stirling, R., 1994. Selective separations in environmental and industrial processes using magnetic carrier technology. *Miner. Eng.* 7: 1039-1056.

Moisescu, C., Bonneville, S., Tobler, D., Ardelean, I., Benning, L.G., 2008. Controlled biomineralization of magnetite (Fe_3O_4) by *Magnetospirillum gryphiswaldense*. *Mineral. Mag.* 72: 333-336.

Mollenhauer, H.H., 1964. Plastic embedding mixtures for use in electron microscopy. *Stain Technol.* 39: 111–114.

Montague, G.A., Morris, A.J., Ward, A.C., 1989. Fermentation monitoring and control: A perspective. *Biotechnol. Genet. Eng. Rev.* 7: 147-188.

Mosbach, K., Andersson, L., 1977. Magnetic ferrofluids for preparation of magnetic polymers and their application in affinity chromatography. *Nature*. 270: 259–261.

Müller, C., Heidenreich, E., Franzreb, M., Frankenfeld, K., 2015. Purification of equine chorionic gonadotropin (eCG) using magnetic ion exchange adsorbents in combination with high-gradient magnetic separation. *Biotechnol. Prog.* 31: 78–89.

Murat, D., Quinlan, A., Vali, H., Komeili, A., 2010. Comprehensive genetic dissection of the magnetosome gene island reveals the step-wise assembly of a prokaryotic organelle. *Proc. Natl. Acad. Sci.* 107: 5593-5598.

Nakamura, N., Burgess, J.G., Yagiuda, K., Kudo, S., Sakaguchi, T., Matsunaga, T., 1993. Detection and removal of *Escherichia coli* using fluorescein isothiocyanate conjugated monoclonal antibody immobilized on bacterial magnetic particles. *Anal. Chem.* 65: 2036-2039.

Nebe-von-Caron, G., Stephens, P.J., Hewitt, C.J., Powell, J.R., Badley, R.A., 2000. Analysis of bacterial function by multi-colour fluorescence flow cytometry and single cell sorting. *J. Microbiol. Methods* 42: 97–114.

Neu, H.C., Heppel, L.A., 1965. The release of enzymes from *Escherichica coli* by osmotic schock and during the formation of spheroplasts. *J.Biol.Chem.* 240: 3685–3692.

Nguyen, H.V., Suzuki, E., Oestreicher, Z., Minamide, H., Endoh, H., Fukumori, Y., Taoka, A., 2016. A protein-protein interaction in magnetosomes: TPR protein MamA interacts with an Mms6 protein. *Biochem. Biophys. Reports.* 7: 39-44.

Noguchi, Y., Fujiwara, T., Yoshimatsu, K., Fukumori, Y., 1999. Iron reductase for magnetite synthesis in the magnetotactic bacterium *Magnetospirillum magnetotacticum*. *J. Bacteriol.* 181:2142-

2147.

Odabaşi, M., Denizli, A., 2001. Polyhydroxyethylmethacrylate-based magnetic DNA-affinity beads for anti-DNA antibody removal from systemic lupus erythematosus patient plasma. *J. Chromatogr. B Biomed. Sci. Appl.* 760: 137-48.

Ota, H., Takeyama, H., Nakayama, H., Katoh, T., Matsunaga, T., 2003. SNP detection in transforming growth factor-b1 gene using bacterial magnetic particles. *Biosens. Bioelectron.* 18: 683-687.

Overton, T.W., 2014. Recombinant protein production in bacterial hosts. *Drug Discov. Today*. 19: 590-601.

Özkara, S., Akgöl, S., Çanak, Y., Denizli, A., 2004. A novel magnetic adsorbent for immunoglobulin-G purification in a magnetically stabilized fluidized bed. *Biotechnol. Prog.* 20: 1169-75.

Öztürk, N., Günay, M.E., Akgöl, S., Denizli, A., 2007. Silane-modified magnetic beads: Application to immunoglobulin G separation. *Biotechnol. Prog.* 23: 1149-56.

Pankhurst, Q.A., Thanh, N.T.K., Jones, S.K., Dobson, J., 2009. Progress in applications of magnetic nanoparticles in biomedicine. *J. Phys. D. Appl. Phys.* 42:22.

Peng, Z., Ling, M., Ning, Y., Deng, L., 2014. Rapid fluorescent detection of escherichia coli K88 based on DNA aptamer library as direct and specific reporter combined with immuno-magnetic separation. *J. Fluoresc.* 24: 1159-68..

Pierce, J.J., Turner, C., Keshavarz-Moore, E., Dunnill, P., 1997. Factors determining more efficient large-scale release of a periplasmic enzyme from E. coli using lysozyme. *J. Biotechnol.* 58: 1–11.

Plačková, L., Oklestkova, J., Pospíšková, K., Poláková, K., Buček, J., Stýskala, J., Zatloukal, M., Šafařík, I., Zbořil, R., Strnad, M., Doležal, K., Novák, O., 2017. Microscale magnetic microparticle-based immunopurification of cytokinins from Arabidopsis root apex. *Plant J.* 89: 1065-1075.

Plan Sangnier, A., Preveral, S., Curcio, A., K. A. Silva, A., Lefèvre, C.T., Pignol, D., Lalatonne, Y., Wilhelm, C., 2018. Targeted thermal therapy with genetically engineered magnetite magnetosomes@RGD: Photothermia is far more efficient than magnetic hyperthermia. *J. Control. Release*. 279: 271–281.

Pollithy, A., Romer, T., Lang, C., Müller, F.D., Helma, J., Leonhardt, H., Rothbauer, U., Schüler, D., 2011. Magnetosome expression of functional camelid antibody fragments (nanobodies) in Magnetospirillum gryphiswaldense. *Appl. Environ. Microbiol.* 77: 6165-71.

Pósfai, M., Lefèvre, C.T., Trubitsyn, D., Bazylinski, D.A., Frankel, R.B., 2013. Phylogenetic significance of composition and crystal morphology of magnetosome minerals. *Front. Microbiol.* 4:344.

Qian, H., Li, C., Lin, Z., Zhang, Y., 2010. Using thiophilic magnetic beads in purification of antibodies from human serum. *Colloids Surfaces B Biointerfaces*. 75: 342-348.

Qu, Y., Zhang, X., Xu, J., Zhang, W., Guo, Y., 2014. Removal of hexavalent chromium from wastewater using magnetotactic bacteria. *Sep. Purif. Technol.* 136: 10-17.

Raschdorf, O., Müller, F.D., Pósfai, M., Plitzko, J.M., Schüler, D., 2013. The magnetosome proteins MamX, MamZ and MamH are involved in redox control of magnetite biomineralization in *Magnetospirillum gryphiswaldense*. *Mol. Microbiol.* 89: 872–886.

Raschdorf, O., Plitzko, J.M., Schüler, D., Müller, F.D., 2014. A tailored galK counterselection system for efficient markerless gene deletion and chromosomal tagging in *Magnetospirillum gryphiswaldense*. *Appl. Environ. Microbiol.* 80: 4323-4330.

Robinson, P.J., Dunnill, P., Lilly, M.D., 1973. The properties of magnetic supports in relation to immobilized enzyme reactors. *Biotechnol. Bioeng*. 15: 603-606.

Rong, C., Huang, Y., Zhang, W., Jiang, W., Li, Y., Li, J., 2008. Ferrous iron transport protein B gene (feoB1) plays an accessory role in magnetosome formation in *Magnetospirillum*

gryphiswaldense strain MSR-1. *Res. Microbiol.* 159: 530-536.

Rong, C., Zhang, C., Zhang, Y., Qi, L., Yang, J., Guan, G., Li, Y., Li, J., 2012. FeoB2 functions in magnetosome formation and oxidative stress protection in *Magnetospirillum gryphiswaldense* strain MSR-1. *J. Bacteriol.* 194: 3972-3976.

Routledge, S.J., 2012. Beyond de-foaming : The effects of antifoams on bioprocess productivity. *Comput. Struct. Biotechnol. J.* 3: e201210014.

Rui, H., Xing, R., Xu, Z., Hou, Y., Goo, S., Sun, S., 2010. Synthesis, functionalization, and biomedical applications of multifunctional magnetic nanoparticles. *Adv. Mater.* 22: 2729-42.

Ruiz, J.A., López, N.I., Fernández, R.O., Méndez, B.S., 2001. Polyhydroxyalkanoate degradation is associated with nucleotide accumulation and enhances stress resistance and survival of Pseudomonas oleovorans in natural water microcosms. *Appl. Environ. Microbiol.* 67: 225-30.

Schatz, A., Reiser, O., Stark, W.J., 2010. Nanoparticles as semi-heterogeneous catalyst supports. *Chem. A. Eur. J.* 16: 8950-8967.

Scheffel, A., Gärdes, A., Grünberg, K., Wanner, G., Schüler, D., 2008. The major magnetosome proteins MamGFDC are not essential for magnetite biomineralization in *Magnetospirillum gryphiswaldense* but regulate the size of magnetosome crystals. *J. Bacteriol.* 190: 377-86.

Scheffel, A., Gruska, M., Faivre, D., Linaroudis, A., Plitzko, J.M., Schüler, D., 2006. An acidic protein aligns magnetosomes along a filamentous structure in magnetotactic bacteria. *Nature.* 440: 110-114.

Scheffel, A., Schüler, D., 2007. The acidic repetitive domain of the *Magnetospirillum gryphiswaldense* MamJ protein displays hypervariability but is not required for magnetosome chain assembly. *J. Bacteriol.* 189: 6437–6446.

Schübbe, S., Kube, M., Scheffel, A., Wawer, C., Heyen, U., Meyerdierks, A., Madkour, M.H., Mayer, F.,

Reinhardt, R., Schüler, D., 2003. Characterization of a spontaneous nonmagnetic mutant of *Magnetospirillum gryphiswaldense* reveals a large deletion comprising a putative magnetosome island. *J. Bacteriol.* 185: 5779-5790.

Schüler, D., 2008. Genetics and cell biology of magnetosome formation in magnetotactic bacteria. *FEMS Microbiol. Rev.* 32: 654–672.

Schüler, D., 1999. Formation of Magnetosomes in Magnetotactic Bacteria. *J. Molec. Microbiol. Biotechnol*. 1: 79–86.

Schuler, D., Baeuerlein, E., 1998. Dynamics of iron uptake and Fe_3O_4 biomineralization during aerobic and microaerobic growth of *Magnetospirillum gryphiswaldense*. *J. Bacteriol.*180: 159-162.

Schüler, D., Baeuerlein, E., 1997. Iron transport and magnetite crystal formation of the magnetic bacterium *Magnetospirillum gryphiswaldense*. *J. Phys. IV* 7: 647–650.

Schüler, D., Frankel, R.B., 1999. Bacterial magnetosomes: Microbiology, biomineralization and biotechnological applications. *Appl. Microbiol. Biotechnol.* 52: 464-73.

Schüler, D., Spring, S., Bazylinski, D.A., 1999. Improved technique for the isolation of magnetotactic spirilla from a freshwater sediment and their phylogenetic characterization. *Syst. Appl. Microbiol.* 22: 466-71.

Schüler, D., Uhl, R., Baeuerlein, E., 1995. A simple light scattering method to assay magnetism in *Magnetospirillum gryphiswaldense. FEMS Microbiol. Lett.* 132: 139–145.

Schultheiss, D., Handrick, R., Jendrossek, D., Hanzlik, M., Schüler, D., 2005. The presumptive magnetosome protein Mms16 is a poly(3-hydroxybutyrate) granule-bound protein (phasin) in *Magnetospirillum gryphiswaldense*. *J. Bacteriol.* 187: 2416-2425.

Schultheiss, D., Schüler, D., 2003. Development of a genetic system for *Magnetospirillum gryphiswaldense*. *Arch. Microbiol.* 179: 89-94.

Setchell, C.H., 1985. Magnetic separations in biotechnology–a review. *J. Chem. Technol. Biotechnol. Biotechnol.* 35: 175–182.

Sevastsyanovich, Y., Alfasi, S., Overton, T., Hall, R., Jones, J., Hewitt, C., Cole, J., 2009. Exploitation of GFP fusion proteins and stress avoidance as a generic strategy for the production of high-quality recombinant proteins. *FEMS Microbiol. Lett.* 299: 86-94.

Sharma, M., Hasija, V., Naresh, M., Mittal, A., 2008. Functional control by codon bias in magnetic bacteria. *J. Biomed. Nanotechnol.* 4: 44-51.

Silva, K.T., Leão, P.E., Abreu, F., López, J.A., Gutarra, M.L., Farina, M., Bazylinski, D.A., Freire, D.M.G., Lins, U., 2013. Optimization of magnetosome production and growth by the magnetotactic vibrio *Magnetovibrio blakemorei* strain MV-1 through a statistics-based experimental design. *Appl. Environ. Microbiol.* 79: 2823–2827.

Sode, K., Nakasono, S., Tanaka, M., Matsunaga, T., 1993. Construction and characterization of low-temperature-operating biosensors. *Sensors and Actuators B*. 13-14: 663–664.

Song, H.P., Li, X.G., Sun, J.S., Xu, S.M., Han, X., 2008. Application of a magnetotactic bacterium, *Stenotrophomonas sp*. to the removal of Au(III) from contaminated wastewater with a magnetic separator. *Chemosphere.* 72: 616-621.

Song, H.P., Li, X.G., Sun, J.S., Yin, X.H., Wang, Y.H., Wu, Z.H., 2007. Biosorption equilibrium and kinetics of Au(III) and Cu(II) on magnetotactic bacteria. *Chinese J. Chem. Eng.* 15: 847–854.

Spalding, B.J., 1991. Downstream processing: Key to slashing production costs 100 fold. *Bio. Technology.* 9:229-233.

Svoboda, J., 1987. Magnetic methods for the treatment of minerals. Amsterdam: Elsevier Sci. Publ. Co.

Sun, J.B., Zhao, F., Tang, T., Jiang, W., Tian, J., Li, Y., Li, J.L., 2008a. High-yield growth and

magnetosome formation by Magnetospirillum gryphiswaldense MSR-1 in an oxygen-controlled fermentor supplied solely with air. *Appl. Microbiol. Biotechnol.* 79: 389–397.

Sun, J., Li, Y., Liang, X.J., Wang, P.C., 2011. Bacterial magnetosome: A novel biogenetic magnetic targeted drug carrier with potential multifunctions. *J. Nanomater.* 2011: 469031.

Sun, J.B., Duan, J.H., Dai, S.L., Ren, J., Guo, L., Jiang, W., Li, Y., 2008b. Preparation and anti-tumor efficiency evaluation of doxorubicin-loaded bacterial magnetosomes: Magnetic nanoparticles as drug carriers isolated from *Magnetospirillum gryphiswaldense*. *Biotechnol. Bioeng.* 101: 1313-20.

Sun, J.B., Duan, J.H., Dai, S.L., Ren, J., Zhang, Y.D., Tian, J.S., Li, Y., 2007. *In vitro* and *in vivo* antitumor effects of doxorubicin loaded with bacterial magnetosomes (DBMs) on H22 cells: The magnetic bio-nanoparticles as drug carriers. *Cancer Lett.* 258: 109-17.

Taimur Khan, M.M., Pyle, B.H., Camper, A.K., 2010. Specific and rapid enumeration of viable but nonculturable and viable-culturable gram-negative bacteria by using flow cytometry. *Appl. Environ. Microbiol*. 76: 5088-5096.

Tanaka, M., Mazuyama, E., Arakaki, A., Matsunaga, T., 2011. MMS6 protein regulates crystal morphology during nano-sized magnetite biomineralization *in vivo*. *J. Biol. Chem.* 286: 6386-92.

Tanaka, T., Maruyama, K., Yoda, K., Nemoto, E., Udagawa, Y., Nakayama, H., Takeyama, H., Matsunaga, T., 2003. Development and evaluation of an automated workstation for single nucleotide polymorphism discrimination using bacterial magnetic particles. *Biosensors and Bioelectronics.* 19: 325-30.

Tanaka, T., Matsunaga, T., 2000. Fully automated chemiluminescence immunoassay of insulin using antibody - Protein A - Bacterial magnetic particle complexes. *Anal. Chem.* 72: 3518-22.

Tanaka, T., Takeda, H., Kokuryu, Y., Matsunaga, T., 2004a. Spontaneous integration of

transmembrane peptides into a bacterial magnetic particle membrane and its application to display of useful proteins. *Anal. Chem.* 76: 3764–3769.

Tanaka, T., Takeda, H., Ueki, F., Obata, K., Tajima, H., Takeyama, H., Goda, Y., Fujimoto, S., Matsunaga, T., 2004b. Rapid and sensitive detection of 17β-estradiol in environmental water using automated immunoassay system with bacterial magnetic particles. *J. Biotechnol.* 108: 153-159.

Tang, Y.S., Wang, D., Zhou, C., Ma, W., Zhang, Y.Q., Liu, B., Zhang, S., 2012. Bacterial magnetic particles as a novel and efficient gene vaccine delivery system. *Gene Ther.* 19: 1187-95.

Thomas, O.R.T., 1998. Downstream processing of biotechnological products. Volume 30206, Course note. Technical University of Denmark.

Theodossiou, I., Collins, I.J., Ward, J.M., Thomas, O.R.T., Dunnill, P., 1997. The processing of a plasmid-based gene from E. coli. Primary recovery by filtration. *Bioprocess Eng.* 16: 175-183.

Tian, J., Sinskey, A.J., Stubbe, J.A., 2005. Kinetic studies of polyhydroxybutyrate granule formation in *Wautersia eutropha* H16 by transmission electron microscopy. *J. Bacteriol.* 187: 3814-24.

Tsao, C.W., Lee, Y.P., 2016. Magnetic microparticle-polydimethylsiloxane composite for reversible microchannel bonding. *Sci. Technol. Adv. Mater.* 17: 2-11.

Uebe, R., Junge, K., Henn, V., Poxleitner, G., Katzmann, E., Plitzko, J.M., Zarivach, R., Kasama, T., Wanner, G., Pósfai, M., Böttger, L., Matzanke, B., Schüler, D., 2011. The cation diffusion facilitator proteins MamB and MamM of *Magnetospirillum gryphiswaldense* have distinct and complex functions, and are involved in magnetite biomineralization and magnetosome membrane assembly. *Mol. Microbiol.* 82: 818–835.

Uebe, R., Schüler, D., 2016. Magnetosome biogenesis in magnetotactic bacteria. *Nat. Rev. Microbiol.* 14: 621–637.

Uebe, R., Voigt, B., Schweder, T., Albrecht, D., Katzmann, E., Lang, C., Böttger, L., Matzanke, B., Schüler, D., 2010. Deletion of a fur-like gene affects iron homeostasis and magnetosome formation in *Magnetospirillum gryphiswaldense*. *J. Bacteriol.* 192: 4192–4204.

Vali, H., Kirschvink, J.L., 1990. Observations of Magnetosome Organization, Surface Structure, and Iron Biomineralization of Undescribed Magnetic Bacteria: Evolutionary Speculations. In: Frankel, R.B., Blakemore, R.P., (Eds.). *Iron Biominer*. Boston: Springer, pp. 97-115.

Vizcaino-Caston, I., Kelly, C.A., Fitzgerald, A.V.L., Leeke, G.A., Jenkins, M., Overton, T.W., 2016. Development of a rapid method to isolate polyhydroxyalkanoates from bacteria for screening studies, *Journal of Bioscience and Bioengineering*. 121: 101-104.

Wacker, R., Ceyhan, B., Alhorn, P., Schueler, D., Lang, C., Niemeyer, C.M., 2007. Magneto immuno-PCR: a novel immunoassay based on biogenic magnetosome nanoparticles. *Biochem. Biophys. Res. Commun.* 357: 391–6.

Wahl, A., Schuth, N., Pfeiffer, D., Nussberger, S., Jendrossek, D., 2012. PHB granules are attached to the nucleoid via PhaM in Ralstonia eutropha. *BMC Microbiol.* 12: 262.

Wang, F., Chen, C., Chen, Y., Wang, P., Chen, C., Geng, D., Li, L., Song, T., 2018. Magnetically targeted photothermal cancer therapy in vivo with bacterial magnetic nanoparticles. *Colloids Surfaces B Biointerfaces* 172: 308–314.

Wang, Q., Liu, J.X., Zhang, W.J., Zhang, T.W., Yang, J., Li, Y., 2013. Expression patterns of key iron and oxygen metabolism genes during magnetosome formation in *Magnetospirillum gryphiswaldense* MSR-1. *FEMS Microbiol. Lett.* 347: 163-72.

Wang, X., Wang, Q., Zhang, Y., Wang, Y., Zhou, Y., Zhang, W., Wen, T., Li, L., Zuo, M., Zhang, Z., Tian, J., Jiang, W., Li, Y., Wang, L., Li, J., 2016. Transcriptome analysis reveals physiological characteristics required for magnetosome formation in *Magnetospirillum gryphiswaldense*

MSR-1. *Environ. Microbiol. Rep.* 8: 371–381.

Wang, Y., Gao, H., Sun, J., Li, J., Su, Y., Ji, Y., Gong, C., 2011. Selective reinforced competitive biosorption of Ag (I) and Cu (II) on *Magnetospirillum gryphiswaldense*. *Desalination.* 270: 258-263.

Ward, A.C., Rowley, B.I., Dawes, E.A., 1977. Effect of oxygen and nitrogen limitation on poly-beta-hydroxybutyrate biosynthesis in ammonium-grown *Azotobacter beijerinckii*. *J. Gen. Microbiol.* 102: 61-68.

Werckmann, J., Cypriano, J., Lefèvre, C.T., Dembelé, K., Ersen, O., Bazylinski, D.A., Lins, U., Farina, M., 2017. Localized iron accumulation precedes nucleation and growth of magnetite crystals in magnetotactic bacteria. *Sci. Rep.* 7: 1–10.

Widdel, F., Bak, F., 1992. Gram-negative mesophilic sulfate-reducing bacteria, in: Balows, A., Troper, H., Dworkin, M., Harder, W., Schleifer, K. (Eds.), *The Prokaryotes*. New York: Springer, pp. 3352–3378.

Wilhelm, S., Tavares, A.J., Dai, Q., Ohta, S., Audet, J., Dvorak, H.F., Chan, W.C.W., 2016. Analysis of nanoparticle delivery to tumours. *Nat. Rev. Mater.* 1: 16014.

Williams, T.J., Lefèvre, C.T., Zhao, W., Beveridge, T.J., Bazylinski, D.A., 2012. *Magnetospira thiophila* gen. nov., sp. nov., a marine magnetotactic bacterium that represents a novel lineage within the Rhodospirillaceae (*Alphaproteobacteria*). *Int. J. Syst. Evol. Microbiol.* 62: 2443-50.

Wyre, C., 2015. Recombinant protein production in *Escherichia coli*: Optimisation of improved protocols. Thesis (PhD). University of Birmingham.

Xiang, L., Wei, J., Jianbo, S., Guili, W., Feng, G., Ying, L., 2007. Purified and sterilized magnetosomes from *Magnetospirillum gryphiswaldense* MSR-1 were not toxic to mouse fibroblasts *in vitro*. *Lett. Appl. Microbiol.* 45: 75–81.

Xu, G., Ahn, J.H., Chang, S.Y., Eguchi, M., Ogier, A., Han, S.J., Park, Y.S., Shim, C.Y., Jang, Y.S., Yang, B., Xu, A., Wang, Y., Sweeney, G., 2012. Lipocalin-2 induces cardiomyocyte apoptosis by increasing intracellular iron accumulation. *J. Biol. Chem.* 287: 4808-17.

Yan, L., Da, H., Zhang, S., López, V.M., Wang, W., 2017. Bacterial magnetosome and its potential application. *Microbiol. Res.* 203: 19–28.

Yan, L., Zhang, S., Chen, P., Liu, H., Yin, H., Li, H., 2012. Magnetotactic bacteria, magnetosomes and their application. *Microbiol. Res.* 167: 507–519.

Yang, C.D., Takeyama, H., Tanaka, T., Matsunaga, T., 2001. Effects of growth medium composition, iron sources and atmospheric oxygen concentrations on production of luciferase-bacterial magnetic particle complex by a recombinant *Magnetospirillum magneticum* AMB-1. *Enzyme Microb. Technol.* 29: 13–19.

Yang, J., Li, S., Huang, X., Tang, T., Jiang, W., Zhang, T., Li, Y., 2013. A key time point for cell growth and magnetosome synthesis of *Magnetospirillum gryphiswaldense* based on real-time analysis of physiological factors. *Front. Microbiol.* 4: 1–7.

Yang, W., Li, R., Peng, T., Zhang, Y., Jiang, W., Li, Y., Li, J., 2010. MamO and mamE genes are essential for magnetosome crystal biomineralization in *Magnetospirillum gryphiswaldense* MSR-1. *Res. Microbiol.* 161: 701-705.

Yoshino, T., Hirabe, H., Takahashi, M., Kuhara, M., Takeyama, H., Matsunaga, T., 2008. Magnetic cell separation using nano-sized bacterial magnetic particles with reconstructed magnetosome membrane. *Biotechnol. Bioeng.* 101: 470-477.

Yoza, B., Arakaki, A., Matsunaga, T., 2003. DNA extraction using bacterial magnetic particles modified with hyperbranched polyamidoamine dendrimer. *J. Biotechnol.* 101: 219–228.

Zhang, Y., Zhang, X., Jiang, W., Li, Y., Li, J., 2011. Semicontinuous culture of *Magnetospirillum*

gryphiswaldense MSR-1 cells in an autofermentor by nutrient-balanced and isosmotic feeding strategies. *Appl. Environ. Microbiol.* 77: 5851–5856.

Zhao, G.Y., Di, D.H., Wang, B., Zhang, P., Xu, Y.J., 2014. Iron regulates the expression of ferroportin 1 in the cultured hFOB 1.19 osteoblast cell line. *Exp. Ther. Med.* 8: 826-830.

Zhao, L., Wu, D., Wu, L.F., Song, T., 2007. A simple and accurate method for quantification of magnetosomes in magnetotactic bacteria by common spectrophotometer. *J. Biochem. Biophys. Methods.* 70: 377-383.